Annual Report 2016

HI Jena

Helmholtz-Institut Jena

Helmholtz-Institut Jena
Fröbelstieg 3
07743 Jena
www.hi-jena.de

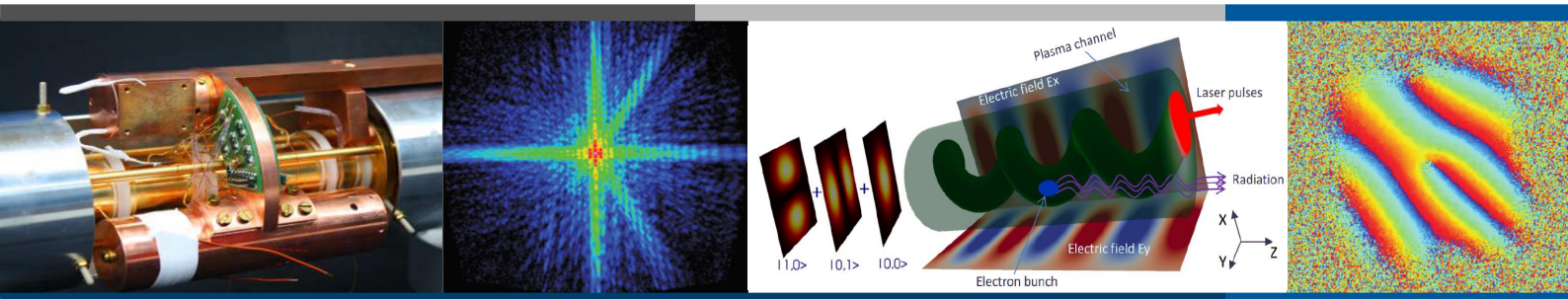

seit 1558

Helmholtz-Institut Jena

Annual Report 2016

Imprint

Publisher:	Helmholtz-Institut Jena, Fröbelstieg 3, 07743 Jena, Germany (http://www.hi-jena.de) @ GSI Helmholtzzentrum für Schwerionenforschung GmbH Darmstadt, Germany (http://www.gsi.de) GSI is member of the Helmholtz association of national research centers (http://www.helmholtz.de).
Editors:	Marc M. Günther and Andrey Volotka
DOI:	10.15120/GSI-2017-00708 (http://dx.doi.org/10.15120/GSI-2017-00708)
Publication date:	May 2017

The annual report 2016 of the Helmholtz-Institut Jena is licensed under the Creative Commons Attribution BY 4.0 (CC BY 4.0):
https://creativecommons.org/licenses/by/4.0/

Contents

Theory 80

Foreword

The central goal of the Helmholtz Institute Jena (HI-Jena), outstation of GSI Darmstadt at the Campus of the Friedrich-Schiller-University Jena, is to maximize synergies between the latest developments in particle accelerators for heavy-ions and electrons and the revolutionary progress in ultra-high intensity laser sources and novel diagnostics in the optical and x-ray regime with particular focus on the interaction of light and matter under extreme conditions. In less than one decade, our institute developed into a well-recognized research institution in the field of photonics with activities covering a broad range of activities such as the design and development of new laser schemes to laser-particle acceleration and to x-ray detection and polarimetry, to name just a few. All these activities are embedded into the research field Matter of the Helmholtz Association where the institute participates in the programs “From Matter to Materials and Life” as well as in “Matter and Technology”. Here the institute closely collaborates with its partner Helmholtz centers GSI at Darmstadt, DESY at Hamburg, and HZDR in Dresden.

With this Annual Report for 2016, we provide an overview of recent research achievements and progress from the last year with 73 contributions. Just to name three remarkable results out of many: attosecond control over relativistic electron bunches (Nature Photonics 239, 1 (2016)), the production of composite states of light and matter (Nature Photonics 10, 445–449, 2016) and a theoretical proposal for studying a new mechanism of nuclear excitation via two-photon electron transitions (editors suggestion Phys. Rev. Lett. 117, 243001 (2016)). Moreover, in the annual report 2016 quite a few important R&D projects currently pursuit at the institute are documented, reflecting also the increasing amount of 3rd party funding. In this context the Research Group “Nano XUV” supported within the framework of ESF should be mentioned as well as various APPA related activities in which the institute is involved in. Moreover, very prominent examples of R&D is related to the commissioning of the JETI200 laser system, a very important, new infrastructure of the institute whose inauguration took place in 2015. In 2016 the commissioning of the JETI 200 laser and the contrast enhancing plasma mirror system was progressing. Results include ASE contrast (ASE: Amplified spontaneous emission) ¿10-12 suppression of prepulses by approximately two orders of magnitude. A first experiment irradiating solid targets have demonstrated sufficient contrast to generate SHHG (SHHG: surface high-harmonic generation) and to optimize this process by introducing a controlled prepulse. This campaign will conclude in May 2017 and will be followed by a LWFA (LWFA: Laser Wakefield Acceleration) commissioning experiment to benchmark performance and stability for LWFA development and high intensity QED (QED: Quantum Electro-Dynamics) experiments.

Furthermore an important part of HI Jena’s activities are related to its Research School for Advanced Photon Science (RS-APS) aiming on the education of the next-generation of scientists in research fields of the institute and for the large scale research infrastructures of the Helmholtz Association such as the international FAIR project in Darmstadt and the European XFEL at Hamburg. Our RS-APS registers continuous interest by doctoral students and in 2016 more than 45 young researchers have participated in the school, with more of the half being 3rd party funded. The annual Lecture Week organized by RS-APS and HGS-HIRe of FAIR has become meanwhile a well-established event. During the fourth lecture week in October 2016 students and lecturers from different research areas at GSI and HI Jena discussed “Innovative detectors for photons and particles”.

Research School of Advanced Photon Science of the Helmholtz Institute Jena

G. Weber[1,2], R. Märtin[1,2], Ch. Spielmann[3], and Th. Stöhlker[1,2,3]
[1]HI Jena, Jena, Germany; [2]GSI, Darmstadt, Germany; [3]IOQ, University Jena, Jena, Germany

Among the most important tasks of the Helmholtz Institute Jena is the education and support of young scientists. The Research School of Advanced Photon Science (RS-APS) provides structured PhD education adapted to the research profile and organizational structure of the HI Jena. Emphasis is given to research being relevant for the international FAIR project in Darmstadt and the European XFEL facility in Hamburg, both being currently in the construction phase.

By the end of 2016 more than 45 PhD students were participating in the program of the research school. About 25 students with third-party funding have decided to join RS-APS to profit from the structured PhD education alongside the 20 stipend holders directly financed by the graduate school. The significant increase in the number of participants just three years after its official inauguration in 2012 is a great success. The doctoral students were supervised by 14 principal investigators belonging directly to the Helmholtz Institute Jena or to institutes of the cooperating University Jena. Besides their doctoral work the students have the possibility to participate in the academic program which is offered directly by the Helmholtz Institute Jena and moreover they have access to the broad spectrum of courses provided by the cooperating graduate programs.

The regular on-site seminars of the Research School provide the students either a platform for presenting their recent results or meeting distinguished researchers in the field. Additionally in 2016 almost half of the students of the HI Jena participated in dedicated soft skill block courses offered by HGS-HIRe focusing on the strengthening the core competencies of young researchers. Furthermore students of the Helmholtz Institute attended so-called Power Weeks by HGS-HIRe. A Power Week is focused on a particular science topic. In contrast to a lecture week it is not interdisciplinary and therefore allows discussions on a much deeper level. In addition transferable skill courses offered on site by the graduate academy Jena have been visited, e.g. qualification in academic teaching.

One major event in 2016 was the third joint HGS-HIRe and RS-APS Lecture Week which took place in Buchenau Manor from October 9th to 14th. The whole week 16 students from RS-APS and HGS-HIRe dealt intensively with “Innovative detectors for photons and particles”. The PhD students have been supervised by the lecturers Michele Caselle (KIT), Andreas Fleischmann (Uni Heidelberg), Volker Tympel (Uni Jena) and Michael Zürch

Figure 1: Participants of the joint lecture week at Haus Ebersberg

(UC Berkely).

The Research School of the HI Jena is not only supporting its students financially through scholarships but also every student has its own annual travel budget which he can spend individually. In 2016 more than two third of the doctoral candidates took use of this money for visiting international workshops and conferences to present their research results.

High Power Laser Development

High Energy Pulse Compression and Focussing of POLARIS Laser Pulses

M. Hornung[1,2,#], H. Liebetrau[2], S. Keppler[2], A. Kessler[1], J. Körner[2], G.A. Becker[2], M. Reuter[2], F. Schorcht[1], M. Hellwing[2], J. Hein[1,2], M.C. Kaluza[1,2]

[1]Helmholtz-Institute Jena, Germany; [2]Institute of Optics and Quantum Electronics, Jena, Germany.

In 2015 and 2016, we have realized an extensive upgrade of the POLARIS laser system in order to reach higher pulse energies and shorter pulse durations.

At the end of this upgrade, we had achieved a record pulse energy of 54.2 J before pulse compression [1]. The spectral bandwidth of these pulses is 18 nm at full width half maximum. Due to the aperture and damage threshold of our tiled-grating compressor, only pulses with a limited energy could be used for compression, focussing and high-intensity experiments. Taking the near-field profile of the fully amplified laser pulses (shown in Fig. 1 a.) and the 200 mJ/cm² damage threshold of the compression gratings into account, we were able to compress 26.6 J pulses, which leads to a pulse energy of 16.7 J on target. The pulses were focused with an f/2-off axis parabola to a minimum focal spot size of A_{FWHM} = 4.1 µm² where the intensity is larger than $I_{max}/2$. The relative energy content in this area is 34 % (q=0.34) and an image of the far-field distribution is shown in Fig. 1 b). Due to an improved utilization of the adaptive optics system, the focal spot size could be more than halved with respect to formerly achieved values (~ 9 µm²).

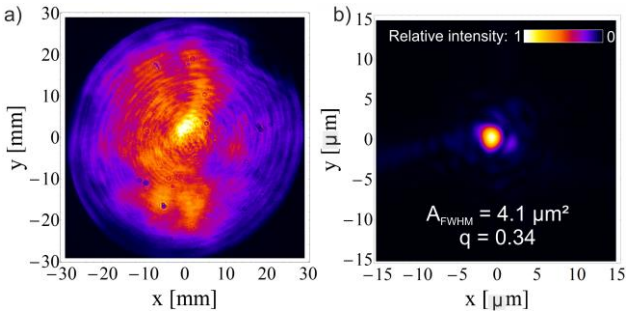

Figure 2: a) Near-field profile of the fully amplified laser pulses (E_{max} = 54.2 J). b) Far-field profile in the target area.

The pulse duration after pulse compression was measured with a home-built 2nd-order autocorrelator. Integrated over the full beam profile we achieved a minimal FWHM pulse duration of t_{FWHM} = 98 fs. The measurement is displayed in Fig. 2 b) and Fig. 2 a) shows the corresponding spectral intensity distribution of the laser pulses. Due to the implementation of tunable spectral filters [2] in the front-end of the laser chain and between A2 and A3 (cf. [1]) we were able to increase the spectral bandwidth to 18 nm FWHM from formerly 11 nm. Furthermore, the stability of the shot-to-shot pulse duration was significantly improved with the installation of an intracavity pulse stretcher in the front-end of Polaris [3].

With a pulse duration of 98 fs and an on-target pulse energy of 16.7 J in a 4.1 µm² focal spot, Polaris is able to generate a peak intensity of 1.3 × 10^{21} W/cm². Since the temporal intensity contrast is of crucial importance for the successful application of the laser pulses in high-intensity experiments, we optimized and measured the temporal contrast for the amplified spontaneous emission to a relative intensity level of I_{ASE}/I_{peak} = 7 × 10^{-13}.

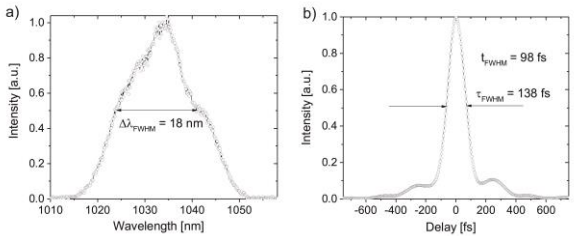

Figure 1 : a) Measurement of the spectral intensity distribution of A5-amplified pulses. b) Pulse duration measurement of the fully amplified pulses.

In conclusion, we have presented results from an extensive upgrade period of the POLARIS laser system which is now able to generate ultra-high intensity laser pulses with ultra-high temporal contrast at a comparatively high repetition rate of f_{rep} = 0.02 Hz. The overall system performance is currently limited by more than a factor of 2 due to the limited compression capabilities and could be increased significantly with state-of the art compression gratings. To the best of our knowledge, we have achieved the highest pulse energy and peak intensity so far with a fully diode-pumped CPA laser system. The optimization of the near field profile of the final amplifier with an additional adaptive optics system is part of ongoing work.

References

[1] M. Hornung, H. Liebetrau, S. Keppler, A. Kessler, M. Hellwing, F. Schorcht, G.A. Becker, M. Reuter, J. Polz, J. Hein, and M. C. Kaluza, "54 J pulses with 18 nm bandwidth from a diode-pumped chirped-pulse amplification laser system", Optics Letters, **41**, Issue 22, pp. 5413-5416 (2016).

[2] S. Keppler, M. Hornung, P. Zimmermann, H. Liebetrau, M. Hellwing, J. Hein, and M. C. Kaluza, "Tunable filters for precise spectral gain control in ultrashort-pulse laser systems", Optics Letters, **41**, Issue 20, pp. 4708-4711 (2016).

[3] H. Liebetrau, M. Hornung, A. Seidel, M. Hellwing, A. Kessler, S. Keppler, F. Schorcht, J. Hein, and M. C. Kaluza, "Intracavity stretcher for chirped-pulse amplification in high-power laser systems ", Optics Letters, **42**, Issue 2, pp. 326-329 (2017).

[#] Marco.Hornung@uni-jena.de

Implementation of the upgraded PHELIX pre-amplifier *

U. Eisenbarth[†1], *S. Götte*[1], *S. Kunzer*[1], *D. Reemts*[1], *B. Zielbauer*[1], *and V. Bagnoud*[1,2]
[1]GSI, Darmstadt, Germany; [2]HIJ, Jena, Germany

In the past year, significant progress has been achieved at the PHELIX laser facility on the way towards higher pulse repetition rates. After detailed studies on the characterization of a flashlamp-based amplifier head and improvements of the optical layout the new pre-amplifier system has been implemented at the PHELIX facility. This step represents an important milestone on the way towards higher performance in terms of output energy and shot repetition rate.

The PHELIX Pre-Amplifier is a flashlamp-based Nd:glass laser amplifier system with a typical pulse output energy of up to 10 J and a repetition rate of one shot every 3 minutes. This limitation mainly arises from thermal wavefront deformations such as defocus, astigmatism, and higher order aberrations as well as birefringence effects. However, some experiments using only the pre-amplifier would greatly benefit from a higher repetition rate. In addition, the design of the 100 J laser to be built for the plasma physics collaboration at FAIR includes a pre-amplifier with the same characteristics as the one of PHELIX but this amplifier should operate at a higher repetition rate. For this reason, it was decided to upgrade the PHELIX pre-amplifier to a repetition rate of 3 shots per minute not only to serve the greater user community but also to gather hands-on experience for the FAIR 100 J laser.

The project follows two lines: at first, a new amplifier layout had to be implemented to overcome the thermal loading limitations of the previous design and second, individual components have been improved. The 45 mm amplifier has been redesigned, which includes a new 45 mm head as well as a new power supply using low voltage (2 kV) and off-the-shelf components. The newly designed optical layout consists of two amplifier heads (19 mm and 45 mm diameter) in double-pass configuration combined with Faraday rotators. The new system needed to be inserted in an existing laser system which led to many layout constraints such as the position of object and image planes, input and exit beam diameters as well as various space limitations.

In a two month shutdown phase in summer 2016, the new system was successfully installed. First measurements demonstrated output energies up to 17 J with considerable margin in terms of flashlamp voltages. Hence the design value of 20 J should be easily reachable. In addition, particular attention was paid to the optimization of the passive transmitted wavefront through the system. Precise alignment in combination with a strongly enhanced Shack-Hartman wavefront sensor (developed at PHELIX) allowed for an overall wavefront error of less than $\lambda/4$. After correction of astigmatic aberrations using controlled deformation of a polarizer plate in the beam path the residual wavefront error corresponds to spherical aberration as the most prominent contribution. During a shot the defocus aberrations is by far the dominating contribution to the wavefront deformation. This effect is compensated using a motorized lens at one of the relay telescopes. Higher order aberrations are compensated by a deformable mirror.

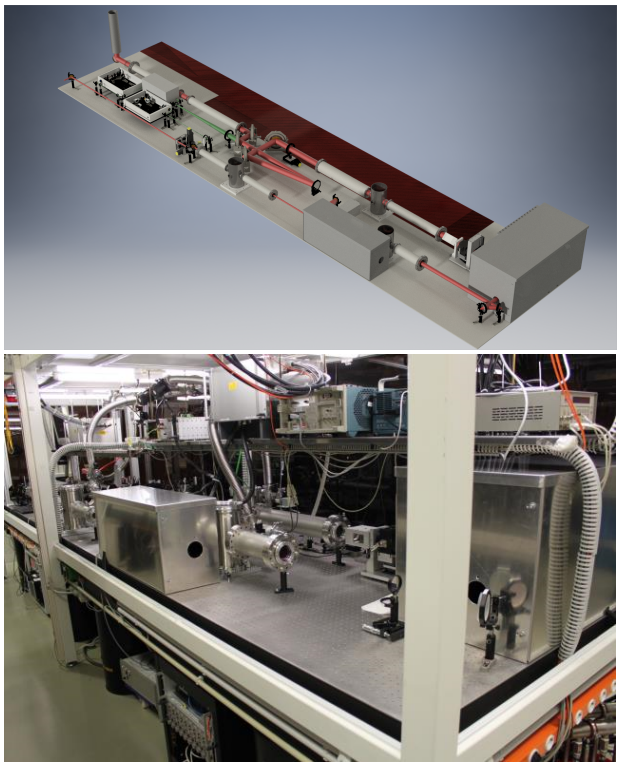

Figure 1: The new PHELIX pre-amplifier as planned (top) and implemented (bottom).

First tests also showed that the magnification of a telescope led to unexpected aperture clipping at the 45 mm head which lead to very little alignment margin and turned out to be critical for daily system usage. Hence, slight modifications of the magnification of telescopes before and after the 45 mm head will easily overcome the limitation. The new lenses will be installed in an upcoming maintenance period. Meanwhile several beamtimes have been performed since the implementation of the new system. The next step will focus on an operation at higher repetition rates on the order of one shot every 20 to 30 s.

* This report is also published in the GSI Scientific Report 2016
† u.eisenbarth@gsi.de

Testing two state-of-the-art laser systems for ELI-ALPS with a Phase meter *

D. Hoff[1,2], *R. Budriunas*[3], *A. Borzsonyi*[4], *S. Hädrich*[5], *T. Eidam*[5], *A. M. Sayler*[1,2], *J. Limpert*[5], *K. Osvay*[4], *and G.G. Paulus*[1,2]

[1]Institute of Optics and Quantum Electronics, Jena, Germany; [2]Helmholtz Institute, Jena, Germany; [3]Light Conversion, Vilnius, Lithuania; [4]ELI-ALPS, Szeged, Hungary; [5]Active Fiber Systems GmbH, Jena, Germany

For the Extreme Light Infrastructure ELI-ALPS in Szeged, Hungary, several laser systems, which push forward the state-of-the-art, have been built [1]. Among others, two of them follow the goal to provide high pulse energy, few-cycle pulse duration and carrier-envelope phase (CEP) stability: The SYLOS laser and, at higher repetition rate, the HR1 laser. Both lasers will reach average output powers in the order of 100 W. The stereo above-threshold ionization (ATI) phase meter has proven to be a versatile tool to test and optimize such cutting edge laser systems in terms of pulse duration and CEP-stability [2]. Here we report on first tests of these two lasers with such a stereo-ATI phase meter and detail their current operating parameters.

Test of the SYLOS laser

This NOPCPA-based laser is built by Light Conversion in Vilnius, Lithuania and provides, in the current stage, 45 mJ of pulse energy at 840 nm central wavelength with a repetition rate of 1 kHz and pulse durations below 9 fs [3]. The passively CEP-stable laser system was found to deliver pulses with a CEP noise of 216 mrad RMS, see figure 2.

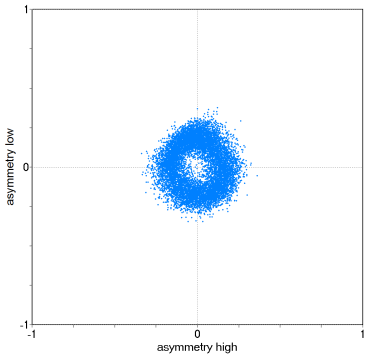

Figure 1: Asymmetry plot of 10 000 CEP-randomized shots from the SYLOS laser. Every blue dot represents a single laser shot with the pulse duration reflected by the radius and the CEP by the azimuthal angle. The average radius of 0.185 corredsponds to 8.5 fs of pulse duration. For details see reference [2].

Test of the HR1 laser

This laser is based on coherent combination of several fibre amplifier channels and is built by Active Fiber Systems in Jena, Germany. It provides 1 mJ pulse energy at 1030 nm central wavelength with a repetition rate of 100 kHz and pulse durations below 7 fs, see figure 3 [4]. Every single shot of the 100 kHz pulse train is evaluated for pulse duration and CEP. The CEP stability is work in progress.

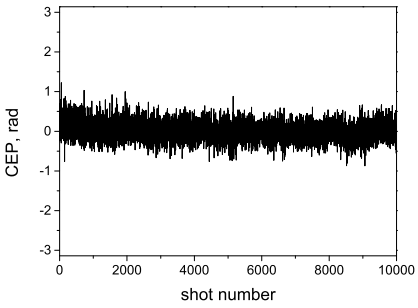

Figure 2: Recorded CEP of 10 000 shots over 10 s of the SYLOS laser with an RMS noise of 216 mrad.

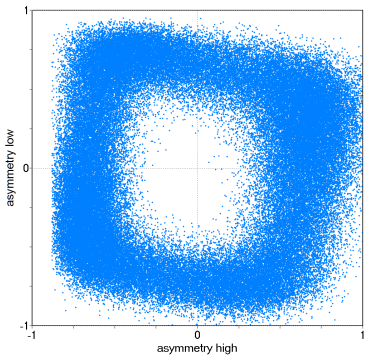

Figure 3: Asymmetry plot of 100 000 shots, i.e. 1 second of operation, from the HR1 laser. The average radius of 0.75 corredsponds to 6.3 fs of pulse duration, i.e. 1.8 cycles at the carrier wavelength of 1030 nm.

References

[1] http://www.eli-alps.hu/

[2] A. M. Sayler et al., "Real-time pulse length measurement of few-cycle laser pulses using above-threshold ionization", Optics express 19, 4464–4471 (2011).

[3] R. Budriunas et al., "53 W average power CEP-stabilized OPCPA system delivering 5.5 TW few cycle pulses at 1 kHz repetition rate", Opt. Express 25, 5797–5806 (2017).

[4] S. Hädrich et al., "Energetic sub-2-cycle laser with 216 W average power," Opt. Lett. 41, 4332–4335 (2016).

* Supported by ELI-ALPS/AFS/HI Jena. dominik.hoff@uni-jena.de

High power nonlinear pulse compression at 2 µm wavelength

M. Gebhardt[1,2], C. Gaida[2], F. Sutzki[2], R. Klas[1,2], S. Demmler[1], J. Rothhardt[1,2], C. Jauregui[2], J. Limpert[#1,2,3], and A. Tünnermann[1,2,3]

[1]Helmholtz-Institute Jena, Fröbelstieg 3, 07743 Jena, Germany; [2]Institute of Applied Physics, Abbe Center of Photonics, Friedrich-Schiller-Universität Jena, Albert-Einstein-Str. 15, 07745 Jena, Germany; [3]Fraunhofer Institute for Applied Optics and Precision Engineering, Albert-Einstein-Str. 7, 07745 Jena, Germany

Powerful, ultrafast laser systems with an emission wavelength around 2 µm are attractive tools for the study of high-field light matter interactions and in particular for efficiently generating high-order harmonics within the water-window [1]. The approach of using a long-wavelength driver to extend the photon energy cut-off towards keV-photon energies is extremely interesting for numerous applications like high-resolution diffractive imaging [2] or spectroscopy [1]. A requirement to expand and enhance the impact of such applications is a significant increase in photon flux/repetition rate. Hence, there is a strong application driven demand for more powerful driving laser sources, which deliver intense pulses around 2 µm wavelength.

Thulium-doped fiber laser systems (TFL) are, in analogy to their well-established ytterbium-based counterparts, an average power scalable solid-state laser concept, which is scalable to hundreds of watts in ultrafast operation [3]. Recently, we have demonstrated 2 GW of peak power with substantial power scaling prospects beyond the current limitations of a single ytterbium-doped fiber amplifiers [4]. These results emphasize the great potential of 2 µm fiber laser systems not only for advancements in pure power scaling but also for addressing demanding future applications like laser particle acceleration [5].

In order to become tomorrow's first choice for addressing scientific applications in high-field physics 2 µm laser systems have to deliver few-cycle pulses. One way of pushing the typically achieved hundreds of fs-pulses towards the few-cycle regime is nonlinear pulse compression. Starting from the above mentioned laser system, which delivered 2 GW, 200 fs-pulses at 61 kHz, we have performed the first nonlinear pulse compression experiment using a TFL and a gas-filled hollow capillary. A schematic of the experimental setup can be seen in Fig. 1. Strong nonlinear spectral broadening was achieved after the propagation through a nitrogen-filled glass capillary with 1 m length and 350 µm inner core diameter. Within this experiment it was found that detrimental propagation effects arising from water-vapor absorption [6] become severe at high gas pressures and have to be circumvented for achieving optimum performance [7]. One of the countermeasures (as discussed in detail in Ref. [7]) is to differentially pump the fiber using a gas with favourable thermo-optical properties. After the nonlinear broadening stage the pulses were compressed to 46 fs (7 optical cycles) using AR-coated fused silica (FS). The compressed pulse energy was 0.25 mJ at an average power of >15 W and a pulse peak power of about 4 GW. The significant pulse shortening becomes apparent when comparing the input and output autocorrelation traces depicted in Fig. 2. It is remarkable that the dispersion properties of FS allow high quality pulse compression towards the few-cycle regime with pulse durations almost identical to the transform limit. This emphasizes that dispersion compensation using FS is a simple, power scalable and effective approach without the need of complex dispersion tailored mirror systems. The laser source presented herein is, to our knowledge, the highest average power 2 µm laser system delivering intense sub-50 fs, GW-class pulses.

Figure 1: Schematic sketch of the experimental setup.

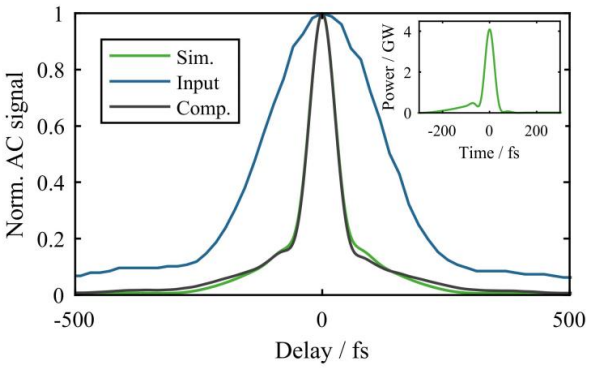

Figure 2: Measured AC traces before (blue) and after the nonlinear compression (black) as well as numerical simulation (green). Inset: Retrieved pulse profile.

Outlook Our future work will concentrate on exploiting the full power scaling potential of ultrafast TDFs and on enhancing the temporal compression in subsequent nonlinear pulse compression. This way, a 100 W-level, GW-class few-cycle source around 2 µm wavelength can be realized in the near future. Such a laser system is ideally suited for addressing the water-window with high photon-flux by generating high-order harmonics in Ne and He.

References

[1] S. L. Cousin et al., Opt. Lett. 39, 5383 (2014)
[2] G. K. Tadesse et al., Opt. Lett. 41, 5170-5173 (2016)
[3] F. Stutzki et al., Opt. Lett. 39, 4671 (2014)
[4] C. Gaida et al., Opt. Lett. 41, 4130 (2016)
[5] J. Breuer et al., Phys. Rev. Lett. 111, 134803 (2013)
[6] M. Gebhardt et al., Opt. Lett. 40, 2770 (2015)
[7] M. Gebhardt et al., Opt. Lett. 42, 747-750 (2017)

[#]jens.limpert@uni-jena.de

Power limits of a CEP stabilized 1.5 μm OPCPA*

K. Mecseki[1], *H. T. Olgun*[2], *M. Windeler*[1], *M. Schulz*[3], *R. Riedel*[3], *F. Tavella*[1], *and M. J. Prandolini*[†2]
[1]SLAC National Accelerator Laboratory, Menlo Park, USA; [2]Helmholtz-Institut Jena, Jena, Germany;
[3]Class 5 Photonics, Hamburg, Germany

High power OPCPAs above 10 W at short-wave IR wavelengths (SWIR: 1.4 – 3 μm) may be limited because of thermal heat dissipation in the nonlinear crystals. In this work, power scaling limits will be discussed.

Scaling to high powers above 10 W requires suitable OPCPA pump lasers at the kilowatt level (P_P), nonlinear crystals that withstand these high pump powers including associated crystal heating through seed and idler beams, and good pump-to-signal conversion efficiency ($P_{\mathrm{SWIR}} = \eta P_P$, where the efficiency $\eta \sim 10\%$). Recently, kilowatt level OPCPA pump lasers with pulse parameters of 16 mJ and 2 ps (FWHM) are currently commercially available (AMPHOS). In addition, compact, CEP stable, 1.5 μm pre-booster OPCPA seed lasers are also commercially available (Class 5 Photonics). The pulse parameters from such a laser are shown in Fig. 1

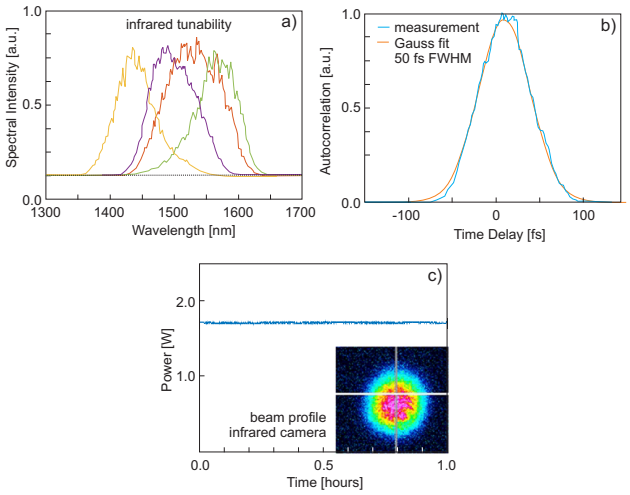

Figure 1: Output parameters for a 1.5 μm pre-booster OPCPA (Class 5 Photonics: White Dwarf): a) tunable spectrum, b) Fourier limited autocorrelation, c) power stability and beam profile.

Numerical simulations were carried out on the first booster stage of a non-collinear OPCPA, pumped by a kilowatt AMPHOS laser and seeded by a pre-booster laser from Class 5 Photonics. The aim was to produce CEP 1.5 μm output pulse energies near 2 mJ for the first stage, with a bandwidth supporting $\sim$50 fs. In order to match the pulse width of the pump pulse with the seed signal pulse, the signal was stretched to match the pump pulse.

* Work supported by HI Jena
† mark.prandolini@desy.de

Table 1: OPCPA simulation output parameters for the first stage using both KTP and KTA. In signal output columns, values are calculated without/with crystal heating effects. The final conversion efficiency is calculated as a pump-to-signal efficiency.

Pulse Parameter	KTP Output	KTA Output
E [mJ]	2.3/1.5	2.1/2.0
τ [ps] (FWHM)	1.2/0.9	1.2/1.2
B-Integral	0.4/0.4	0.7/0.7
M^2	1.1/1.7	1.1/1.1
η(Conv. Eff. [%])	14/9	13/13
Fourier Limit [fs]	51/61	55/55

Two nonlinear OPCPA crystal were examined – KTP and KTA. In addition, to estimate the change in temperature across the crystal, a simple model of a crystal holder was used, which has a heat sink around the edge of the crystal and considers only a radial heat flow. At a repetition rate of 100 kHz, the heat load for KTP/KTA integrated over the whole crystal was calculated to be 1.4/6.6, 933/70, and 85/328 [mW] for the signal, idler, and pump pulses, respectively. For KTP, the idler beam dominates the heat load. For KTA, the pump beam dominates the heat load, because the idler pulse at 3 μm has significantly less absorption at these wavelength compared to KTP (see [1]).

Additionally, the single-pulse simulated parameters for the first stage for both KTP and KTA, including third order effects, were calculated for two separate cases: without and with thermal effects (Table 1). In the case of KTA, all laser parameters were affected by less than 1%. In the case of KTP, significant changes to the laser parameters were calculated. For example, the energy and bandwidth dropped by 30% and 24%, respectively, and M^2 increase by from 1.1 to 1.7.

In summary, we reviewed the critical thermal parameters for KTP and KTA for producing high power laser pulses at 1.5 μm pumped at 1030 nm. At pump power of 1.6 kW, up to 200 W of output energy (2 mJ pulse energy (Table 1) at 100 kHz) could be expected for KTA nonlinear crystals with little pulse parameter distortion.

References

[1] K. Mecseki, H. T. Olgun, M. Windeler, M. Schulz, R. Riedel, F. Tavella and M. J. Prandolini, Proceedings of SPIE Vol. 10082, 100821C (2017).

Spatio-temporal combination for kw-class, 12 mJ femtosecond fiber laser system

M. Kienel[1,2], M. Müller[2], A. Klenke[1,2], J. Limpert[1,2,3], and A. Tünnermann[1,2,3]

[1]Helmholtz-Institute Jena, Fröbelstieg 3, 07743 Jena, Germany;

[2]Institute of Applied Physics, Abbe Center of Photonics, Friedrich-Schiller-Universität Jena, Albert-Einstein-Str. 15, 07745 Jena, Germany;

[3]Fraunhofer Institute for Applied Optics and Precision Engineering, Albert-Einstein-Str. 7, 07745 Jena, Germany

Fiber lasers are ideal candidates for achieving high average powers in combination with a high beam quality and efficient amplification due to their intrinsically good thermal management given by the advantageous aspect ratio. However, in terms of pulse peak-power, nonlinear pulse distortions induced by self-phase modulation and self-focusing limit the usefulness due to the beam confinement in small cores. Additionally, mode instabilities set an upper limit for the specific average power. Straightforward mitigation strategies such as increasing the guided beam diameter by advanced fiber designs and applying chirped-pulse amplification (CPA) helped to push the performance further over the past decade. But further increasing the mode-field diameter and the stretched pulse duration becomes challenging.

One scaling approach that we have pursued over the last years has been to employ parallel amplification channels with subsequent coherent recombination of the resulting output beams and output pulses [1]. This technique can provide an improvement of the average power and peak power by up to a factor of N (N: number of parallel channels). An additional approach is to amplify more than a single pulse at the fundamental repetition rate of such a system, followed by temporal recombination. This is especially useful for fiber amplifiers as the extractable energy from the active material is typically larger than the amount of energy being extractable with a single pulse.

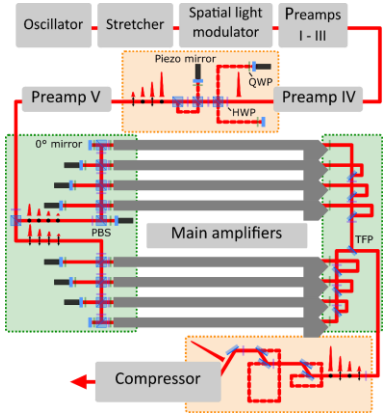

Fig. 1: Scheme of the fiber-CPA system with 8 parallel channels and 4 temporal pulse replicas.

We have integrated the latter approach into a fiber-CPA system with 8 combined large-mode area fiber amplifiers. The corresponding experimental setup is schematically depicted in Fig. 1. A splitting stage containing two delay lines (with adjustable lengths realized with piezo actuators) has been added between preamplifier IV and V to split a single incoming pulse into 4 pulse replicas separated by about 4 ns each. After amplification in the parallel amplifiers and after the spatial recombination of the beams, these pulse replicas are recombined into a single pulse by delay lines of the same lengths as in the splitting stage. An active stabilization system optimizes the output for the maximum power and compensates for environmental fluctuations.

With this setup a pulse energy of 12 mJ could be achieved at an average power of 700 W [2]. Additionally, a high spatial and temporal combination efficiency of around 80% could be achieved. The excellent beam quality of a single amplifier could also be retained.

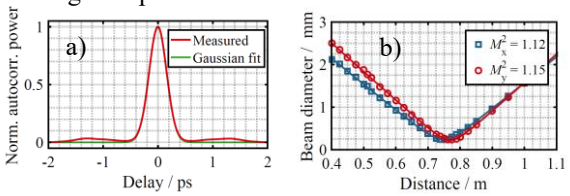

Fig. 2: a) Autocorrelation trace of the output pulse and b) M^2 beam measurement at 12 mJ pulse energy

The achieved performance values of this system are unprecedented for fiber-laser systems so far.

Currently, work is being done to advance both the parallel amplifier configuration and the temporal pulse combination. This includes realizing the temporal recombination from the fundamental oscillator repetition rate of the laser system without prior temporal pulse splitting as well as the integration of the parallel amplification channels into multicore fibers. This will open up the possibility to build systems with even more temporal and spatial pulse replicas, therefore making it possible to move to even higher performance values without sacrificing the inherent advantages of fiber lasers.

References

[1] J. Limpert, A. Klenke, M. Kienel, S. Breitkopf, T. Eidam, S. Hädrich, C. Jauregui, and A. Tünnermann, IEEE JSTQE **20**, 268 (2014).

[2] M. Kienel, M. Müller, A. Klenke, J. Limpert, and A. Tünnermann, Opt. Lett. **41**, 3343-3346 (2016)

* This work has been partly supported by the German Federal Ministry of Education and Research (BMBF) under contract 13N13167 “MEDUSA” and by the European Research Council under the ERC grant agreement no. [617173]. M. K. and A.K. acknowledge financial support by the Helmholtz- Institute Jena. M. M. acknowledges financial support by the Carl-Zeiss Stiftung.

† jens.limpert@uni-jena.de

Intracavity stretcher for high-energy chirped pulse amplification

H. Liebetrau[*1], *M. Hornung*[1,2], *S. Keppler*[1], *A. Kessler*[2], *I. Tamer*[2], *M. Hellwing*[1], *F. Schorcht*[2], *J. Hein*[1,2], *and M. C. Kaluza*[1,2]

[1]Institut für Optik und Quantenelektronik, FSU Jena, Germany; [2]Helmholtz-Institut Jena, Germany

Within the past years the frontend of POLARIS has been optimized to deliver pulses with high intensity contrast and durations as short as 86 fs [1, 2]. The new 8-pass setup for the ns-stretcher established within 2015 [2], however, has disadvantages in certain aspects. First the design requires a focal length of 2 m of the imaging telescope and thus, leads to a large setup and optics with apertures of up to 10". As the stretcher is known to be a source of phase noise, deteriorating the intensity contrast in the ps-range [3], investigating this effect would cause high costs when an optic has to be replaced. Second, the long propagation distance where the pulse is spectrally dispersed (∼60 m) results in distortions of the spectral phase caused by refractive index modulations of the air inside the stretcher, leading to pulse duration variations of more than a factor of 3.

To overcome these limitations we extended the principle of intracavity stretching [4] to ns-pulse duration by inserting an Offner-type stretcher into a regenerative amplifier [5]. The setup of this stretching amplifier (StAmp) is shown in Fig. 1. As the pulses travel 40 roundtrips within the StAmp, the stretcher setup itself and its optics are much smaller compared to the old ns-stretcher. With the angle of incidence set to $\alpha_{in} = 60.7°$ and the virtual grating distance to G_{sl}=144 mm, the StAmp generates the same spectral phase as the old ns-stretcher and simultaneously amplifies the pulses to 100 μJ with a bandwidth of 27 nm. When seeded into the POLARIS main amplifiers, these pulses can be compressed to 88 fs (amplifier A2) and 102 fs (amplifier A5).

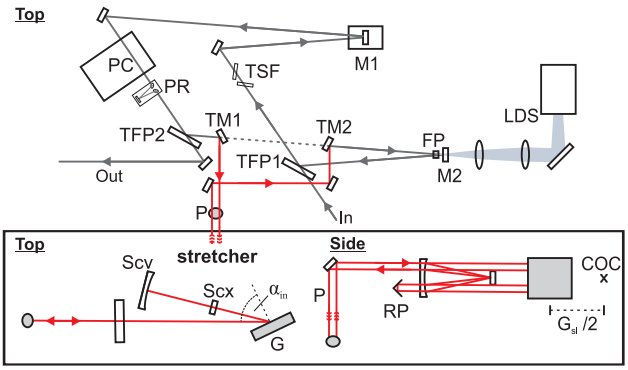

Figure 1: Setup of the amplifier with intracavity stretching: M1 - spherical end-mirror (R_1=5m), PC - Pockels cell, PR - polarization rotator, TFP1/2 - thin film polarizer, TM1/2 - turning mirror, P - periscope, G - diffraction grating (1480 lines/mm), Scv/Scx - concav and convex spherical mirror (f_{cv}=0.2 m, f_{cx}=-0.1 m), RP - roof prism, FP - fluoride phosphate glass, M2 - planar pump-mirror, TSF - transmissive spectral filters, LDS - laser diode stack and pump optics, COC - center of curvature for telescope mirrors, α_{in} - angle of incidence, G_{sl} - 2 times the distance between grating G and COC. Gray dashed line: cavity path without stretcher

The ps-contrast of the StAmp is increased in intensity most likely due to a low quality of a stretcher optic. However, the small setup allows us to investigate this influence in the future without causing high costs. Due to the small stretching factor per round trip, the spatial dispersion inside the Offner-stretcher is small compared to the 8-pass stretcher and the spectral phase is not distorted by refractive index modulations of air. This leads to an improved pulse duration stability shown in Fig. 2, which has proved to significantly enhance the stability of TNSA experiments performed with POLARIS in 2016.

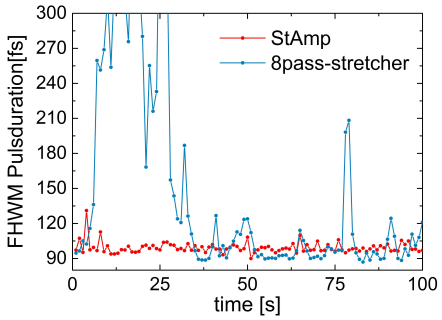

Figure 2: Pulse duration (amplifier A2, 1 Hz) over time with the old stretcher and the StAmp-technique

References

[1] H. Liebetrau, M. Hornung, A. Seidel, M. Hellwing, A. Kessler, S. Keppler, F. Schorcht, J. Hein, and M. C. Kaluza, Opt. Exp. **22**, 24776 (2014).

[2] H. Liebetrau, M. Hornung, S. Keppler, M. Hellwing, A. Kessler, F. Schorcht, J. Hein, and M. C. Kaluza, *Opt. Lett.*, Vol. 41, Nr. 13, S. 3006–3009, 2016.

[3] J. Bromage, C. Dorrer, and R. K. Jungquist, *J.Opt.Soc.Am.B*, Vol. 29, Nr. 5, p. 1125–1135, 2012.

[4] E. Caracciolo, M. Kemnitzer, M. Rumpel, A. Guandalini, F. Pirzio, F. Kienle, T. Graf, M. A. Ahmed, J. A. der Au, and A. Agnesi, *Opt. Lett.*, Vol. 40, Nr. 7, p. 1532–1535, 2015.

[5] H. Liebetrau, M. Hornung, S. Keppler, M. Hellwing, A. Kessler, F. Schorcht, J. Hein, and M. C. Kaluza,' *Opt. Lett.*, Vol. 42, Nr. 2, p. 326–329, 2017.

* Hartmut.Liebetrau@uni-jena.de

Tunable filters for precise spectral gain control in short-pulse laser systems*

S. Keppler† [1], *M. Hornung*[1,2], *H. Liebetrau*[1], *M. Hellwing*[1], *A. Kessler*[2], *F. Schorcht*[2], *J. Hein*[1,2], *and M. C. Kaluza*[1,2]

[1]Institute of Optics and Quantum Electronics, FSU Jena, Germany; [2]Helmholtz-Institute Jena, Germany

The continuous research progress in relativistic laser plasma physics is driven by the ongoing development of high-power short-pulse laser systems. Higher pulse energies as well as shorter pulse durations have led to an increased on-target intensity. To generate ultra-short pulses, the amplification of a broad spectral bandwidth with a flat spectral phase is necessary. However, owing to the non-homogeneous spectral gain characteristic of the different broadband laser materials, a narrowing of the spectral bandwidth during amplification occurs. Various methods have been proposed so far to compensate for spectral gain narrowing including thin angle-tuned étalons, birefringent plates and acousto-optic programmable gain control filters (AOPGCF). These methods, however, disturb either the temporal intensity contrast or the spectral phase of the laser pulse. Both must be avoided for the application of the pulses in high-intensity experiments.

We have developed a new method based on tunable spectral filters (TSFs) which allows for an adjustable and precise control of the spectral gain in ultra-short pulse laser systems [1]. The TSFs are partially reflective dielectric filters, which were used in transmission. The laser pulses propagate through the TSF and experience losses due to the partial reflections. To realize a spectrally shaped reflectivity of the TSF, Gaussian-shaped side-band oscillations of a dielectric mirror have been used. Fig. 1a) shows the reflectivity curve of a TSF that has been designed for compensating the spectral gain of Yb:CaF_2. Here, three different side-band oscillations, enlarged in Fig. 1b), can be used for the compensation. By tuning the angle of incidence of the TSF, the side-bands can be shifted to the desired wavelength. If several TSFs of the same design are used successively, the spectral shape and depth of the losses can be modified. Hence, with a single or a combination of TSFs, the spectral losses experienced by the laser pulse can be precisely tailored. Furthermore, the TSFs provide small spectral aberrations, a high damage threshold and generate no pre- or postpulses.

Fig. 2 shows the gain narrowing compensation of a regenerative amplifier generating an output energy up to 50 mJ with Yb:FP15 as the active material. The uncompensated output spectrum (red line in Fig. 2a) of the amplifier has a bandwidth of 11.5 nm which would support a minimum pulse duration of 135 fs. The implementation of two TSFs, which were designed for Yb:FP15, could broaden

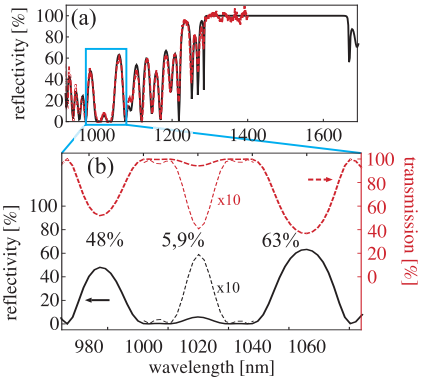

Figure 1: Spectral reflectivity and transmission of a TSF designed for Yb:CaF_2.

the output spectrum to 30 nm which is 2.5 times wider than without compensation. The compensated spectrum could be recompressed to a pulse duration of 86 fs, which corresponds to a pulse shortening and thus, an increase of the on-target intensity of this amplifier of 34 % [2].

Furthermore, compensating gain narrowing with TSFs was successfully applied to the 50-Joule amplifier A5 of the high-power laser system POLARIS [3]. Here, the output spectrum was broadened by 70% from 14 nm to 23.9 nm, which is, to the best of our knowledge, the broadest spectrum reported for a 50-Joule Yb:CaF_2 amplifier and theoretically supports a pulse duration as short as 79 fs.

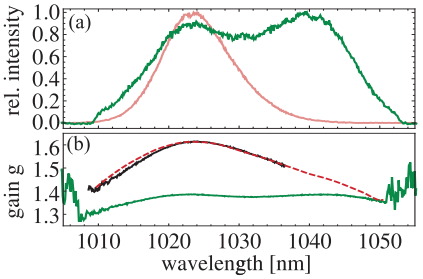

Figure 2: Uncompensated gain (b, red) and output spectrum (a, red); compensated gain (b, green) and output spectrum (a, green) of a 50 mJ regenerative amplifier.

References

[1] S. Keppler et al., Opt. Lett. **41** 4708 (2016).

[2] H. Liebetrau et al., Opt. Lett. **41** 3006 (2016).

[3] M. Hornung et al., Opt. Lett. **41** 5413 (2016).

* Work supported by European Commission (EC) 7th Framework Programme (LASERLAB-EUROPE, 284464); Bundesministerium für Bildung und Forschung (BMBF) (03Z1H531, 05P15SJFA1).

† Sebastian.Keppler@uni-jena.de

Pulse-contrast considerations on divided-pulse amplification setups

M. Kienel[1,2], M. Müller[2], A. Klenke[1,2], J. Limpert[1,2,3], and A. Tünnermann[1,2,3]

[1]Helmholtz-Institute Jena, Fröbelstieg 3, 07743 Jena, Germany;

[2]Institute of Applied Physics, Abbe Center of Photonics, Friedrich-Schiller-Universität Jena, Albert-Einstein-Str. 15, 07745 Jena, Germany;

[3]Fraunhofer Institute for Applied Optics and Precision Engineering, Albert-Einstein-Str. 7, 07745 Jena, Germany

The amplification of a burst of laser pulses followed by a temporal combination into a single pulse is called divided-pulse amplification (DPA). This technique is very suitable for fiber laser based sources because in this amplifier architecture the stored energy generally is higher than the energy extractable by a single pulse, even in chirped-pulse amplifiers (CPA) [1]. Thus, DPA constitutes a further energy and peak-power scaling concept that demonstrated >35 GW peak power [2]. For > 100 GW peak power targeted in our laser systems, pulse contrast considerations become an important subject of investigation. In DPA for CPA femtosecond lasers, free space delay lines are employed for the temporal recombination, often together with polarizing beam splitters (PBS) or thin-film polarizers (TFP). In order to recombine an input pulse train in such a setup, it needs to have a special polarization pattern (see Fig. 1. for the example of four pulse replica). While, in an ideal, case all power can be combined into a single output pulse with a perfect pulse contrast, in reality, the PBSs do not have a perfect polarization contrast leading to pulse contrast degradation.

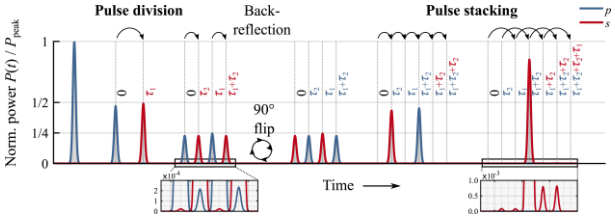

Fig. 1: Scheme of pulse burst generation and combination.

As an example for non-idealized PBSs, the pulse stacking is illustrated step-wise in Fig. 1. The transmission $T_p = 0.97$ and reflectivity $R_s = 0.99$ of the PBS have been assumed, which are typical specifications for commercially available high-contrast PBS. The polarization components being reflected or transmitted into unintended ports of the PBSs during the pulse division lead to slight deviations from the ideal s- and p-polarizations. Thus, field components of different pulse replicas leak into the wrong optical paths, i.e. residual parts that need to be delayed are non-delayed and vice-versa. This results in parasitic pulses during pulse stacking, as shown in the inset below the stacked pulse. Furthermore, peak-power differences among the individual pulses of the burst result in phase imbalances between p- and s-polarization components upon superposition. These translate into deviations from the expected linear-polarization after each combination, again leading to a pulse contrast degradation.

The impact of the parameters T_p, R_s and angle uncertainties of the waveplates on the pulse stacking is quantified simultaneously. For this, the intrinsic temporal stacking efficiency and the pulse contrast are calculated in a Monte Carlo simulation. The stacking efficiency is the ration between the energy extracted from the amplifiers and the energy of the combined pulse. Considering a combination with up to 6 delay lines (64 pulses), 10^5 iterations are carried out for random adjustments of each HWP assuming an uncertainty of ±1° and ideal polarization combiners with $T_p = R_s = 1$, TPFs with $T_p = 0.99$ and $R_s = 0.999$, and PBSs with $T_p = 0.97$ and $R_s = 0.99$.

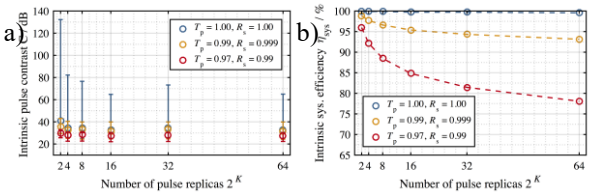

Fig. 2: a) Monte Carlo simulation of the intrinsic pulse contrast and b) corresponding system efficiency

The corresponding intrinsic pulse contrast is shown in Fig. 2(a) with the circles showing the mean values and the error bars the minimum and maximum deviations. In the case of $T_p = R_s = 1$ (blue) the theoretically infinite pulse contrast is reduced on average to ~ 35 dB. For TFP and PBS it gets more likely reduced to ~ 30 dB. The corresponding intrinsic system efficiency is shown in Fig. 2(b). As can be seen, the system efficiency is drastically decreased for degrading PBS or TFP specifications and for an increasing number of pulses. Thus, high-quality TPFs are preferred over PBSs in order to improve both the intrinsic pulse contrast and the intrinsic system efficiency. For further pulse contrast improvements, which will be necessary in the future, additional polarizers can be added into the delay lines to improve on the polarization contrast as well as other well-known contrast improving elements like pockels cells.

References

[1] J. Limpert, A. Klenke, M. Kienel, S. Breitkopf, T. Eidam, S. Hädrich, C. Jauregui, and A. Tünnermann, IEEE JSTQE **20**, 268 (2014).

[2] M. Kienel, M. Müller, A. Klenke, J. Limpert, and A. Tünnermann, Opt. Lett. **41**, 3343-3346 (2016)

* This work has been partly supported by the German Federal Ministry of Education and Research (BMBF) under contract 13N13167 “MEDUSA” and by the European Research Council under the ERC grant agreement no. [617173]. M. K. and A.K. acknowledge financial support by the Helmholtz- Institute Jena. M. M. acknowledges financial support by the Carl-Zeiss Stiftung.

† jens.limpert@uni-jena.de

Multi-pass relay imaging layouts for high energy laser amplifiers

J. Körner[1], *J. Hein*[1,2], *and M.C. Kaluza*[1,2]

[1]Institute of Optics and Quantum Electronics, Jena, Germany; [2]Helmholtz-Institute Jena, Germany

High energy laser amplifiers are typically designed as multi-pass amplifiers, because the desired beam sizes and profiles can hardly be realized in regenerative cavities. In low gain laser media, where fluences are typically below the saturation fluence, a high number of passes is needed to achieve an acceptable energy extraction efficiency. Hence, to maintain commonly used flat top shaped beam profiles and to counteract diffraction effects throughout the amplification process relay imaging in between every material pass is required. Imaging systems for many amplification passes, where each pass contains its own optical elements, will lead to a vastly increased system complexity with many degrees of freedom for adjustment. This will limit the maximum suitable number of passes. Therefore, especially for amplifiers with a large number of round-trips, reusing the imaging setup for every pass is desirable.

In a detailed theoretical work [1] we investigated such so called "relay imaging systems". Starting with only a minimum of assumptions it could be shown that there are only two different types of such systems that can be constructed with up to three imaging elements, namely Type I systems, resembling a telescope, and Type II systems, corresponding to an angle compensated double imaging of a single lens or mirror. Both types are exemplified for lenses in figure 1.

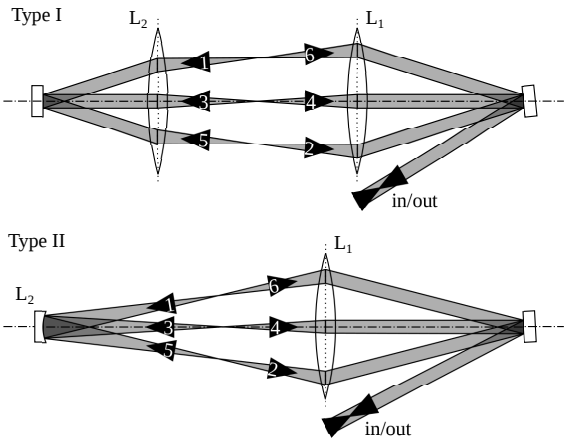

Figure 1: Schematic layouts for Type I and II systems with lenses and only three double passes for clarity.

We used an ABCD matrix calculation formalism to describe the most prominent aberrations that can occur in such systems, which allowed to derive universal quantitative statements in dependence of the system's geometry and to describe compensation methods. It could be demonstrated that the influence of a thermal lens as well as the astigmatism in mirror based layouts could be compensated by the system's optics itself simply trough an adaption of distances and incidence angles.

As cross checks for the ABCD calculations coherent ray-tracings with wavefront analysis on test systems were carried out as depicted in figure 2. The results from the different methods were in very good agreement, showing that the aberration compensation algorithm is working as expected.

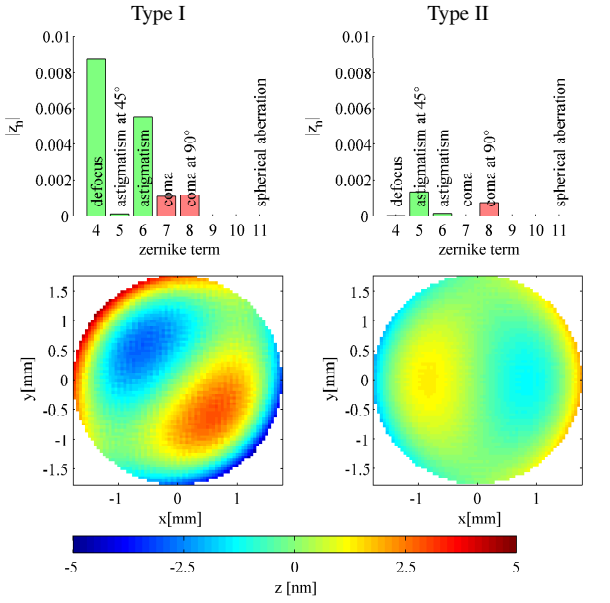

Figure 2: Wave front aberrations of an optimized Type I system (5 round-trips) and a Type II system (10 round-trips) from coherent ray-tracing. Upper row: Zernike coefficients (numbering according to Noll [2], wavelength was 1 μm). Lower row: residual wave front deformation after subtracting terms lower than 7 as false color map.

This work allows to design relay imaging multi-pass systems for compact high energy amplifiers comprising a high number of round-trips, a low number of optical elements, a small footprint, and an excellent wavefront transmission.

References

[1] J. Körner, J. Hein, and M. C. Kaluza, "Compact Aberration-Free Relay-Imaging Multi-Pass Layouts for High-Energy Laser Amplifiers", Appl. Sci. 6[11], 2016, pp. 353–370, doi: 10.3390/app6110353

[2] R. J. Noll, "Zernike polynomials and atmospheric turbulence", J. Opt. Soc. Am. 66[3], 1976, pp. 207-211, doi: 10.1364/JOSA.66.000207

Laser Particle Acceleration

Ring-like Spatial Distribution of Laser Accelerated Proton Beams *

G. A. Becker[1], S. Tietze[2], J. Reislöhner[1], S. Keppler[1], M. Hornung[2], A. Seidel[2], J. Bin[3,4], L. Bock[1], F. Brack[5], M. Hellwing[1], P. Hilz[3,4], A. Kessler[2], S. Kraft[5], S. Kuschel[2], H. Liebetrau[1], J. Polz[1], H-P. Schlenvoigt[5], F. Schorcht[2], K. Zeil[5], J. Hein[1,2], U. Schramm[1], M. Zepf[1,2,6], J. Schreiber[3,4], S. Rykovanov[2], and M. C. Kaluza [1,2]

[1]Institut für Optik und Quantenelektronik, Friedrich-Schiller-Universität Jena, Germany; [2]Helmholtz-Institut Jena, Germany; [3]Fakultät für Physik, Ludwig-Maximilians-Universität, Germany; [4]Max-Planck-Institut für Quantenoptik, Germany; [5]Institut für Strahlenphysik, Helmholtz-Zentrum Dresden-Rossendorf, Germany; [6]School of Mathematics and Physics, Queens University Belfast, UK

Laser-driven proton acceleration has seen a considerable amount of experimental and theoretical research since the first experiments at the turn of the millennium [1]. This research covers inter alia the spectral and spatial characteristics of the accelerated proton beams under different experimental conditions, since an excellent understanding and control over these is necessary for applications.

Utilizing the POLARIS laser system at the Helmholtz-Institute Jena, an experiment has been performed to investigate the proton beam profiles with submicron-thick plastic foils as targets. In order to use foils with thicknesses from 100 nm up to 800 nm without being destroyed by a prepulse, POLARIS' laser pulses were frequency doubled to $\lambda = 515$ nm to achieve the necessary Temporal Intensity Contrast (TIC) [2]. A fast responding plastic scintillator, with two gateable CCD cameras (supported by CR-39 nuclear track detectors for a few shots), was employed as an online-diagnostic for the proton beams' angular distribution. The dominant feature of the proton-beam profile is a ring-like structure (Fig. 1a). 2D-Particle-In-Cell simulations were performed with the EPOCH-code to investigate the origin of this ring. The simulated Gaussian laser pulse had a normalized amplitude of the vector potential $a_0 = 4.5$ and a full-width-at-half-maximum pulse duration of $\tau = 140$ fs, matching experimental conditions. The peak of the laser pulse entered the simulation box ($x = -5$ µm) at $T_{peak} = 322$ fs. A two peak structure in the proton beam's angular distribution – corresponding to a ring in 3D – was produced (Fig. 1b).

This structure can be explained within the Target Normal Sheath Acceleration (TNSA) [3] regime. The laser pulse is focused onto the plastic foil, generating hot electrons and accelerating them through the foil. These electrons form a sheath at the foil's rear side, producing a longitudinal charge separation field with MV/µm amplitudes between the sheath and the foil. This field is strongest opposite the focus' position and decreases transversally. Therefore protons in the center are accelerated the most and travel larger longitudinal distances than protons further outside. This leads to a Gaussian-like proton distribution expanding into vacuum, generating a transverse charge separation field (Fig. 1c) which accelerates protons outwards. This results in a gain in the protons' transverse momentum p_y, as shown in Fig. 1d where p_y is plotted over the protons' spatial coordinates. From the rear side of the foil ($x = 0.2$ µm) p_y increases in the longitudinal direction with maxima at the indicated positions. The longitudinal momentum p_x increases from the foil's rear side in the longitudinal direction as well, whereas the largest p_x is located at the front and the lateral center of the proton distribution. Looking at $|\theta| = |\tan^{-1}(p_y/p_x)|$ plotted over the spatial distribution (Fig. 1e) large areas exist from which protons are emitted under roughly the same angle. When weighted with the particle density distribution, this results in the maxima of the protons' angular distribution shown in Fig. 1f.

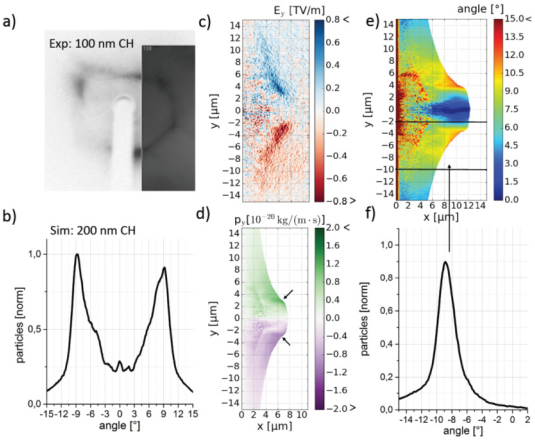

Figure 1: a) Measured and b) simulated angular distribution of accelerated protons. The transverse components of c) the quasi-static electric field and d) the proton momentum for $T_{peak} + 118$ fs. e) The absolute value of the average proton emission angle for $T_{peak} + 198$ fs while f) shows the angular distribution of protons within the designated area normalized to b).

References

[1] Macchi et al., Rev. Mod. Phys. 85, 751 (2013).
[2] Hornung et al., Appl. Sciences 5, 1970 (2015).
[3] Wilks et al., Phys. Plasmas 8, 542 (2001).

*Work is part of the SFB TR18 and onCOOPtics

Improvement of the homogeneity of the laser-driven proton beam within the LIGHT project

D. Jahn[1], *D. Schumacher*[2], *C. Brabetz*[2], *S. Weih*[1], *J. Ding*[1], *F. Kroll*[3,4], *F.E. Brack*[3,4], *U. Schramm*[3,4], *T. E. Cowan*[3,4], *V. Bagnoud*[2,5], *A. Blazevic*[2,5], *and M. Roth*[1]

[1]Technische Universität Darmstadt, Darmstadt, Germany; [2]GSI Helmholtzzentrum für Schwerionenforschung, Darmstadt, Germany; [3]Technische Universität Dresden, Dresden, Germany; [4]Helmholtzzentrum Dresden-Rossendorf, Dresden, Germany; [5]Helmholtz-Institut Jena, Jena, Germany

Laser-driven ion acceleration is an emerging and promising field in which the Laser Ion Generation Handling and Transport (LIGHT) project makes a significant contribution. LIGHT combines the laser-driven ion acceleration with conventional accelerator technology realized in a worldwide unique test beamline [1] and leads to developments of experimental and applied science capability for e.g. FAIR and radiography. The project is based on a Target Normal Sheath Acceleration (TNSA) source driven by the Petawatt High-Energy Laser for Heavy Ion EXperiments (PHELIX) 100 TW beam resulting in a exponential proton energy spectrum. The generated ions are captured by a high-field solenoid for energy selection of protons of 9±1 MeV via chromatic focusing and transported into a radiofrequency double spiral resonator operating at -90 degrees synchronous phase which is used for phase rotation of the single ion bunch. Behind the resonator, the beam is transported into a second target chamber. This transport can optionally be supported with two permanent quadrupole doublets. In the second target chamber a second high-field solenoid system was installed for steep focusing to access highest proton peak intensities. The beamtime in April 2016 aimed to improve the proton beam homogeneity. This goal is essential to enable the time-resolved imaging capability of the laser-driven proton beam and for the determination of a density distribution of a sample. In this beamtime, the so called Radiochromic Imaging Spectroscopy (RIS) was chosen as the detection method in which several radiochromic films (RCF) enable a spectral and spatial analysis of the beam profile. Due to the Bragg behaviour of the protons connected to a corresponding position in the film, an energy resolution is possible. Based on the transverse spectrum, the so called normalized beam uniformity factor (isonorm 13694:2015) can be calculated, which describes whether the beam has an uniform distribution ($U_\eta = 0$ completely uniform).
We have shown already the successful generation of sub-nanosecond focused proton bunches [2], this time compression enables the resolution of fast dynamic processes. Now we will improve the beam homogeneity. Figure 1 a) shows the beam profile recorded on a RCF film (Bragg peak at 7.4 MeV) at 6 m distance from target and shows low particle numbers but it has a good homogeneity ($U_\eta = 0.27$). Based on TraceWin simulations, we removed the quadrupole doublets from the beamline and improved the transport efficiency.

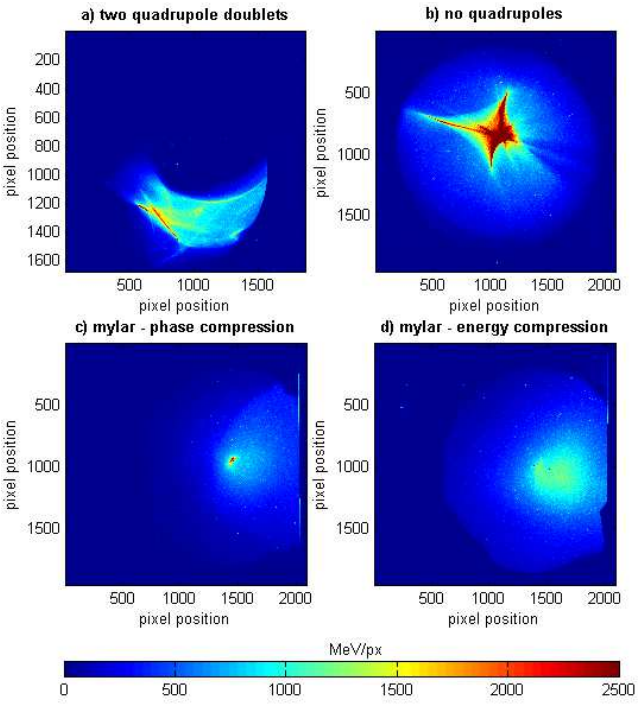

Figure 1: Beam profiles at 6 m distance from the target: a) beam with the installed quadrupole doublets, b) beam without the quadrupole doublets, c) time compressed beam with a mylar foil, d) energy compressed beam with a mylar foil.

Figure 1 b) demonstrates a higher energy deposition at 6 m distance from target and a star shaped inhomogeneity leading to $U_\eta = 0.50$. In the next step, a 1.25 μm thin mylar foil for transverse scattering (negligible energy loss of 10%) was placed between the first solenoid and the rf cavity leading to significant improvements. Figure 1 c) shows the beam profile of a beam which is compressed in time with a beam uniformity $U_\eta = 0.38$. Figure 1 d) shows the profile of a beam which is compressed in energy with a beam uniformity $U_\eta = 0.25$. This beam uniformity value in combination with the increased particle number describes an essential improvement in our beam transport quality.

References

[1] S. Busold *et al.*, NIMA **740**, 94-98 (2014)

[2] S. Busold *et al.*, Scientific Reports **5**, 12459 (2015)

This report is also published in *News and Reports from High Energy Density generated by Heavy iOn and Laser Beams 2016*.

Temporal pulse profile studies of seeded free-electron lasers*

H. Höppner[1], *S. Toleikis*[1], *F. Tavella*[2], *the FERMI collaboration*[3], *and M. J. Prandolini*†[4]
[1]DESY, Hamburg, Germany; [2]SLAC, Menlo Park, USA; [3]Elettra-Sincrotrone Trieste, Trieste, Italy;
[4]Helmholtz-Institut Jena, Jena, Germany

The temporal intensity profile of a free-electron laser (FEL) is of utmost importance for FEL users exploring the new scientific perspectives offered by FELs and is a difficult experimental parameter to determine. Our method is based on the cross-correlation of the FEL with an external optical laser, providing online and single-shot performance [1]. Extensive measurements were carried out at FERMI, where the special FEL pulse properties arising from a combination of FEL machine and external seeding-laser parameters were investigated [2]. Here we present an example measurement, where electron dispersion R_{56} scans were carried out, demonstrating two main pulses with a separation in agreement with theory. These results provide essential FEL intensity information to users that in the past was often lacking.

To measure the temporal intensity profile of an FEL, we used the single-shot EUV/optical cross-correlation with a solid-state target [1]. With this method, the wavefront of the FEL is tilted with respect to the target, thereby spatially encoding the FEL intensity onto the surface target sample. The FEL pulse excites transient electrons into the conduction band of the target, modifying its optical transmission properties. This evolution is monitored by a probing optical laser with a wavefront parallel to the target. Online analysis of the cross-correlation data uniquely determines the intensity profile of EUV FEL pulses.

For this series of measurements, the seeding FEL laser had a pulse duration of 112 ± 2.5 fs, resulting in an FEL pulse duration of 53 ± 3 fs. Subsequently, the dispersion parameter R_{56} was increased from an optimized value of 26.2 μm up to 75 μm. This increase drives a previously optimized seeding condition into a deeply saturated condition. This setting is expected to induce the formation of multiple structures in the FEL pulse. Fig. 1(a) shows measurements of the cross-correlation data. Starting at $R_{56} = 46.5\,\mu$m, the pulse profile has a well separated secondary peak. At larger values of R_{56}, the pulse clearly splits into two substructures whose separation grows with the dispersion R_{56}. In Fig. 1(b) the pulse separation resulting from the profiles is compared to calculation. We observe two main pulses with a separation in reasonable agreement with the theory.

In addition, the pulse spectra, measured simultaneously and independently via the spectrometer (data not shown), show the presence of intensity modulations suggesting a structure in the temporal distribution. A rough assumption that the splitting leads to the formation of two identical Gaussian pulses separated in time by an interval with a common frequency chirp. The chirp was derived from the previous analysis of the experimental data (see [2]). With this analysis, we were therefore able to reproduce the FEL pulse separation compared to experiment (see Fig. 1).

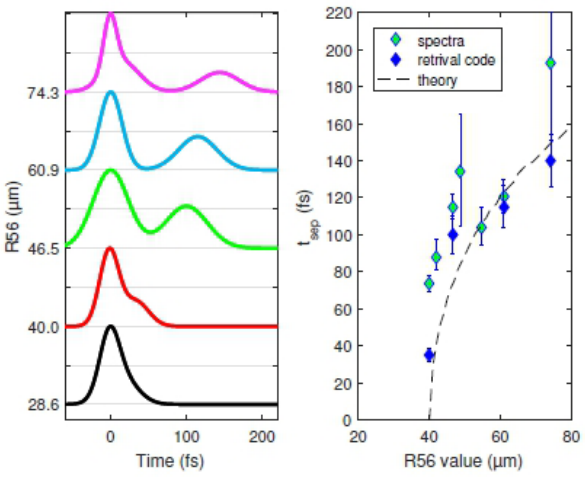

Figure 1: Pulse temporal profile as a function of the R_{56} parameter. Left: single-shot cross-correlation retrieved FEL temporal pulse profile. Right: measured temporal separation of the split pulses at $R_{56} > 40\,\mu$m (blue diamonds); separation calculated (black dashed line); pulses separation estimated from the spectral traces (green diamonds).

The above experimental technique has therefore shown the capability to provide temporal measurements, even in the presence of complex pulse structures (with multiple peaks both in the temporal and spectral domain), whenever these were induced by specific tuning of the machine parameters. Thus transient transmission cross-correlation may provide a tool to link the spectral shape to the pulse temporal structure on a single-shot basis.

References

[1] R. Riedel, A. Al-Shemmary, M. Gensch, T. Golz, M. Harmand, N. Medvedev, M. J. Prandolini, K. Sokolowski-Tinten, S. Toleikis, U. Wegner, B. Ziaja, N. Stojanovic, and F. Tavella, Nat. Commun. **4**, 1731 (2013).

[2] P. Finetti, et al., "Pulse duration of seeded free-electron lasers", in preparation for Physical Review X.

* Work supported by HI Jena
† mark.prandolini@desy.de

Platform development for laser accelerated particle induced nuclear reaction studies utilizing RC methods*

P.Neumayer[1,2], A.Yakushev[1,3], J. Khuyagbaatar[1,3], V. Bagnoud[1,4], Ch.Brabetz[1], B. Borm[1,5], J. Hornung[1,4], F.Wagner[1], T. Kuehl[14,6], T.Stoehlker[1,4,7], J.Despotopulos[8], D.Sayre[8], D.Schneider[8]

[1]GSI Helmholtzzentrum, Darmstadt, Germany, [2]J.W.-Goethe University, Frankfurt, Germany, [3]JHelmholz Institute Mainz, Mainz, Germany, [4]Helmholtz Institute Jena, Jena, Germany, [5]TU Darmstadt, Darmstadt, Germany, [6]J.-Gutenberg University, Mainz, Germany, [7]F.-Schiller University, Jena, Germany, [8]Lawrence Livermore National Laboratory, Livermore, USA

A team of GSI and LLNL researchers successfully completed a platform development experiment to enable future nuclear science experiments at short-pulsed laser facilities. The experiment was led from the GSI side as a joint effort between the plasma physics and super heavy element research departments. This first experiment demonstrated an efficient collection of isotopes produced in nuclear reactions with laser-driven MeV proton beams. The proposed experiment was awarded the requested runtime of 20 shifts and 40 shots have been used to demonstrate the isotope collection efficiency and reproducibility.

The experiment utilizes laser-accelerated (MeV) proton beams (5 – 20 MeV) in combination with a gas-jet technique to study nuclear reactions. In particular (p,n), (p,2n), (p,pn)-reactions in thin ^{nat}Cu-foils were used to measure the rates of the short lived ^{62}Cu and ^{63}Zn.

The proton beams where produced through the TNSA (Target Normal Sheath Acceleration) mechanism utilizing the GSI PHELIX Laser beam pulses at 90 J and 500 fs impinging on a thin gold target (the observation of Laser accelerated protons has first been reported from experiments at LLNL laser facilities [1,2]). After various tests to identify the spatial, time and energy distribution of the accelerated protons, the protons were used to activate thin Cu-foils and to measure the level of activation. This was found to be consistent with known milli-barn cross sections for 5 – 20 MeV protons.

After passing through a thin capton foil as debris shield and a thin Ti-foil as window in the gas filled (in flow mode) target cell inside the main target chamber, the protons interacted with a stack of 1µm-thick Cu target foils (5-10 foils) inside the target cell. The spot size of the accelerated protons at the exit of the conversion foil is less than 1 mm due to the small source emittance. But due to the divergence of the accelerated protons the spot size at the target foils is increased to around 10 mm. The parameters of the accelerated protons were measured at the exit of the target chamber.

The reaction residues recoiling from the targets were stopped in a He + KCl aerosol carrier-gas at about 1 bar pressure, and transported to a filter through a thin PTFE tube. Transported residues were identified by measuring the γ-rays associated with their radioactive decays. In Fig. 1 the comparison of γ-spectra before and after activation of the Cu are shown. Taken into account the measured half-lives, the 511 and 669 keV mainly originate from ^{62}Cu and/or ^{63}Zn

The length of the transport line was varied from a 1m to 20 m distance resulting in a transport efficiency loss of around 80%.

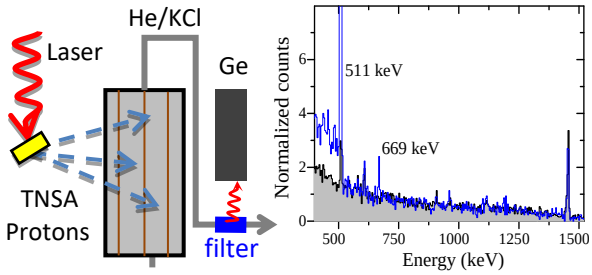

Figure 1: (left) Schematic drawing of the experimental setup. (right) Gamma-spectra of the filter before (shaded-area) and after the laser shots.

The presented experiment at PHELIX with laser accelerated MeV protons and a pulse duration of around 1 ps opens up new domains of studies through the detection of short lived isomers. The experiments provide critical experimental input for future experiments at FAIR (Facility for antiproton and heavy ion research) facility [3], but also at laser facilities as ELI (Extreme Light Infrastructure)[4]. The collaborative experimental research is part of an agreement between LLNL (DOE) and the GSI (BMBF).

References

[1] R. A. Snavely et al., PRL **85**, 2954 (2000)

[2] D. A. Shaughnessy, et al., Rev. Sci. Instr. 85, 063508(2014).

[3] FAIR Green Paper - The Modularized Start Version, 2009

[4] ELI-NP White Book, eds. D. Habs et al. (2010), http://www.eli-np.ro/documents/ELI-NP-WhiteBook.pdf

* This report is also published in the annual report of the Helmholtz Institute Jena

Background free ionization injection in a laser wake field accelerator

S. Kuschel[1,2], *M. B. Schwab*[1,2], *W. Ziegler*[1,2], *M. Yeung*[1], *D. Hollatz*[2], *A. Seidel*[2], *A. Sävert*[1,2], *M. C. Kaluza*[1,2], *and M. Zepf*[1,2,3]

[1]Helmholtz Institute Jena, Fröbelstieg 3, 07743 Jena, Germany; [2]Institute for Optics and Quantumelectronics, Friedrich-Schiller-Universität of Jena, Max-Wien-Platz 1, 07743 Jena, Germany; [3]School of Mathematica & Physics, Queens University Belfast, BT7 1NN, UK

Laser wake field accelerators (LWFA) have shown the potential to accelerate electrons over cm-scales distances to GeVs of energy[1]. It holds the promise to provide accelerated electrons for different kinds of secondary experiments while still being an affordable tool for university sized labs. While the maximum energy of laser accelerated electrons has been continuously increased, accurate control over the spectral shape and particularly the spectral bandwidth of the electrons still need to improve to match the requirements for many secondary experiments.

The key for gaining control over the spectral shape and the beam emittance is the injection process. Different schemes have been proposed and demonstrated, but uncontrolled self-injection is still a problem to fight against in most setups.

We have identified a regime in which we can drive a plasma wake self-injection free and inject electrons into the wake by adding a dopant gas (N_2). This allows the study of different injection mechanisms without background.

The slow down of the phase velocity of the plasma wake (β_p) is a neccessary requirement for wave breaking to occur. This slow down is given by

$$\beta_p = 1 - \underbrace{\frac{1}{2}\frac{\omega_p^2}{\omega^2}}_{\text{dispersion}} - \underbrace{\frac{\omega_p^2}{\omega^2}}_{\text{etching}} - \underbrace{\frac{\zeta}{2n_e}\frac{\partial n_e}{\partial \zeta}}_{\text{density downramp}} \qquad (1)$$

with the laser frequency ω, the plasma frequency ω_p, the co-moving coordinate ζ and the plasma density n_e. The transverse probing pictures (Shadowgrams), which resolve the plasma wave with an unprecended precision ([2]) also allow to infer the plasma density variations on a micron scale. The data show, that density downramps due to an inhomogeneous plamsa density profile are the leading contribution the slow down of the phase velocity of the plasma wake rather than dispersion and etching alone. Consequently these variations also act as the main trigger for wave breaking and therefore the self-injection process.

A comparison between gas jet and gas cell shows that the gas cell's homogeneous plasma density is likely to be the reason for it's suppression of self-injection.

The the transition from uncontrolled self-injection (gas jet) to ionization injection (gas cell) leads to an increase of the pointing stability of the e^--beam by an order of magnitude. Also the divergence of the final electron beam has been impoved by a similar factor, depending on the electron density used (Fig. 2).

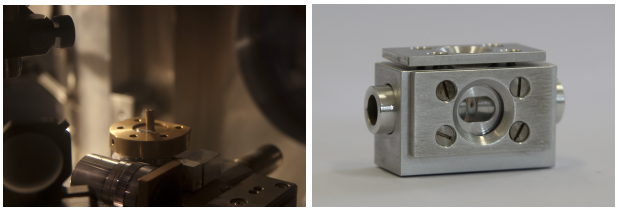

Figure 1: Images of the gas jet (left) and the newly developed gas cell (right). The acceleration length is set to 2 mm in both cases.

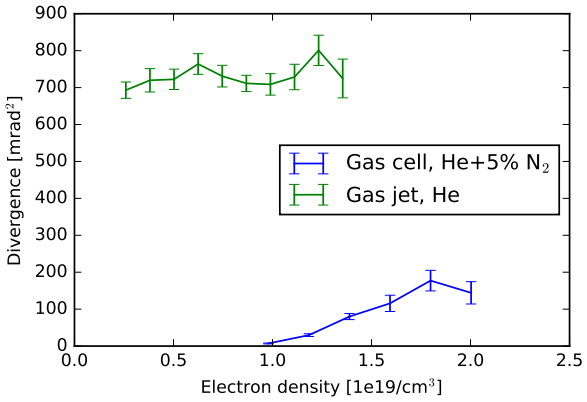

Figure 2: The gas jet (self-injection) and the gas cell (ionization-injection) show different scalings of the accelerated electron beam divergence depending on the plasma density.

With the increased peak power of the new JETI 100 laser system of the Helmholtzinstitute Jena, it will be possible to trigger wave breaking in the gas cell while maintaining the spot size and plasma density, which will allow us to gain further insight into the wave breaking process. These future experiments will assess if the electron beam quality of the gas jet is due to the density variation or if they are linked to the wave breaking process itself.

References

[1] W.P. Leemans et al., PRL 113, 24 (2014)

[2] M.B. Schwab et al., APL 19, 103 (2013)

Polarisation rotation through azimuthal magnetic fields in a laser wakefield accelerator

M. Reuter[1,2], *M. Leier*[1], *E. Siminos*[3], *A. Sävert*[1,2], *and M.C. Kaluza*[1,2]
[1]IOQ , Jena, Germany; [2]HI Jena, Germany; [3]Chalmers, Gothenburg, Sweden

Polarisation rotation of a linearly polarised, ultrashort probe beam inside a laser wakefield accelerator is investigated. Due to the high temporal and spatial resolution of the polarograms, new insight into the accelerating structure is gained. Simulations support the experimental findings.

Future applicability of laser accelerated electron pulses and the corresponding secondary radiation requires a stable and controllable acceleration process. Therefore, it is essential to investigate and understand the dynamics during the acceleration process.

In a laser-wakefield accelerator (LWFA), an intense laser pulse excites a plasma wave – an electron oscillation propagating with the laser's group velocity. In the first half cycle of the plasma wave, large electric fields ($\approx 100\,$GV/m) can accelerate trapped electrons close to the speed of light c. The electron current – generated both by the accelerated and the plasma wave electrons – as well as the displacement current generated by the temporally varying electric field of the plasma wave, induce azimuthal magnetic fields [1]. A manifestation of these magnetic fields is Faraday rotation – the rotation of the polarisation of an electromagnetic wave. Highly resolved optical probing of the laser plasma interaction at different time steps reveals new insights into the accelerating structure.

The experiment was performed with the JeTi-laser at the IOQ Jena, delivering $\approx$750 mJ in $\approx$30 fs. Focused with an $f/20$ off-axis parabolic mirror, a vacuum intensity of $\approx 2\times10^{18}$ W/cm^2 was achieved. The energy of the accelerated electrons, generated in a pulsed helium gas jet with a diameter of 2.1 mm, was measured in a magnetic spectrometer. A fraction of the laser pulse was spectrally broadened in a hollow core fibre. After temporal compression, probe pulses with a duration of $\approx$6 fs [2] were available. In combination with the imaging system, highly resolved snapshots of the interaction were generated. Two CCD cameras equipped with a polariser with polarisation angles $\phi_1 \approx -\phi_2$ were employed to measure the polarisation state of the probe beam after traversing the interaction region. Dividing the pixel values of the two images through each other reduces the initial brightness modulations of the probe beam whereas the bright and dark regions due to polarisation rotation remain.

At different time steps during the interaction represented by the position of the laser pulse inside the gas jet x, the maximum of the angle of rotation ϕ_{rot} was determined. The measured curve (red circles in Figure 1) peaks at $x \approx 650\,\mu$m. In close vicinity, wavebreaking radiation (brown triangle) was detected indicating the presence of strong magnetic fields during wavebreaking which could be traced back to the plasma wave by means of simulations. Moreover, the concurrence of wavebreaking and maximal signal (turquoise squares) could be confirmed by simulations .

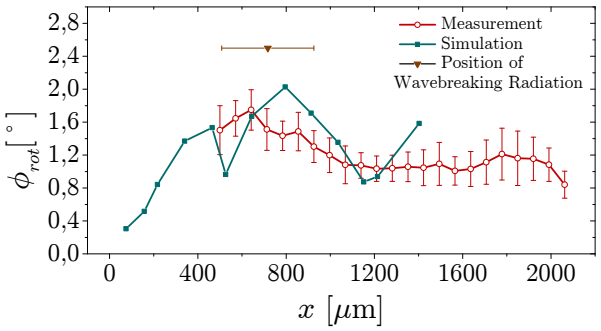

Figure 1: Measured (red) and simulated (turquoise) angle of rotation ϕ_{rot} as well as the average position of wavebreaking (brown).

During the interaction, the shape of the signal changes. At first, two spots are observed in the experiment (Figure 2(a)) as well as the simulation (b). At later positions, the signal has developed a more complex structure ((c) experiment, (d) simulation) representing the ongoing evolution of laser pulse and plasma wave.

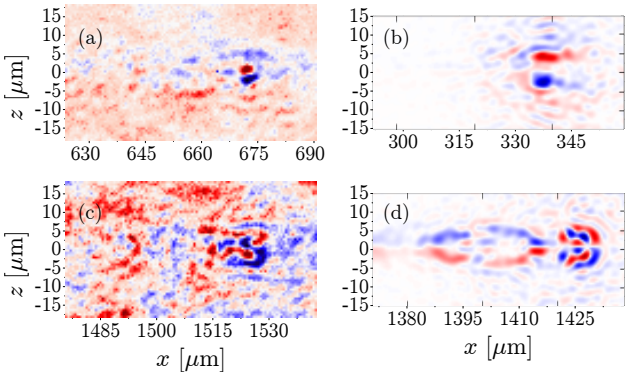

Figure 2: The appearance of the rotation signal changes due to the evolution of laser pulse and plasma wave. Left-hand side: measurement, right-hand side: simulations.

References

[1] M. C. Kaluza et al.: PRL **105** (11), 2010
[2] M. B. Schwab et al.: APL **103** (19), 2013

Laser-assisted discharge ignition for plasma waveguides

C. Wirth[1], *A. Sävert*[1,2], *W. Ziegler*[1], *and M. C. Kaluza*[1,2]

[1]Institute of Optics and Quantum Electronics, Jena, Germany; [2]Helmholtz-Institute Jena, Germany

We present the results of a stabilization analysis of a high voltage discharge in a hydrogen filled capillary. In the experiment the influence of the preionization of the gas with an intensive femtosecond laser pulse on the discharge as well as the guiding properties of the plasma waveguide have been investigated.

In the process of laser wakefield acceleration (LWFA) electrons can be accelerated by the huge longitudinal electric fields ($> 100\,$GV/m) of a plasma wave structure, reaching GeV-energies on a centimeter-scale [1]. To efficiently use these longitudinal fields of the plasma wave, the wave has to sustain over the whole acceleration length meaning the laser intensity has to remain sufficiently high throughout the whole length. This can be achieved by guiding the laser pulse in a preformed plasma channel generated by a high-voltage (HV) discharge in a hydrogen filled capillary [2].

The experiment was carried out at the JeTi-40 laser system in Jena [3]. For the stabilization analysis the start of the capillary discharge relative to an artificial signal (relative ignition time) has been observed on an oscilloscope both with and without preionizing the hydrogen in the capillary with a fraction of the JeTi-40 laser pulses (3 mJ, 30 fs). Additionally the guiding of a HeNe-laser (cw, 35 mW) in the generated plasma channel has been studied by analyzing the quality of the HeNe-focal spot at the capillary exit with a gateable CCD allowing a time scan with 20 ns step size. The quality q of the focal spot at the exit is defined as:

$$q = \frac{\text{power in } 1/e^2\text{-area of focus at capillary exit}}{\text{power in } 1/e^2\text{-area of focus at capillary entrance}}$$

The stabilization analysis (Fig. 1) showed a jitter reduction of the relative ignition time from several μs to $\sim$20 ns for the whole voltage range by preionizing the hydrogen in the capillary. Without preionization this stable behavior of the high voltage discharge was achieved only for an applied voltage of 14 kV (jitter $\sim$30 ns).
In the experiment we achieved the guiding of a low power HeNe-laser in the preformed plasma channel (with preionization) with optimal guiding properties $\sim$40 ns after the onset of the high-voltage discharge. Quality values up to 65 % have been reached in this region as displayed in Fig. 2a. The evolution of the exit mode in the different guiding regions is shown in Fig. 2b. A comparison of the focus at the capillary entrance and the guided focus (region 2) shows a slight broadening ($\sim$15 %) of the focus at the capillary exit.

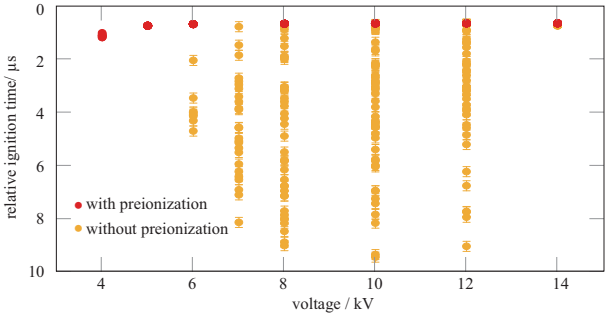

Figure 1: Behavior of the relative ignition time as a function of voltage with and without preionization.

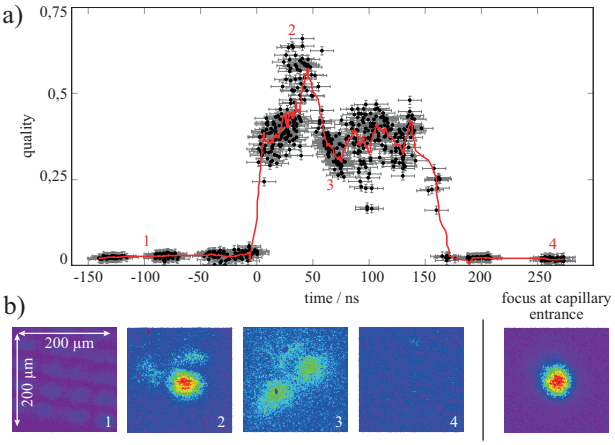

Figure 2: (a) Quality of the exit focus as a function of time. t=0 marks the onset of the high-voltage discharge. (b) Entrance mode and mode quality at the capillary exit belonging to regions 1 to 4.

For the usage of the capillary in an electron acceleration campaign at the JeTi-200 laser system at the Helmholtz-Institute Jena, the high voltage unit will be optimized to further reduce the ignition time jitter to $\sim$1 ns...2 ns. At the system it will be possible to use a few-cylce probe-pulse [4] to image the plasma wave structure getting direct insight into electron acceleration in a capillary waveguide [5].

References

[1] T. Tajima et al., Phys. Rev. Lett. 43, 267–270 (1979).

[2] D.J. Spencer et al., J. Phys. B 34, 4103 (2001).

[3] C. Wirth, Masterarbeit, IOQ, FSU Jena (2016).

[4] M. B. Schwab et al., Appl. Phys, Lett. 103, 191118 (2013).

[5] A. Sävert et al., Phys. Rev. Lett. 115, 055002 (2015).

Laser-scattering from near-ciritcal plasmas*

A. K. Arunachalam†[1,2], *M. B. Schwab*[1], *and M. C. Kaluza*[1,2]

[1]Helmholtz-Institute Jena, Jena, Germany; [2]Institute of Optics and Quantumelectronics, Jena, Germany

Preferential side-scattering has been observed during the interaction between an intense laser pulse and under-dense argon plasma. The scattering angle is found to decrease for increasing electron densities ranging from $0.01 - 0.25 n_c$ (n_c - critical density). We show that the scattering process results from the non-uniform density distribution of the gas-jet with the scattering angle being oriented along the direction of the resulting electron density gradient.

Laser-Plasma experiment

In order to deepen our understanding of the laser-plasma interaction dynamics at near-critical densities, an experiment has been carried out at the high-power laser JETI-40 in Jena. In this experiment, the laser pulses were focused using an $f/6$ off-axis parabola into an argon gas-jet, where a peak intensity of up to 4.4×10^{19} W/cm^2 was reached. The backing pressures of the gas-jet was varied from $5 - 80$ bar. The laser-plasma interaction region was backlighted using a 2ω probe beam at $90°$ to the laser's propagation direction and imaged onto a CCD-camera, of which a typical image is shown in fig. 1(a). It shows the phenomenon of side-scattering occurring preferentially on one-side of the laser-plasma interaction region (upwards).

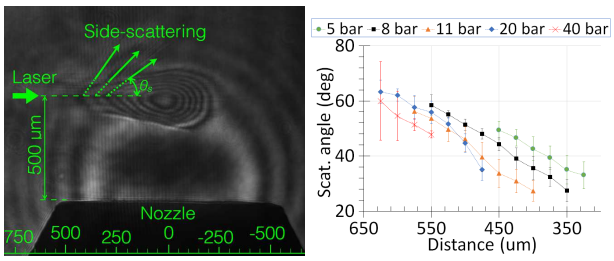

(a) (b)

Figure 1: (a) Side-view image of the interaction region obtained using the probe beam, and (b) corresponding side-scattering angle measured for varying backing pressures.

As the laser pulse propagates from the outer edges of the gas-jet towards its centre, the scattering-angle decreases invariably for pressures ranging from $5 - 40$ bar, as shown in fig. 1(b). Such a scattering process has been previously reported[1], where it has been attributed to Raman scattering. Here, we show that for our experimental conditions the scattering process is a result of the non-uniformity of the gas-jet.

Gradient analysis

The non-uniformity of the gas-jet is best captured by the direction of its gradient along the laser-axis. In the absence of any direction measurement, the plasma-density is calculated from the gas-density based on the argon's ionization energies. A comparison of the measured scattering angle for 20 bar against the plasma and gas density gradient directions, as shown in fig. 2(a), indicates that the scattering occurs along the direction of the plasma-density gradient originating from the central interaction region.

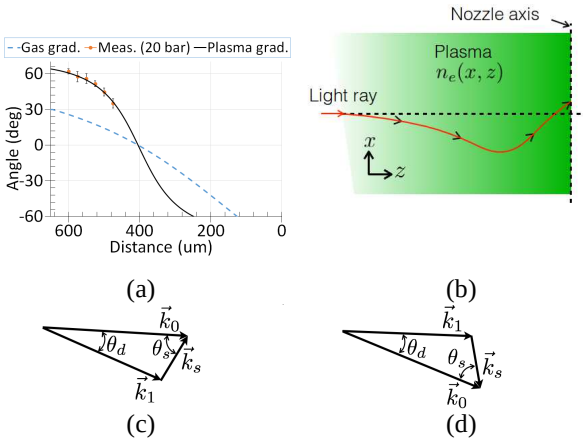

Figure 2: (a) Direction of the plasma and gas density gradient along with the scattering-angle measured for 20 bar, (b) representation of a light-ray propagation in a non-uniform plasma, (c) and (d) phase-matching conditions for positive and negative scattering.

The scattering process can be viewed as a consequence of the momentum conservation of the laser pulse entering the gas-jet. Fig. 2(b) shows the path of a light-ray ($\vec{k}_0$) in a non-uniform plasma-density distribution. If it were to represent the laser pulse entering the gas-jet, the phase-matching conditions shown in fig. 2(c) and (d) show that its deflection ($\vec{k}_1$) on either side of the laser-axis ought to result in an addition wave-vector component ($\vec{k}_s$), which can be viewed as the scattered wave.

References

[1] T. Matsuoka *et al.*, "Stimulated Raman Side Scat. in Laser Wakefield Accel.", Phys. Rev. Lett. 105, 034801 (2010)

* Work supported by HI Jena and IOQ Jena.

† ajay-kawshik.arunchalam@uni-jena.de

An analytical study on the rear side terahertz emission during laser-solid interaction

S.Herzer[1], *G.G.Paulus*[1,2], *and A.Gopal*[*1,2]

[1]Institute of Optics and Quantum Electronics, Friedrich-Schiller University, Max-Wien Platz 1, 0-7743, Jena;
[2]Helmholtz Institute Jena, Fröbelstieg 3, 07743, Jena

Intense electromagnetic radiation in the terahertz frequency regime are generated during high-power laser-solid interaction. Emission from the interacting surface occurs due to various linear and non-linear processes. Here we study two mechanisms contributing to the terahertz emission from the target rear surface.

Introduction

Coherent electromagnetic radiation covering a broad spectral range is emitted during high-power laser-matter interaction. High frequency radiation generation during such an interaction has been extensively studied and is well reported in the literature. Recent works at our institute and elsewhere have confirmed that low frequency radiation extending upto the mm regime can also be efficiently generated[1, 2]. Experimental observations reported the generation of few tens of micro joules from the target front surface, whereas above 700 micro Joules from the rear surface. Although the less intense emission from the interaction side is widely understood, the intense rear surface emission is yet to be fully explored in detail. Here we study the latter by analyzing the particle dynamics at the rear surface.

Methods & Discussion

During laser-plasma interaction, an ultra intense laser pulse ($I_L \geq 1\times10^{19}$ W/cm^2) hitting a thin foil target generates a hot electron plasma mainly through the mechanism of ponderomotive scattering[3]. Some of the generated electrons can gain energy in the laser field and travel through the target to exit at the rear surface. These hot electrons are responsible for generating a micron size plasma sheath with a quasi static field of magnitude comparable to the transverse laser electric field, which in turn ionize the atoms at target rear side and accelerate the ions in target normal direction. A closer look at the particle dynamics at the rear surface will provide a clearer picture of the radiation emission. Here we consider two radiation emission process at the rear surface. Firstly, transition radiation(TR) is generated when the electrons exist at the rear surface due to the change in dielectric properties of the mediums. Earlier works have reported the observation of optical and higher frequencies very close to the target normal direction. The contribution from the TR is calculated by considering the difference between the two inhomogeneous solutions of Maxwell equations of the electro magnetic fields of the moving charge in each medium separately. Following the theoretical treatment of Ginzburg-Frank[4], the angular distribution of the CTR is shown in Figure 1(left).

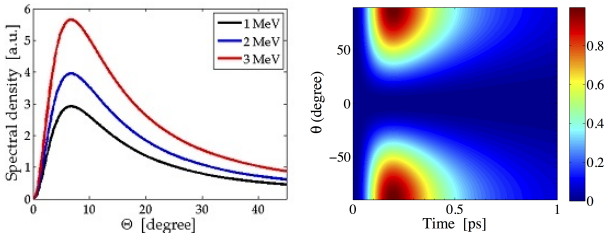

Figure 1: Angular distribution of the CTR (left) and SR by an adiabatic expanding plasma(right)

The second contributor to the rear side emission is the transient sheath acceleration process (SR). The emitted radiation is calculated by inserting the terms for charge dynamics in the plasma sheath[5] into the Lienard-Wiechert potential to obtain the radiation profile. For our study, the experimental parameters from the JETI laser system are considered.The angular power distribution for incident laser intensity$I_L \sim 10^{19}$ W/cm^2 is presented in Figure 1 (right). Most of the energy is emitted in large angles with respect to the target normal, implying dipole-like radiation pattern. Considering an initial electron temperature $k_{\mathrm{B}}T_{\mathrm{e}}$ = 2MeV and a density $n_e = 5\times10^{19}$cm^{-3} leads to a pulse duration $\tau \approx 412$fs. Spectral analysis reveal that most of the energy is emitted below 3 THz agreeing well with the experimental results [6].

Conclusion

In conclusion, a simple analytical model has been used to study the terahertz emission from the rear surface of a solid target during high-power laser matter interaction. Two possible sources have been discussed, a) TR radiation due to the electron bunch crossing the plasma vacuum boundary and b) SR due to the transient dynamics of the plasma sheath formed at the rear surface or the target normal sheath acceleration process, which generates terahertz radiation in the non-collinear direction.

References

[1] A.Gopal *et al.*, Opt.Lett. **38**, 4705, PRL. **111**, 074802 (2013).

[2] C.Li *et al.*, Phys.Rev.E **84**, 036405 (2011).

[3] S.C.Wilks *et al.*, Phys. Plasmas. **8**, 542, (2001).

[4] V.L.Ginzburg and I.M. Frank, Sov. Phys. JETP **16**, 15 (1946).

[5] P.Mora, PRL. **90**, 185002 (2003), PRE **72**, 056401 (2005).

[6] S.Herzer *et al.*, submitted

* amrutha.gopal@uni-jena.de

Characterizing High Power Terahertz Radiation from Relativistic Laser-Solid Interaction

A. H. Woldegeorgis[1,2,#], G. G. Paulus[1,2] and A. Gopal[1,2]

[1]Institut für Optik und Quantenelektronik, Friedrich-Schiller-Universität Jena, Germany; [2]Helmholtz-Institut Jena, Germany.

The quest for intense terahertz (THz) sources is growing significantly owing to their numerous applications in nonlinear THz optics and spectroscopy, particle acceleration, biological imaging and so on. Researchers have already demonstrated the generation of sub-picosecond broadband THz pulses with energy up to 700 µJ from the rear side of a thin solid target irradiated by high intensity laser pulses [1,2]. However, to fully harness the potential of this powerful source, a thorough understanding of the radiation mechanisms and full characterization of the radiation are of vital importance. To this aim, we performed an investigation on THz radiation emitted from the rear side of a thin foil during a relativistic laser-solid interaction. The dependence of the THz yield as well as the temporal and spectral properties of the THz pulses on the incident laser pulse parameters and target properties have been studied.

The experiment was conducted at the JeTi40 laser facility which delivers pulses of 1J energy in 30 fs duration at a central wavelength of 800nm. The laser pulses were focused using an f/1.2 off-axis parabolic mirror (OAP), producing intensities $>10^{19}$ W/cm^2, onto the thin foil target. Titanium, polyethylene and aluminum foils were used as a target. An ellipsoidal mirror and 90° OAP were employed to collect and collimate the noncollinear emission whereas the forward emission was collected and collimated using a 90° OAP.

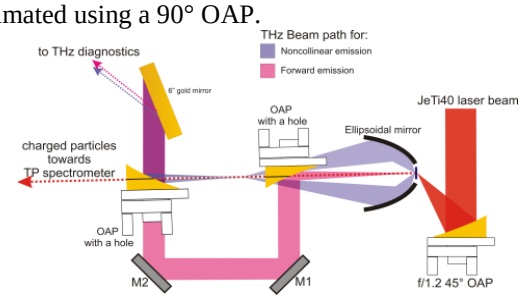

Fig. 1: Schematic of the experimental setup.

The collimated radiation from both emissions is steered out of the experimental chamber by a set of metallic mirrors towards the THz diagnostics. Simultaneously, the ion spectra were recorded using a Thomson parabola spectrometer. A calibrated pyroelectric detector measures the integrated THz pulse energy. A noncollinear electrooptic setup measures the THz temporal waveform, peak electric field and spectrum in a single-shot.

Among the numerous data collected during the experimental campaign, here we only present preliminary results showing the THz yield scaling as a function of the laser intensity. The laser intensity was varied by changing either the pulse energy or the duration at a time; the focusing conditions were kept the same. In fig. 2 the laser intensity scan was done by varying the on-target laser energy between 0.2 J and 0.7 J while the pulse duration remains unaltered. The THz signal scales with $I^{1.4\pm0.2}$ and shows no sign of saturation, but limited only by the available laser energy. The proton cutoff energy, which scales as $I^{0.6\pm0.1}$, slightly diverges from the well-established scaling with an exponent of 0.5.

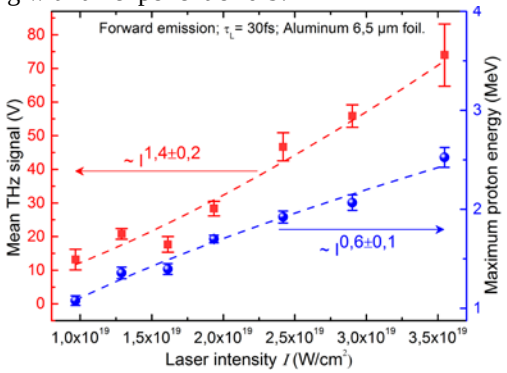

Fig. 2: Scaling of THz yield (forward emission) and proton cutoff energy vs laser intensity (only the pulse energy was varied).

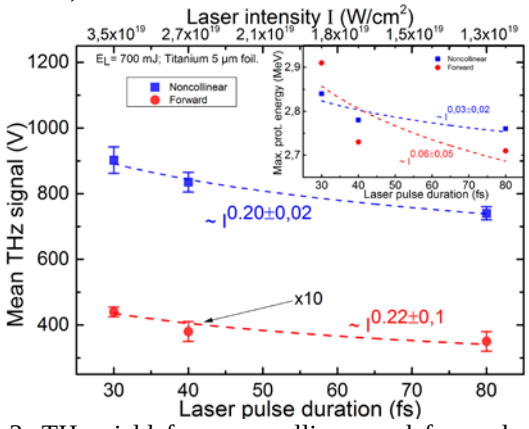

Fig. 3: THz yield from noncollinear and forward emissions for different laser pulse durations. Inset shows the proton cutoff energy vs. laser pulse duration.

In fig. 3 the laser intensity was varied by changing the pulse duration while keeping the energy constant at 0.7 J. The power-law fits show a different intensity scaling for the THz yield compared to the one in fig. 2. It can be observed that varying the pulse duration did not have a strong impact on both the THz signal and the proton cutoff energy. The THz emitted in the noncollinear direction is higher than the forward emission by a factor of 20; however, to make a reasonable comparison, the solid angles of the collection optics have to be considered. Beam profile measurements have already been done and will address this issue in an upcoming publication.

References

[1] Gopal, A. *et al.* Phys.Rev.Lett. **111** 074802 (2013).

[2] Gopal, A. *et al.* Opt.Lett. **38**, 4705 (2013).

abel.woldegeorgis@uni-jena.de

Photon and Particle Spectroscopy

First results of the SHHG commissioning experiments at the JETI200 laser facility

B. Walter[*1,2], *K. C. Saraswathula*[1], *R. McHugh*[1,2], *G. Schäfer*[1], *L. Li*[3], *A. Sävert*[1,2], *D. Ullmann*[†1], *M. Yeung*[3], *A. Kessler*[1], *M. M. Günther*[1], *M. C. Kaluza*[1,2], *and M. Zepf*[1,2,3]

[1]Helmholtz Institute Jena, Germany; [2]Institute for Optics and Quantum Electronics, FSU Jena, Germany; [3]Department of Physics and Astronomy, Queen's University Belfast, UK

In the past year, the JETI200 laser facility has been successfully commissioned resulting in first generation of surface harmonics at this new facility. Recent results of the commissioning experiments with laser energies up to 2.1 J and pulse durations as low as 24 fs are presented. There is clear evidence that JETI200 is capable of applying higher intensities than JETI40 in contrast-sensitive experiments even by the initial experimental results.

Since surface high-harmonic generation (SHHG) is especially sensitive on the intensity contrast of the laser, SHHG experiments were carried out in order to benchmark and enhance the performance of the JETI200 laser facility. Because the first shots on target in June 2016 proved insufficient contrast, a single plasma mirror device was implemented and characterized, consequently, as it has been shown to principally act as a few-hundred-femtosecond switch, capable of reducing the intensity contrast by three orders of magnitude [1, 2, 3].

The following experimental campaign resulted in the first-ever observed harmonic spectra using the JETI200 laser. Unfortunately, the harmonic signal was non-reproducible and unstable due to both the laser being unstable after a long period of operation and still insufficient intensity contrast evident in most of the spectra. Thus, the laser was maintained thoroughly and additional beam characterization installations were undertaken to facilitate more convenient control over the laser beam and to allow for extensive measurements of various pre-pulse levels. Those measurements were carried out subsequently, yielding a detailed temporal characterization of JETI200's intensity contrast.

Finally, the femtosecond contrast, measured directly before the target chamber, has proved to be crucial to the generation of harmonics at JETI200. Achieving levels better than $2 \cdot 10^{-4}$ at -400 fs and $6 \cdot 10^{-4}$ at -150 fs, clear and stable harmonics have been generated in every further experimental campaign even though relativistically oscillating mirror (ROM) harmonics were present in every spectrum indicating contrast levels higher than desired. By implementing a pre-pulse mirror (PPM) in order to create a well-controlled pre-pulse a few picoseconds before the main-pulse one can influence the efficiency of the ROM generation and find the respective optimum [4]. This was used as a tool to investigate if the contrast is at least good enough to perform first SHHG experiments.

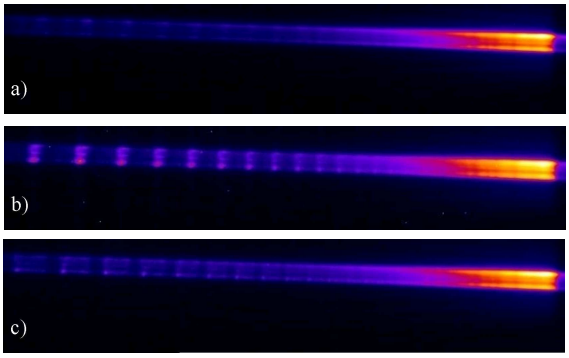

Figure 1: Harmonic lines generated using the JETI200 laser on a Jasny spectrometer influenced by an intentionally induced pre-pulse with delays of a) 0 ps, b) -3 ps and c) -5 ps, respectively. The energy on target was 625 mJ at a pulse-duration of 24 fs resulting in $6.5 \cdot 10^{19}$ W$\cdot$ cm^{-2} in focus.

As shown in fig. 1, the intensity and efficiency of the harmonics could be increased initially by worsening the picosecond contrast, thus increasing the plasma scale-length (fig. 1 b)). Further increase of the scale-length then leads to decreasing harmonic intensity (fig. 1 c)). This behavior of the harmonic intensity proves that the current contrast level of JETI200 is at least good enough to reach the scale-length optimum for the energy used by worsening the contrast with a PPM. Since the laser energy before compressor was 1.4 J, thus higher than the maximum energy of JETI40 using similar focussing and having similar pulse-duration and transmission including compressor, beam-line, and plasma mirror, JETI200 proved the capability of applying higher intensities in contrast-sensitive experiments.

Detailed parameter scans such as pre-pulse scaling using higher energies are still to be completed in order to fully benchmark the performance, as well as further experiments beyond benchmarking.

References

[1] B. Dromey, et al., Rev. Sci. Instrum. 75, 645 (2004)

[2] G. Doumy, et al., Phys. Rev. E 69, 026402 (2004)

[3] C. Rödel, et al. Appl. Phys. B (2011) 103: 295

[4] S. Kahaly, et al., PRL 110, 175001 (2013)

* bastian.walter@uni-jena.de

† Now: Department of Physics, University of Strathclyde, Glasgow, UK

Matter and Light: Unite!

K. S. Schulze[1,2], J. Haber[3], K. Schlage[3], R. Loetzsch[2], L. Bocklage[3], T. Guryeva, H. Bernhardt[1], H.-C. Wille[3], R. Rüffer[4], I. Uschmann[1,2], G. G. Paulus[1,2] and R. Röhlsberger[3]

[1]Helmholtz Institute Jena, Germany; [2]Friedrich-Schiller-Universität Jena, Germany; [3]Deutsches Elektronen Synchrotron DESY, Germany; [4]European Synchrotron Radiation Facility ESRF, Grenoble, France.

When light interacts with matter, it may be deflected or absorbed, resulting in the excitation of atoms and molecules; but the interaction can also produce composite states of light and matter, which are neither one thing nor the other, and therefore have a name of their own – polaritons. These hybrid particles have now been prepared and accurately measured for the first time in the field of hard X-rays by researchers of DESY, ESRF, University of Jena and Helmholtz Institute Jena [1]. The polaritons are created by the interaction of X-rays produced by the synchrotron ESRF with a periodic stack of alternating layers of different iron isotopes: the Mössbauer isotope iron-57 (^{57}Fe) and the non-resonant, most commonly occurring isotope of iron ^{56}Fe. Each layer was less than two nanometers thick. If the wavelength of the X-rays are tuned to the extremely narrow nuclear resonance of ^{57}Fe at an energy of 14.4 keV, the multilayer system acts as a Bragg reflector. Classically, one would expect that the different dispersion relations of the Bragg reflection and the nuclear resonance overlap. However, strong coupling of the X-rays with the nuclei lead to an anti-crossing in the dispersion curve, which shows the presence of polaritons (see figure). This can also be regarded as a creation of two different resonances, which are separated by only 37.3 neV.

The precise measurement of these extremely small spectroscopic features was enabled by a high-purity X-ray polarimeter [2], which was developed in Jena. Depending on the magnetization of the sample, the photons scattered at the nuclei change their polarization. Thus, these photons can pass the polarimeter with polarizer and analyzer in crossed position, whereas the non-resonant, specular reflected photons are suppressed by about eight orders of magnitude. This leads to a separation of the signal from the background with a very high degree of sensitivity. The method already enabled the discovery of quantum optical effects in the past [3,4].

The preparation and measurement of polaritons in the X-ray range is an important step on the path to tailored radiation fields in the X-ray range. The simultaneous emission of many identical photons during the decay of nuclear polaritons could lead to extremely narrow-band, non-classical light sources in the X-ray range, and pave the way for new applications in high-precision spectroscopy. At the same time, the experiment is a further step towards establishing quantum optics in the X-ray domain.

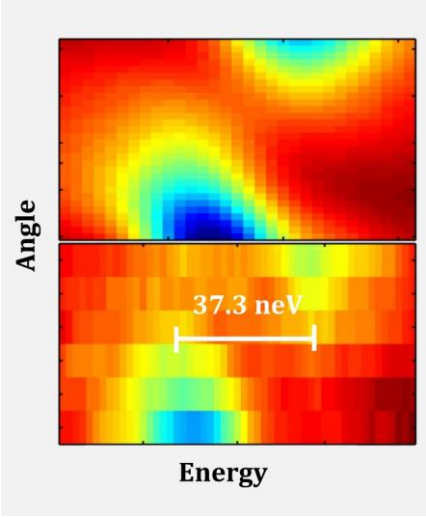

Figure 1: The simulated (top) and recorded (bottom) detector images display the intensity of the Bragg reflected X-rays for different angles and photon energies. The splitting of the resonance due to the formation of polaritons is just 37.3 neV.

References

[1] J. Haber, K. S. Schulze, K. Schlage, R. Loetzsch, L. Bocklage, T. Guryeva, H. Bernhardt, H.-C. Wille, R. Rüffer, I. Uschmann, G. G. Paulus and R. Röhlsberger, "Collective strong coupling of X-rays and nuclei," Nature Photonics, 2016.

[2] B. Marx, I. Uschmann, S. Höfer, R. Lötzsch, O. Wehrhan, E. Förster, M. Kaluza, T. Stöhlker, H. Gies, C. Detlefs, T. Roth, J. Härtwig, and G.G. Paulus, "Determination of high-purity polarization state of X-rays", Optics Communications 284: 915-918, 2011.

[3] K. P. Heeg, H.-C. Wille, K. Schlage, T. Guryeva, D. Schumacher, I. Uschmann, K. S. Schulze, B. Marx, T. Kämpfer, G. G. Paulus, R. Röhlsberger, and J. Evers, "Vacuum-Assisted Generation and Control of Atomic Coherences at X-Ray Energies", PRL 111, 073601, 2013

[4] K. P. Heeg, J. Haber, D. Schumacher, L. Bocklage, H.-C. Wille, K. S. Schulze, R. Loetzsch, I. Uschmann, G. G. Paulus, R. Rüffer, R. Röhlsberger, and J. Evers, "Tunable sub-luminal propagation of narrow-band x-ray pulses", PRL 114: 203601, 2015

High purity x-ray polarimetry with single-crystal diamonds

H. Bernhardt[1,2], B. Marx-Glowna[1], K. S. Schulze[1,2], B. Grabiger,[1,2] J. Haber[3], C. Detlefs[4], R. Lötzsch[1,2], R. Röhlsberger[3], E. Förster[1,2], T. Stöhlker[1], I. Uschmann[1,2], G. G. Paulus[1,2]

[1]Helmholtz-Institut Jena, Germany; [2]Institut für Optik und Quantenelektronik, FSU Jena, Germany; [3]Deutsches Elektronen Synchrotron DESY, Germany; [4]European Synchrotron Radiation Facility ESRF, France.

The polarization rotation of light in a sucrose is still one of the most famous experiments in optics, revealing the chirality of complex molecules. In the x-ray regime, applications based on polarization effects are becoming increasingly significant. One prominent example is x-ray magnetic circular dichroism. More recently, the development of high-performance x-ray polarizers for crossed polarizer/analyzer setups expanded the applications of nuclear resonant scattering and even enabled the detection of optical activity of sugar at a photon energy of 12.9 keV [1]. In order to detect such polarization effects in the x-ray range, appropriate instruments with high angular resolution near the extinction position are essential. Further improvements of x-ray polarizers will likely yield new physical insights and open up experiments like the detection of vacuum birefringence [2].

Polarized X-rays

Light can generally be polarized by using a reflection at the Brewster angle, which is very close to 45° in the x-ray regime. In addition, very high reflectivities for x-rays are achieved when the Bragg condition is fulfilled, which means that the path difference $2d \cdot \sin(\theta_B)$ of two reflected beams under a Bragg angle θ_B has to be a multiple of the wavelength lambda λ. In order to obtain extremely pure polarization states, special channel-cut crystals are used, where the radiation is reflected two, four or six times at the walls of a groove cut inside a crystal. Thereby, polarization purities or intensity ratios of 10^{-10} between the two linear polarization components π and σ can be achieved.

The advantages of diamond

The reachable polarization purity is limited by multiple-beam cases, in which the incident beam excites a secondary reflection. A part of the intensity of the unwanted polarization component π is then reflected via Umweganregung in the direction of the desired beam, which degrades the polarization purity. These multiple-beam cases are weaker in crystal materials with smaller atomic number Z, which renders it interesting to use diamond for x-ray polarizers. Due to their unique physical properties such as low x-ray absorption, high thermal conductivity, and high x-ray reflectivity, diamond has also become very attractive for use as monochromator crystals in high power density beamlines, as material for phase plates, beam splitters and as self-seeding crystals in FEL technology.

A new crystal holder

In the absence of large and perfect diamond crystals, it is not possible to manufacture a monolithic diamond channel-cut crystal. Thus, we developed a special crystal holder to realize the channel-cut geometry with two separate chemical vapor deposited diamond crystals. Most parts of this quasi-channel-cut (QCC) holder are made out of invar steel to minimize thermal expansion. As shown in Figure 1, the first crystal is fixed whereas the second one is attached to a mirror mount allowing a parallel alignment of both crystals. In addition a piezo element can be used for very precise adjustment.

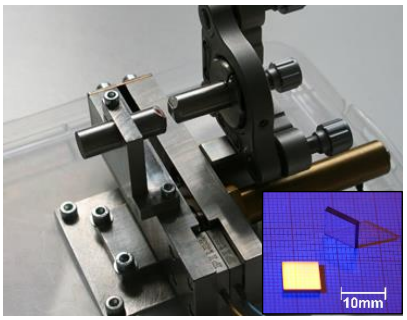

Fig. 1: Quasi-channel-cut-holder with diamond crystals, inset: two diamond crystals 8x8x1.2mm^3

Results

A highly polarized x-ray beam was produced and a polarization purity of

$$\frac{I_\pi}{I_\sigma} = 8.9 \cdot 10^{-10}$$

was measured by using two of these holders as polarizer and analyzer. This purity is the best value reported for two-reflection polarizer/analyzer setups and a first step to improve the resolution of x-ray polarimeters further by using diamond crystal QCC's with four or six consecutive reflections. The experiment was carried out at the European Synchrotron Radiation Facility at beamline ID06 with a photon energy of 9838.75eV [3].

References

[1] B. Marx, K. S. Schulze, I. Uschmann, T. Kämpfer, R. Lötzsch, O. Wehrhan, W. Wagner, C. Detlefs, T. Roth, J. Härtwig, E. Förster, T. Stöhlker, G. G. Paulus, "High-precision x-ray polarimetry", Physical Review Letters 06/2013; 110(25):254801.

[2] T. Heinzl, B. Liesfeld, K. Amthor, H. Schwoerer, R. Sauerbrey, A. Wipf, "On the observation of vacuum birefringence", Optics Communications 267 (2006) 318–321

[3] H. Bernhardt, B. Marx-Glowna, K. S. Schulze, B. Grabiger, J. Haber, C. Detlefs, R. Lötzsch, T. Kämpfer, R. Röhlsberger, E. Förster, T. Stöhlker, I. Uschmann, G. G. Paulus, "High purity x-ray polarimetry with single-crystal diamonds", Appl. Phys. Lett. 109 (2016) 121106

Ultra high precision refractive index measurement at γ-ray energies up to 2 MeV

M. M. Günther[#,1,2], *M. Jentschel*[3], *A. J. Pollitt*[3], *P. G. Thirolf*[4], *M. Zepf*[2,5,6]

[1]GSI Helmholtzzentrum für Schwerionenforschung GmbH, Darmstadt, Germany; [2]Helmholtz-Institut Jena, Jena, Germany; [3]Institut Laue-Langevin, Grenoble, France; [4]Ludwig-Maximilians-Universität, München, Germany; [5]Queen's University Belfast, Belfast, United Kingdom; [6]Friedrich-Schiller-Universität, Jena, Germany.

For the first time the refractive index of Materials with different atomic charge numbers (from Z=4 to Z=82) were investigated at γ-ray energies from 181 keV to 2 MeV. The experiments were performed at the new γ high resolution double crystal spectrometer GAMS6 at the Institut Laue-Langevin (ILL) in Grenoble. The work was performed by the collaboration of the HI Jena, the ILL in Grenoble and the LMU in Munich. The refractive index is a sensitive observable to study fundamental interaction processes. The relation is given via the complex forward atomic scattering amplitude, where the real part is related to the real part of the complex refractive index n=1+δ+iβ. Information on the γ refractive index was only accessible via the extrapolation of the classical scattering model. Since the underlying interactions and scattering physics change in relative importance with increasing photon energies, the question arises up to which energy the extrapolation remains valid. The development of highly brilliant tunable γ-ray sources further motivates this research. Certain applications envisaged on these facilities such as nuclear resonance fluorescence (NRF) based experiments etc. would benefit significantly from focusing optics in the MeV regime. Therefore, from a fundamental, but also applied physics point of view, it is important to establish a reliable experimental knowledge of the refractive properties at γ-ray energies.

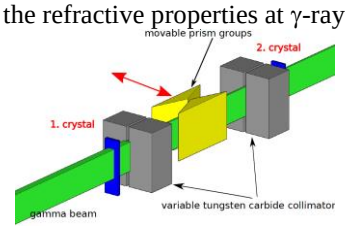

Figure 1: Schematic of the experimental setup.

The concept of the refractive index measurement is based on prism optics. The principle consists in i) defining a low-divergence monochromatic photon beam, ii) deflecting it via refraction at the interfaces of a prism and iii) measuring the deviation angle with respect to the incident beam. These principle points are realized in detail using GAMS6 (see [1] for more details). An optical heterodyne Michelson interferometer is used for high resolution angle measurements. The angular resolution is about 10^{-9} radian. After propagation of the beam through the two crystals the angular intensity profile is scanned by rocking the 2. crystal around Bragg's angle and measuring the transmitted intensity by a HPGe detector. The centre of the rocking curve presents the angular position of the beam. The γ beam is generated by neutron capture processes of an in-pile Gd_2O_3 target close to the nuclear fission reactor core. The γ emission rate is about 10^{17} γ/s. After collimation a small beam reaches GAMS6, where the flux is 10^9 γ/s. By moving the prism groups (fig. 1) right and left, prism pairs refract the beam in opposite directions, enhanced the deviation angle.

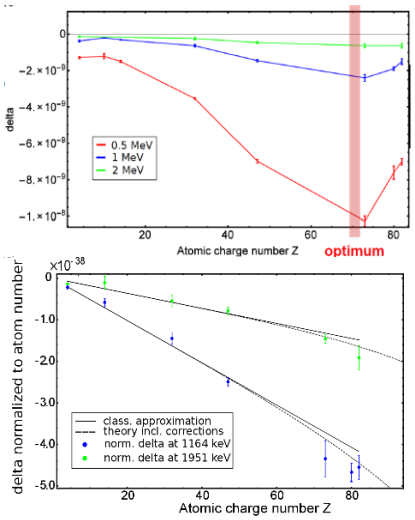

Figure 2: (preliminary) Z dependency of δ is shown for several γ energies: Be, SiO_2, Si, Ge, Ag, Ta, Hg (fluid), and Pb were used. Materials within the optimum range are suitable for γ refractive optics ($\delta=-10^{-8}$ – -10^{-9}). In the lower panel is shown that a slight deviation from classical model was observed for High Z and high energies.

First conclusions of the experimental campaign are (see fig. 2): i) refractive index at γ energies up to 1 MeV is suitable for the realization of γ refractive optics. In a future experimental campaign novel γ optics will be tested for a new imaging technique. ii) dispersive behaviour as well as the Z dependency is different to the classical model for high energies and high Z materials (Ta, Hg, Pb), but follow the classical model at low Z and low γ energies.

More details of the experiments and a re-evaluation of data from Silicon refractive index measurements at the older GAMS5 are presented in [1]. In an upcoming paper the reason for the slight deviation from classical model will be discussed.

References

[1] M. M. Günther et al., arXiv:1702.07023[physics.atom-ph] (2017). Submitted to Phys. Rev. A

[#]m.guenther@gsi.de

Time-resolved observation of a sub-200 fs graphitization of diamond*

F. Tavella[1], *H. Höppner*[2], *V. Tkachenko*[3], *N. Medvedev*[3], *the FERMI collaboration*[4], *M. J. Prandolini*[†5], *S. Toleikis*[2], *and B. Ziaja*[3]

[1]SLAC, Menlo Park, USA; [2]DESY, Hamburg, Germany; [3]Center for Free-Electron Laser, Hamburg, Germany; [4]Elettra-Sincrotrone Trieste, Trieste, Italy; [5]Helmholtz-Institut Jena, Jena, Germany

Soft x-rays were applied to induce graphitization of diamond through a non-thermal solid-to-solid phase transition. This process was observed within polycrystalline diamond with a time-resolved experiment using ultrashort soft x-ray pulses of duration 52.5 fs and cross correlated by an optical pulse of duration 32.8 fs. This scheme enabled for the first time the measurement of a phase transition on a timescale of $\sim$150 fs.

The method used to observe ultrafast graphitization of diamond is based on solid-state target EUV/optical cross-correlation [1]. With this approach, a 47.4 eV FEL pulse is used to induce the transition from diamond to graphite. The wavefront of the FEL is tilted with respect to the target; thus the integrated FEL fluence is encoded spatially and temporally onto the surface of the target. The subsequent temporal evolution of the graphitization process is monitored by a probe laser with a wavefront parallel to the target. The experiment was carried out at the DiProI beamline at the FERMI free-electron laser. Details on the experimental setup and beam parameters are available in [2].

Initially measurements were performed below the graphitization threshold, in order to measure the FEL pulse duration, define the time overlap between the FEL pulse and the optical probe pulse and to measure the threshold for damage (graphitization). Thereafter measurements were performed above the graphitization threshold to investigate the underlying dynamics. We observed onset of graphitization on diamond at fluence values >0.1 J/cm^2 in agreement with previous estimates (see references in [2]).

Fig. 1 shows a typical optical cross-correlation data for a FEL fluence above the graphitization threshold. The transmission curve was normalized to the initial transmission of non-irradiated diamond. It exhibits a few characteristic features which reflect three different stages of graphitization, modeled by the in-house simulation tool, XTANT (see references in [2]). First, the electrons emitted after FEL photoabsorption excite a sufficient number of electrons into the conduction band via collisional processes. Second, the high number of electrons excited to antibonding states weakens interatomic bonds, which leads to a band gap collapse. This occurs within $\sim$50 fs after the FEL pulse maximum. Third, the band gap collapse promotes even more electrons into the conduction band, weakening the interatomic potential within the diamond lattice. Interatomic bonds are then breaking and forming sp2 bonds instead of sp3. Finally, diamond graphitization completes within the next 50–100 fs.

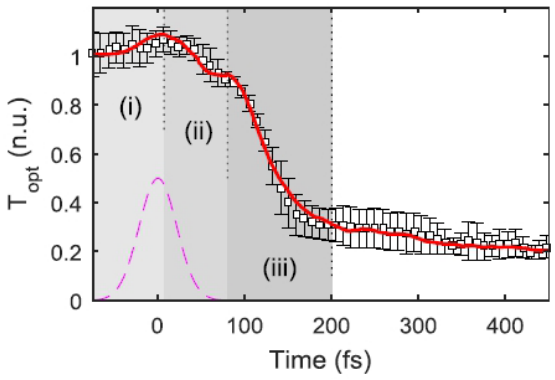

Figure 1: Cross-correlation measurement of ultrafast graphitization: experimental (open black squares with error bars) and theoretical (red line). FEL photon energy was 47.4 eV, pulse duration was 52.5 fs (FWHM, magenta line). Intervals (i)-(iii) denote different stages of graphitization.

We would like to emphasize that the induced phase transition is of non-thermal nature. It is caused solely by the modification of the interatomic potential and not by atomic heating via electron-phonon coupling. Our model predicts that the electron-phonon coupling acts at picosecond scales. During the graphitization process reported here (which occurs within $\sim$150 fs), the contribution of heating by electron-phonon coupling is only minor. Moreover, we have verified that if in our theoretical model we 'switch off' the electron-phonon coupling, the results remain the same.

This time-resolved experiment confirms for the first time the occurrence of a direct solid-to-solid ultrafast phase transition induced by a non-thermal modification of the potential energy surface. This finding is important both for fundamental research and for technological applications of diamond as a nanomaterial.

References

[1] R. Riedel, A. Al-Shemmary, M. Gensch, T. Golz, M. Harmand, N. Medvedev, M. J. Prandolini, K. Sokolowski-Tinten, S. Toleikis, U. Wegner, B. Ziaja, N. Stojanovic, and F. Tavella, Nat. Commun. **4**, 1731 (2013).

[2] F. Tavella, et al., "Soft x-rays induced femtosecond solid-to-solid phase transition", arXiv:1612.06698 and submitted to Nat. Commun.

* Work supported by HI Jena

† mark.prandolini@desy.de

Laser-Induced Fragmentation of an Ion Beam of H_2^+ by High-Intensity Fields with Short-Wave Infrared Wavelength

M. Möller[*1,2], *P. Wustelt*[1,2], *Lun Yue*[3], *A. M. Sayler*[1,2], *Stefanie Gräfe*[3], *and G. G. Paulus*[1,2]

[1]Helmholtz Institut Jena, Germany; [2]Institute for Optics and Quantum Electronics, Friedrich-Schiller-University Jena, Germany; [3]Institute for Physical Chemistry, Friedrich-Schiller-University Jena, Germany

In this project, we experimentally and theoretically investigate laser-induced fragmentation of an ion beam of the simplest molecule in nature, i.e. the hydrogen molecular ion, H_2^+, by high-intensity laser fields with short-wave infrared wavelength (SWIR, $1\mu m - 2.5\mu m$), femtosecond pulse duration and peak intensities up to few $10^{15} W/cm^2$.

The H_2^+ ion represents the benchmark system for the theoretical understanding of the molecular bond and related couplings between electronic and nuclear dynamics of small molecules. Interaction with strong laser fields causes to two different fragmentation reactions, i.e. strong-field photodissociation $H_2^+ \rightarrow H + H^+$ and photoionization $H_2^+ \rightarrow H^+ + H^+ + e^-$. Inducing both with intense SWIR fields, represents an interesting situation where the electronic motion is forced to the time scale of the laser's optical period of several femtoseconds, e.g. 6.75 fs for $2\mu m$ during which the nuclei of a light molecule can significantly change their position. Accordingly, measurements in this regime promise the observation of interesting couplings between electronic and nuclear dynamics and thus, provide a test bed for their understanding. In addition to these fundamental interest in molecular dynamics, ionization and dissociation of small diatomic molecules is a common precursor for particle acceleration in laser-driven plasmas at relativistic intensities.

Figure 1: Two-dimensional histogram of the momentum distribution from strong-field photodissociation and photoionization of H_2^+ by a linearly polarized 65-fs-$2\mu m$ laser field with a peak intensity of $\approx 10^{15} W/cm^2$ in the plane of the polarization. The arrows and dots are representative for an individual dissociation (grey) and ionization event (red).

The ideal approach for studying such molecular dynamics from the theoretical side would be *ab initio* simulations of the time-dependent Schrödinger equation (TDSE) with methods that treat the electronic and the nuclear motions on equal footing. However, presently existing limits in computational power do not allow these simulations in the needed parameter space. Thus, several simplified concepts for the understanding of on-going electronic-nuclear dynamics exist whose predictions for SWIR laser wavelength deserve investigation.

For our measurements, the output of a high-power high-repetition laser is used to pump an optic parameteric amplifier that generates intense SWIR fields. These are then focused into the interaction region of the ion beam apparatus for laser-induced fragment momentum spectroscopy, which is regularly operated at HI Jena. Three-dimensional momentum distributions of the heavy fragments, i.e. of the momenta of the proton, p_{H^+}, and the Hydrogen atom, p_H, for dissociation and the two proton momenta, p_{H^+} and p_{H^+} for ionization, are measured as function of the laser parameters such as peak intensity, center wavelength and pulse duration.

An example for two-dimensional histogram of the momentum distribution is given in Figure 1. The laser field is linearly polarized and parallel to the x-axis of the plot. Arrows, symbols and dots are representative for one dissociation (grey) and one ionization (orange) event. The dissociation events are found in the center and have lower momenta as well as wider angular distribution. Ionization events have higher momenta and are narrower in angular distribution. Momentum conservation dictates that the center-of-mass (COM) of an individual dissociation is always equal to the initial momentum of the H_2^+ molecule before dissociation. Thus, $p_{H^+} + p_H \approx 0$, is a good approximation due to the well controlled ion beam target with low intitial momentum spread. The COM-kick of individual ionization events however, can be used to infer the electron momentum, p_e, using $p_{H^+} + p_{H^+} = -p_e$. Analysis of p_e gives the opportunity to analyze coupled electron-nuclear dyanmics during strong-field photoionization of H_2^+ by SWIR fields.

So-far, we have performed the measurement, are comparing the experimental data with theoretical expectations and prepare the results for publication [1, 2].

References

[1] M. Möller, P. Wustelt, L. Yue, F. Grossmann, A. M. Sayler, S. Gräfe, G. G. Paulus, *in preparation*

[2] P. Wustelt, M. Möller, L. Yue, A. M. Sayler, S. Gräfe, G. G. Paulus, *in preparation*

[*] max.moeller@uni-jena.de

Optical vortex diagnostics via ptychographic reconstruction

F. Tuitje[1,2]*, M. Zürch*[2,3]*, and C. Spielmann*[1,2]

[1]Helmholtz Institute Jena, Germany; [2]Institute for Optics and Quantum Electronics, FSU Jena, Germany; [3]Department of Chemistry, University of California, Berkeley, USA

Optical vortices (OV) are widely used either in high-resolution imaging as structured illumination to achieve the highest resolutions or in micro particle manipulation. Both applications rely on the their helical phase gradient. Beside the classical contributions to characterize an OV [1], we demonstrate a method of numerical reconstruction of the OV in phase and intensity via ptychographic reconstruction. This allows an in-situ characterization in experiments, which already use OV generated diffractograms.

An OV was generated via a computer generated pitchfork hologram (CHG), which ensures a spatial separation of OV and fundamental beam [2]. A topological charge (TC) of $m = 1$ was chosen to minimize discretization artifacts. The spatial filtered OV was focused down on a known sample. Implementating the ePIE algorithm we were able to reconstruct both the known complex object and the complex illumination function using a 20×20 sampling grid [3].
The reconstructed intensity after 15 iterations as seen in fig.1 shows a typical ring shaped intensity distribution with an outer FWHM of 32.4±0.4 μm, which matches the directly measured beam profile (37.1±0.4 μm), and an inner FWHM of 3.9±0.4 μm.

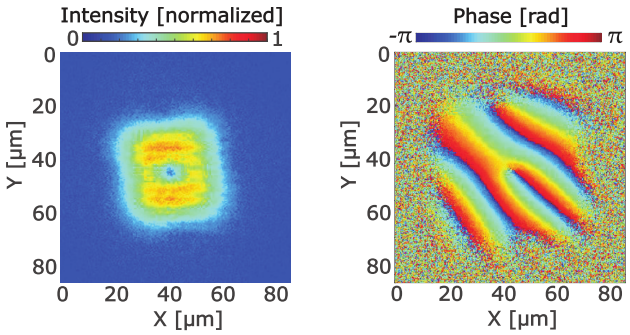

Figure 1: Reconstruction of the illumination function. The intensity distribution (left) shows the typical ring structure with the phase singularity in its dark center, which appears in the phase distribution (right) as the splitting region of the pitchfork.

The smaller inner FWHM, compared to the directly measured one (13.1±0.4 μm), is a result of the numerical reconstruction. The decreasing intensity in the vicinity of the phase singularity is a result of destructive interference. The algorithm has to keep the intensity to reconstruct the phases properly. The reconstructed phase appears as a pitchfork distribution, which is explainable with the reconstruction process itself. The ePIE algorithm probes the illumination function with plain waves, which outcomes as pitchfork like phases. To recover the helical phase distribution, the reconstructed phase was interfered with a plain wave as the counterpart of the OV generation (fig.2).

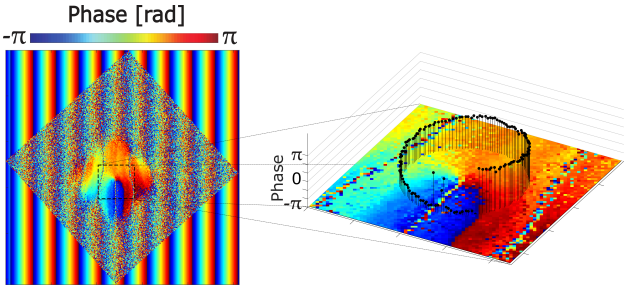

Figure 2: OV phase reconstruction. Numerical interference between the reconstructed pitchfork phase and a plain wave let the helical phase reappear. A closer look to the vicinity of the phase singularity show the phase jump of 2π.

The recovered phase shows the helical distribution with a phase jump of $\sim 2\pi$. The topological charge defined as

$$m = \pm\frac{1}{2\pi}\oint \nabla\Phi\left(\vec{r}\right) d\vec{r} \qquad (1)$$

with the phase Φ and applied to the reconstructed data results in a TC of $m = 0.98 \pm 0.15$, which states the TC to 1, since m has to be a natural number [4] and matches the initial state of the generating CHG.
The reconstruction from redundant datasets allows a full characterization of the OV within a few iterations, which could be a useful expansion to diffractogram based imaging methods.

References

[1] Bekshaev et al., "Wide-slit diffraction and wavefront diagnostics of optical-vortex beams". In: Ukrainian Journal of Physical Optics 16.1 (2015), pp. 17–23.

[2] Sacks et al. "Holographic formation of optical-vortex filaments". In: Optical Society of America 15.8 (Aug. 1998), pp. 985–990.

[3] Maiden, A.; Rodenburg, J. "An improved ptychographical phase retrieval algorithm for diffractive imaging". In: Ultramicroscopy 109.10 (Sept. 2009), pp. 1256–1262.

[4] Curtis,J.; Grier, D. "Structure of Optical Vortices". In: Physical Review Letters 90.13 (Apr. 2003).

Broadband Stimulated Raman Backscattering*

B. Landgraf[1,2], *G. Lehmann*[3], *B. Aurand*[3], *A. Hoffmann*[1], *T. Gangolf*[2,3,5], *T. Kühl*[1,3], *and C. Spielmann*[1,2]

[1]Helmholtz Institute Jena, Jena, Germany; [2]Institute of Optics and Quantum Electronics, Abbe Center of Photonics, Friedrich-Schiller University Jena, Jena, Germany; [3]Heinrich-Heine-Universität, Düsseldorf, Germany ; [4]GSI, Darmstadt, Germany; [5]École polytechnique: Université Paris-Saclay, Paris, France

Introduction

Stimulated Raman backscattering (SRBS) is a possible candidate to overcome scaling limitations in state-of-the-art chirped pulse laser amplifiers. SRBS describes a three wave interaction in laser plasmas in which a plasma wave is generated due to the ponderomotive force of a beat-wave originating from two counter-propagating and frequency shifted laser pulses. The conversion of a high-energy picosecond pump into sub-20 fs backscattered pulses offers to extend the scientific scope of petawatt laser systems towards ultra-short pulse applications while preserving their respective peak intensities.

Transient ionization

Current experiments mostly rely on ionization by a dedicated laser source. The optimal plasma distribution is found if a density gradient is present [1], resulting in higher bandwidth and conversion efficiency. Here we study SRBS with pump ionization in Neon. Pump and seed are overlapped spatially and temporally while the pump ionizes Ne up to four times in a sequential manner. A precise particle-in-cell (PIC) simulation model of pump, seed and ionization mechanic is developed and compared to experimental results.

Results

Broadband amplification of up to 80 nm could be recorded at densities of n_e/n_c = 0.002 which is also the optimal density. Analyzing the PIC simulation reveals amplification within 100 fs in which up to 1.2 % conversion efficiency is reached at 5×10^{15} W/cm^2. The average conversion efficiency over the full beam is lower at 0.6 % and 410 μJ output energy. This window is also consistent if the dispersion relation is locally solved to calculate the growth rate. Only in this timeframe sufficient growth rate and stable parameters fit together to allow SRBS before significant Landau wave-breaking and particle trapping set in. A comparison of experimental results and simulation in figure 1 shows very good agreement.

* Work supported by GSI(PHELIX)/HI Jena/HGShire/European Regional Development Fund (EFRE)/state of Thuringia (TMBWK) under Grant No. B 715-08008/TR 18

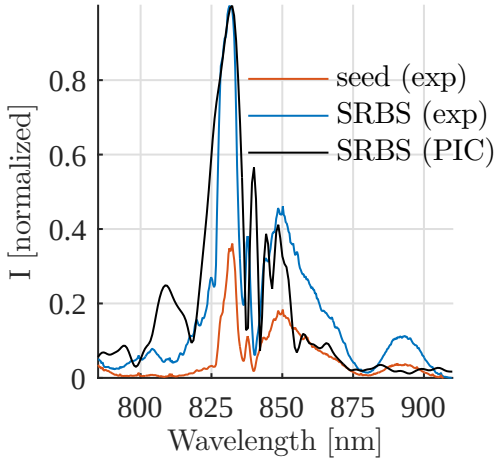

Figure 1: Comparison of PIC and experimental results as well as initial seed spectrum.

Conclusion

Amplification in the strong wave-breaking regime was measured in a transient ionization scheme. An optimal parameter region of density and intensity could be defined in which wave-breaking acts slow enough to circumvent theoretically predicted limiting mechanisms. A beneficial consequence is the growth of an ultra-short pulse whose spectral transform limit is 16.7 fs which is up to date the best published result. While the conversion efficiency is comparable to some studies in the theoretically optimal intensity regime of SRBS improvements regarding overlap length, angle and peak intensity might significantly increase it and offer important insights about the behavior of competing instabilities to SRBS in the strong wave-breaking regime.

References

[1] J. Ren, "A new method for generating ultraintense and ultrashort laser pulses", Nat. Phys. 3, 732 - 736 (2007).

[2] B. Landgraf, et al. "Broadband Stimulated Raman Backscattering", New J. Phys. 18 073048 (2016).

Generation of keV hot near solid density plasma at high contrast laser-matter-interaction

S. Zähter[1], A. Schönlein[1], O. N. Rosmej[1,2], Z. Samsonova[3,4], D. Khaghani[3], C. Arda[1], N. Andreev[5], A. Hoffmann[3], S. Höfer[3], M. Kaluza[3,4], D. Kartashov[3], L. Pugachev[5], I. Uschmann[3,4], and C. Spielmann[3,4]

[1]Goethe Universität, Frankfurt, Germany; [2]GSI, Darmstadt, Germany; [3]Friedrich-Schiller-Universität, Jena, Germany; [4]Helmholtz-Institute Jena, Germany; [5]Joint Institute for High Temperatures, Moscow, Russia

Laser accelerated electrons play a major role in the process of laser energy transfer into matter. Electron energies can usually be described by a maxwellian-like distribution function with one or more temperatures. In this work, we investigate relativistic laser-matter interaction at high laser contrast and show that a large amount of relatively "slow" keV electrons play a dominant role in the target heating process leading to the creation of a high energy density plasma state.

The experiment was carried out at the JETI-40 lasersystem delivering a high contrast (10^{-8}) frequency doubled ($400\,nm$), $45\,fs$ relativistic ($10^{19}\,W/cm^2$; $a_0 \approx 1$) laser pulse. The $180 - 200\,mJ$ laser pulse was focused to a $5\,\mu m$ spot onto the target at $45\,\mathrm{deg}$. $25\,\mu m$-thick Ti-foils have been used as targets. The diagnostic setup used in the experiment included an X-ray spectrometer with a cylindrically bent HOPG-crystal ($2d = 6.71\,\AA$) ensuring a wide spectral window of $4.4 - 7.9\,keV$ and a spectral resolution of $\lambda/\delta\lambda = 1000$. For analysis of the bremsstrahlung radiation up to $0.5\,MeV$ a hard X-ray detector (HXRD) based on a filter attenuation method and a Timepix detector operated in the single hit regime were used.

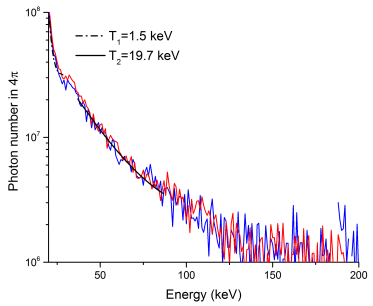

Figure 1: Bremsstrahlung radiation measured by Timepix.

Spectral distribution of the bremsstrahlung radiation of suprathermal electrons traversing the target measured using the Timepix detector is presented in Fig. 1. It can be well approximated by a two temperature electron energy distribution with $T_1 = 1.5 \pm 0.2\,keV$, $T_2 = 19.6 \pm 0.1\,keV$ and the corresponding hot electron fraction f_2 of nearly 3%.

Fig. 2 presents a Ti spectrum containing several K-shell transitions: $K\alpha$- and $K\beta$- transitions of weakly ionized Ti-atoms, K-shell transitions of intermediate charge states with vacancies in the M- and L-shell (F- up to Be-like ions) and K-shell transitions from one and double excited states in Li- and He-like Ti ions. While the intermediate charge states occur at plasma temperatures of 200–300 keV, the Li- and He-like states originate from a hot surface layer with keV temperatures. Both, a large number of low-energy electrons and a small interaction volume lead to high energy density plasmas with keV temperatures and near-solid densities. As shown in [1], the analysis of the $K\alpha$-profile broadening, that incorporates K-shell transitions of weakly ionized Ti-ions, allows to determine a plasma temperature in "warm" foil regions heated by laser accelerated electrons. In our case, this method leads to temperatures of $20 - 50\,eV$. The fit of the experimental spectrum in 2 was made using FLYCHK [2] for an optically thin plasma case with a bulk electron temperature of $T_1 = 1250\,eV$.

Diagnostics of the electron density was based on the relative intensities of the $He\alpha$ resonance and intercombination ($1s^2(^1S_0)$–$1s2p(^3P_1)$) transitions.

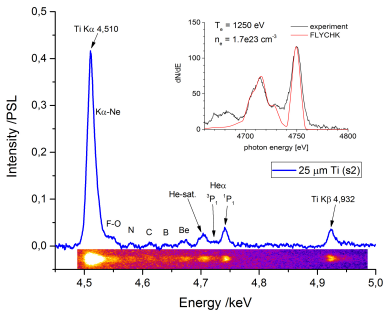

Figure 2: Measured Ti-spectrum and FLYCHK fit.

According to the fit made for the optical thin case, we obtain $n_e = 1.7 \cdot 10^{23}\,cm^{-3}$ or 15 % of the Ti solid density. Corrections for optical thickness $\tau = R/L_{ph}$ (see FLYCHK) lead to a higher bulk plasma temperature $T_1 = 1450\,eV$ and electron density $n_e = 2 \cdot 10^{23}\,cm^{-3}$.

References

[1] A. Schönlein et al, "Generation and characterization of warm dense matter isochorically heated by laser-induced relativistic electrons in a wire target", EPL, June 2016, p. 45002

[2] http://nlte.nist.gov/FLY/

X-ray emission from a laser-induced plasma with ZnO nanostructured targets

Z. Samsonova[*1,2], *S. Ališauskas*[3], *A. Baltuška*[3], *E. Förster*[1,2], *S. Höfer*[1], *D. Kartashov*[1], *V. Kaymak*[4], *S. Kroker*[5], *A. Pugžlys*[3], *A. Pukhov*[4], *C. Ronning*[6], *C. Spielmann*[1,2], *L. Trefflich*[6], *and I. Uschmann*[1,2]

[1]Institute of Optics and Quantum Electronics, Abbe Center of Photonics, FSU Jena, Germany; [2]Helmholtz Institute Jena, Germany; [3]Photonics Institute, Vienna University of Technology, Austria; [4]Institute of Theoretical Physics, Heinrich-Heine-University Düsseldorf, Germany; [5]LENA Laboratory, Technical University Braunschweig, PTB, Germany; [6]Institute of Solid State Physics, FSU Jena, Germany

Hard X-ray sources based on laser-induced plasma emission gain new interest with the advent of high energy mid-infrared laser systems. Tightly focused femtosecond laser pulses with an energy of several tens of mJ in this wavelength range can result into relativistic on-target intensities. The relatively long optical period promotes effective acceleration of the generated electrons to high kinetic energies [1]. The subsequent strong collisional ionization causes radiative transitions in the X-ray range. In our recent experiments we investigated the interaction of 3.9 μm laser pulses with nanostructured targets. The combination of such targets with a mid-IR laser source evolves into a novel regime of X-ray generation, what has been not studied yet. It is generally accepted that nanowire (NW) arrays may drastically increase the laser energy absorption [2].

With the idler beam of an OPCPA laser system (TU Vienna) is used to generate plasma from solid targets. The p-polarized laser pulses with an energy of 20-25 mJ are focused onto the samples resulting in the peak intensity of nearly 10^{17} W/cm^2. The investigated nanostructured targets, representing an array of separately standing NWs on a thick substrate, are made of ZnO (Z_{Zn}=30) and Si (Z_{Si}=14), transparent in mid IR spectral range. The main diagnostic tools in this study were bent crystal spectrometers, allowing to measure X-ray spectra in the energy ranges 1.7-2.1 keV and 8.5-9.7 keV for Si and Zn, respectively.

The electric field component oriented perpendicular to the target surface appears only at non-normal incidence of a p-polarized beam. Thereby, as it was observed, the flux from the polished samples is greatly dependent on the incidence angle. The obtained line emission is qualitatively different for investigated target materials. From the ZnO targets only K-shell emission from neutral and weakly ionized Zn is detected (Fig. 1). In turn, the nanostructured Si targets produce emission also from highly-charged ions (He_α and even Ly_α lines), which is not the case of the polished sample (Fig. 2). A huge enhancement of the K_α line is observed for the ZnO NW target in comparison with the polished one. However, under 45^0 angle of incidence this dominance is washed out. In contrast, the Si polished target can generate comparable K-shell emission from neutral atoms, but just a weak signal from Si ions at best. Our findings suggest that NWs are strongly affecting the generation of the hot line emission (He-like and H-like lines), what refers to a hotter and denser plasma, than it is produced with the polished samples. To get an insight into the plasma evolution we are currently analyzing the experimental results together with the Particle-in-Cell (PIC) simulations.

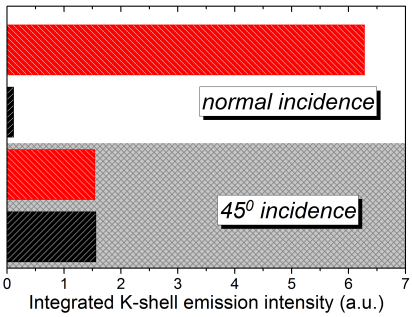

Figure 1: Integrated X-ray flux detected from the ZnO polished (black) and the nanostructured (red) targets.

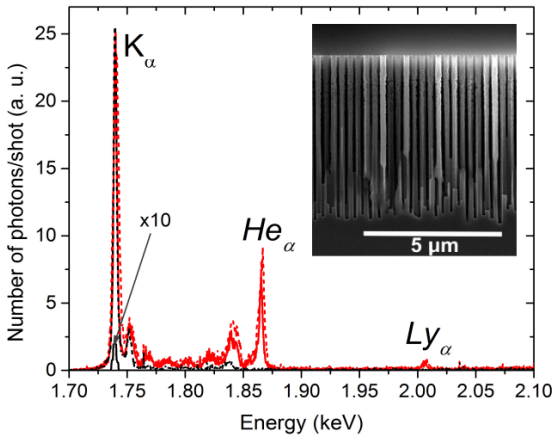

Figure 2: X-ray spectra from Si polished (black) and nanostructured (red) targets for normal (solid) and 45^0(dashed)-incidence. Inset: SEM image of the Si NW array.

References

[1] A. Purvis et al., "Relativistic plasma nanophotonics for ultrahigh energy density physics", Nature Photonics 7 (2013)

[2] J. Weisshaupt et al., "High-brightness table-top hard X-ray source driven by sub-100-femtosecond mid-infrared pulses", Nature Photonics 8 (2014)

* zhanna.samsonova@uni-jena.de

Multiphoton pumped nanowires

R. Hollinger[1,2], S. Ališauskas[3], V. Shumakova[3], L. Trefflich[4], R. Röder[4], A. Pugžlys[3], D. Kartashov[1], A. Baltuška[3], C. Ronning[4], and C. Spielmann[1,2]

[1]Institute of Optics and Quantum Electronics, Abbe Center of Photonics, FSU Jena, Germany; [2]Helmholtz Institute Jena, Germany; [3]Photonics Institute, Vienna University of Technology, Austria; [4]Institute of Solid State Physics, FSU Jena, Germany

Introduction

Zinc oxide (ZnO) nanowires provide all necessities for a laser: ZnO is a well studied gain medium, and the cylindrical geometry, together with the end facets, forms a waveguide cavity. To get laser emission the gain medium must be sufficient pumped. So far lasing from ZnO with a band gap of 3.3 eV has been mainly investigated using a single photon pump process [1]. We demonstrated lasing from single ZnO nanowires using femtosecond laser pulses, in a very broad range of wavelengths, ranging from the near (0.8 μm) to the mid-IR (3.9 μm), for pumping.

Methods

The crystalline ZnO nanowire batches were synthesized by a chemical vapor deposition (CVD) process using the vapor-liquid-solid (VLS) mechanism. Single nanowires with a length between 300-500 nm and a diameter of 10-20 μm are transferred to a SiO_2 layer using a dry imprint technique. The near-IR pumping was performed by 35 fs, 1 mJ pulses, originating from 1 kHz repetition rate Ti:Sa laser system operating at 0.8 μm wavelength. A hybrid OPA/OPCPA system, operating at 20 Hz repetition rate, provided the 90 fs, up to 30 mJ pulses centered at 3.9 μm wavelength. This pulses were focused to excite the single nanowires. A variable attenuator was used to adjust the pump power. The near ultraviolet (NUV) photoluminescence was collected with a 50x NUV microscope objective (NA = 0.4) and analysed with a spectrometer (Andor Shamrock 193i) using a back illuminated, peltier cooled CCD (Andor Newton).

Results and Discussion

Figure 1 and 2 show the measured NUV emission spectra for different pump pulse energies, when the wires are pumped with 0.8 μm near-IR and 3.9 μm mid-IR pulses, respectively. The insets depict the integrated emission vs.pump pulse energy. The spectra show for pump pulses in the near as well as mid-IR the characteristic Fabry-Perot-modes when the laser threshold is reached. This transition from spontaneous to stimulated emission is identified by a rapid change in the slope of the integrated emission. The experimental data show, that ZnO nanowires can be pumped sufficient in a wide range of wavelengths to enable laser emission. While a three photon absorption process enables the excitation of an electron in the case of 0.8 μm near-IR pulses, tunnel ionization is dominating if 3.9 μm mid-IR pulses are used [2]. To our knowledge, this is the first experimental proof of observing stimulated emission under pumping via tunneling excitation.

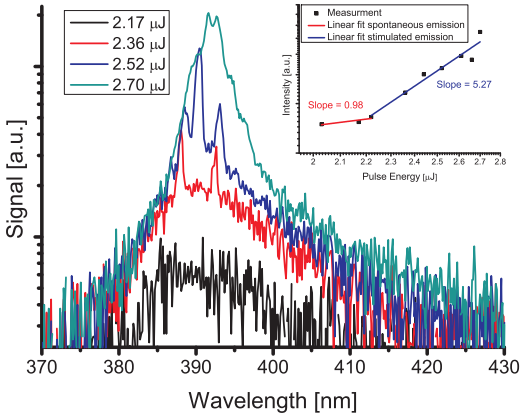

Figure 1: Emission spectra of a near-infrared (0.8 μm) pumped single nanowire. The inset show the emitted signal vs. pump energy.

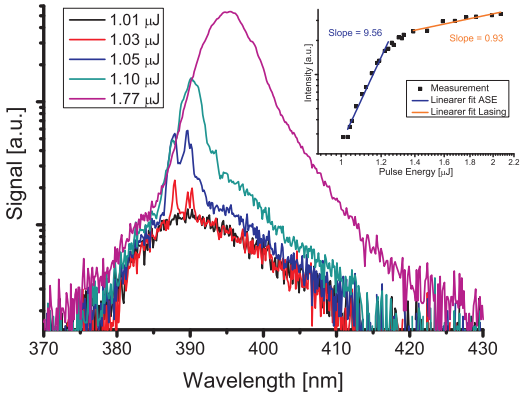

Figure 2: Emission spectra of a mid-infrared (3.9 μm) laser pumped single nanowire. The inset show the emitted signal vs. pump energy.

References

[1] M. A. Zimmler, F. Capasso, S. Müller and C. Ronning, "Optically pumped nanowire lasers: invited review", Semiconductor Science and Technology, 25(2):024001 (2010)

[2] L. V. Keldash, "Ionization in the field of a strong electromagnetic wave", Soviet Physics JETP, 20:1307–1314 (1965)

Forschergruppe: XUV technology and methods for imaging with nanoscale resolution

S. Fuchs[*1,2], *G. G. Paulus*[1,2], *F. Tuitje*[1,2], *M. Zürch*[2], *C. Spielmann*[1,2], *M. Tschernajew*[1,2], *J. Rothhardt*[1,2], *J. Limpert*[1,2], *M. O. Herdrich*[1], *G. Weber*[1], *and T. Stöhlker*[1,2]

[1]Helmholtz Institute, Jena, Germany; [2]Friedrich Schiller University, Jena, Germany

Imaging in the extreme ultraviolet regime has decisive advantages. It can provide nanometer resolution and a unique material contrast. However, the technological realization of lab-scale XUV microscopes is extremely demanding. One of the main challenges is the transition from large-scale synchrotron light sources towards small footprint laser sources. Therefore, laser radiation needs to be converted into the XUV and imaging techniques, which are common at a synchrotron, need to be adapted to the new sources. At the Helmholtz Institute Jena a new research collaboration ("Forschergruppe"), funded by the Thüringer Aufbaubank (TAB), has been founded to combine various expertise in different fields of XUV technology inside the Institute.

High-flux HHG sources have been developed during the last years. In the photon energy range below 100eV they can reach photon fluxes, which are comparable to synchrotron sources [1]. To this end, high average-power fiber laser system with very high repetition rates are tightly focused to reach the intensity which is necessary to produce high harmonics.

The generated radiation exhibits laser-like properties and its coherence is, once monochromatized, perfectly suited for coherent lensless imaging approaches like coherent diffraction imaging (CDI) and ptychography. The HI Jena successfully used laser-based sources to demonstrate these methods on the lab-scale [2] and reached nanometer lateral resolution.

However, since the high harmonics intrinsically have a very broad bandwidth, most of the XUV photons are lost by the monochromatization. Therefore, a novel broadband three-dimensional imaging technique called XUV coherence tomography (XCT) has been developed. The method utilizes the spectrally broad photon flux to reach nanometer axial resolution [3].

Even for CDI monochromatization could in fact be avoided if a pixelated detector with energy resolution in every pixel would be used. The HI Jena has experience in using such detectors in the hard x-ray regime. Pixelated micro-calorimeters are used to measure the heat input of single photons and thus the photon energy [4]. Such detectors with a sufficient pixel number and energy resolution in the XUV regime have the potential to be a game changer in XUV imaging.

The main goal of the "Forschergruppe" is to combine all of these approaches and thus to develop entirely new methods which are specially designed to fit the needs of a HHG source. The sturcture of the group is depicted in Fig. 1. The sources will be optimized even further to deliver sufficient photon flux to drive CDI and XCT. First experiments show that CDI with its nanometer lateral resolution and XCT with nanometer axial resolution can in fact be combined to record three-dimensional images with nanoscale resolution in every dimension in reflection geometry without cutting or destroying the sample. The combination of both techniques requires the recording of spectrally resolved diffraction patterns. This can be done via a swept source approach, i.e. scanning a monochromator, which is time consuming or with the new energy resolved detectors, which can record all wavelengths at once.

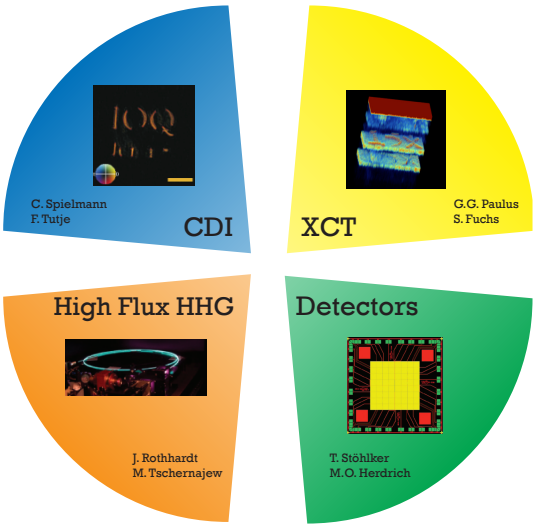

Figure 1: Structure and contributions of the four groups inside the "Forschergruppe"

References

[1] Hädrich, S. *et al.*, "High photon flux table-top coherent extreme-ultraviolet source", Nat. Photonics 8, 779-783 (2014).

[2] Zürch, M. *et al.*, "Real-time and Sub-wavelength Ultrafast Coherent Diffraction Imaging in the Extreme Ultraviolet", Scientific Reports 4, 7356 (2014).

[3] Fuchs, S. *et al.* , "Nanometer resolution optical coherence tomography using broad bandwidth XUV and soft x-ray radiation", Scientific Reports 6, 20658 (2016).

[4] Hengstler D. *et al.*, "Metallic magnetic calorimeters for high-resolution x-ray spectroscopy", Phys. Scr. T166 (2015).

* silvio.fuchs@uni-jena.de

High resolution nanoscale XUV imaging on a table-top*†

G. Tadesse[1,2], *W. Eschen*[1,2], *R. Klas*[1,2], *M. Zürch*[1,3,4], *C. Spielmann*[1,3], *A. Tünnermann*[1,2,5], *J. Limpert*[1,2,5], *and J. Rothhardt*‡ [1,2]

[1]Helmholtz Institute Jena, Jena, Germany; [2]Friedrich-Schiller-University, Institute of Applied Physics, Jena, Germany; [3]Friedrich-Schiller-University, Institute of Optics and Quantum Electronics, Jena, Germany; [4]Department of Chemistry, University of California, Berkeley, California 94720, USA; [5]Fraunhofer IOF, Jena, Germany

Coherent diffractive imaging is a well-established technique at synchrotron and free-electron-laser light sources which allows imaging of small objects with only a few-nanometers resolution. Since only the diffraction pattern is detected and the object exit wave is reconstructed by iterative computer algorithms, no imaging optics are required. Hence, the resolution is solely determined by the wavelength and the maximum scattering angle which can be detected with sufficient signal-to-noise ratio. We developed a table-top implementation of this technique by utilizing high harmonics generated by focusing an infrared femtosecond fiber laser into an argon gas jet (see Fig. 1.)[1,2]. The generated XUV radiation (18 nm wavelength) is separated from the fundamental infrared light and re-focused onto the sample by using two concave multilayer mirrors. A typical diffraction pattern of a test structure, recorded by an XUV-CCD, is shown in Fig. 2(a).

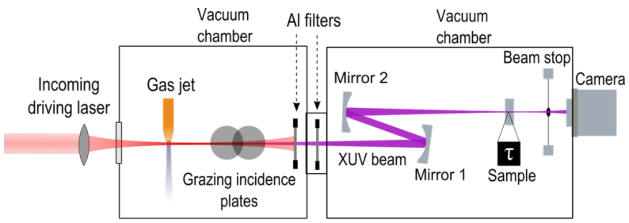

Figure 1: Experimental setup of the table-top XUV Nanoscope. XUV light is generated by focusing femtosecond pulses from an infrared fiber laser into an argon gas jet. It is then refocused onto the sample and a CCD-Camera records the diffraction pattern behind the sample.

Due to the record high photon flux of our table-top XUV source [1], as well as the excellent beam quality and spatial coherence, the diffraction pattern (Fig. 2(a)) has been detected with a numerical aperture as high as 0.7. Fig. 2(b) and (c) display the reconstructed amplitude and phase of the light wave exiting the employed sample. The achieved spatial resolution is better than 15 nm (Abbe-limit: 12 nm) and represents a new record for table-top XUV and X-ray microscopes. Moreover, a single 3 s acquisition is sufficient to achieve 25 nm resolution, which will allow scanning on extended samples and 3D tomography on the nanoscale in the near future. Further advances in femtosecond fiber laser technology and high harmonic generation will ultimately enable few-nanometer resolution imaging of 3D nanostructures e.g. modern nano-optical and nano-electronic devices.

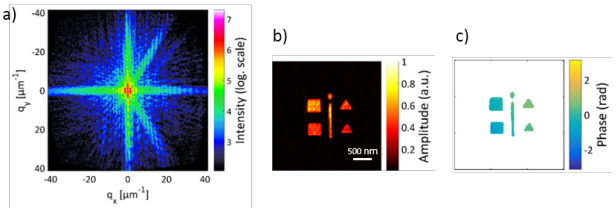

Figure 2: (a) Measured diffraction pattern, (b) Reconstructed amplitude, (c) reconstructed phase. The achieved resolution is 13 nm

References

[1] J. Rothhardt, S. Hädrich, Y. Shamir, M. Tschnernajew, R. Klas, A. Hoffmann, G. K. Tadesse, A. Klenke, T. Gottschall, T. Eidam, J. Limpert, A. Tünnermann, R. Boll, C. Bomme, H. Dachraoui, B. Erk, M. Di Fraia, D. A. Horke, T. Kierspel, T. Mullins, A. Przystawik, E. Savelyev, J. Wiese, T. Laarmann, J. Küpper, and D. Rolles, "High-repetition-rate and high-photon-flux 70 eV high-harmonic source for coincidence ion imaging of gas-phase molecules," Opt. Express 24, 18133–18147 (2016).

[2] S. Hädrich, J. Rothhardt, M. Krebs, S. Demmler, A. Klenke, A. Tünnermann, and J. Limpert, "Single-pass high harmonic generation at high repetition rate and photon flux," J . Phys. B. 49, 1 (2016).

[3] G. K. Tadesse, R. Klas, S. Demmler, S. Hädrich, I. Wahyutama, M. Steinert, C. Spielmann, M. Zürch, T. Pertsch, A. Tünnermann, J. Limpert, and J. Rothhardt, "High Speed and High Resolution Table-Top Nanoscale Imaging," Opt. Lett. 41, 5170-5173 (2016).

* Work supported by the Thüringer Aufbaubank.

† This article is also part of the annual report of the Institute of Applied Physics.

‡ j.rothhardt@gsi.de

High Harmonic Generation in the Water Window with a 2 µm Fiber Laser

R. Klas[1,2], S. Demmler[1], M. Tschernajew[1,2], M. Gebhardt[1,2], C. Gaida[2], F. Sutzki[2], A. Kirsche[1], A. Tünnermann[1,2,3], J. Rothhardt[1,2] and J. Limpert[#1,2,3]

[1]Helmholtz-Institute Jena, Fröbelstieg 3, 07743 Jena, Germany;

[2]Institute of Applied Physics, Abbe Center of Photonics, Friedrich-Schiller-Universität Jena, Albert-Einstein-Str. 15, 07745 Jena, Germany;

[3]Fraunhofer Institute for Applied Optics and Precision Engineering, Albert-Einstein-Str. 7, 07745 Jena, Germany

Nanoscale imaging in the XUV and X-ray spectral region allows exceptionally high resolution without additional markers or super-resolution techniques [1]. Especially the spectral region of the water window spanning from 284 eV to 543 eV is of great interest, because water is rather transparent but the K-edges of the biological building blocks like carbon (284 eV), nitrogen (410 eV), and oxygen (543 eV) provide good contrast for imaging. Moreover, near edge X-ray absorption fine structure (NEXAFS) spectroscopy can be combined with imaging to gain additional information on the chemical composition and coordination of the constituents. Applicability in many fields of science and technology, however, desires table-top implementations of these techniques. Therefore, there is a great demand for a high photon flux coherent water-window light sources.

High harmonic generation (HHG) is an attractive method to enable such sources. Due to the favorable λ^2 scaling of the cutoff energy long driving wavelength are beneficial for generating high photon energies.

Recent approaches used TiSa seeded OPA schemes to generate harmonics in the water window [3],[4]. However, the ~ 2.0 µm wavelength drivers are so-far limited to a few kHz of repetition rate and a few Watts of average powers, due to thermo-optical constraints and limited pump-power.

Fiber lasers on the other hand offer a high repetition rate up to the MHz regime and high average power up to 1 kW. Yb-based femtosecond fiber lasers emitting at ~1 µm wavelength, have shown to be suitable driver for high photon flux sources in the extreme ultraviolet (XUV) wavelength region [5],[6].

We now directly used a Tm doped fiber chirped pulse amplifier (FCPA), delivering a central wavelength of 1950 mm, and demonstrated water window HHG with such a system, for the first time.

The driving laser system delivers 100 fs pulses with 6.7 W of average power at 10 kHz of repetition rate, resulting in 670 µJ of pulse energy. Afterwards these pulses are strongly focussed into a neon gas jet, using a f=50 mm lens. This yields a focal spot size of 60 µm, resulting in a peak intensity of $1.1 \cdot 10^{14}$ W/cm^2. Afterwards the collinearly propagating XUV radiation and the infrared driving laser have been separated by a 200 nm thick silver filter and is then analysed by a flat field spectrometer (Fig. 1). To achieve fully phase matched and absorption limited HHG, a gas nozzle with a diameter of 500 µm and a backing pressure of 15 bar had to be used.

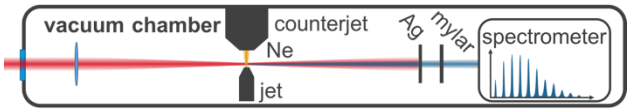

Figure 1: Schematic sketch of the experimental setup.

However, the high gas load of such a nozzle alone would result in a too high ambient pressure in the vacuum chamber and re-absorption of the generated XUV light. Therefore, a second nozzle opposite to the jet was used to collect the largest amount of the gas. This reduces the ambient pressure in the chamber by more than one order of magnitude and therefore minimizes re-absorption.

The measured HHG spectra are shown in Fig. 2. These spectra show a photon flux of ~10^4 photons/s/eV in the water window. A 200 nm thick mylar filter with a K-absorption edge at 284 eV was used for energy calibration and signal verification. A maximum photon energy of ~310 eV has been detected. Numerical simulations indicate phase-matched generation of these water-window harmonics.

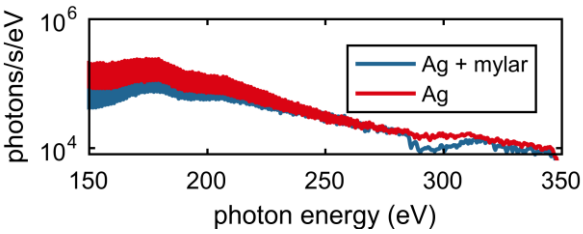

Figure 2: Measured spectra with and without mylar.

This is the first demonstration of HHG, driven directly by Tm-doped FCPA. Further developments in laser architecture will lead to intense few-cycle pulses at average powers of up to 100 W which will allow to increase the reported photon flux by more than 2 orders of magnitude.

Such a high photon flux source will foster many applications including imaging and spectroscopy of organic- and biological samples.

References

[1] G. K. Tadesse et al., Opt. Lett. 41, 5170 (2016).
[2] M.V. Frolov et al., PRL 100, 173001 (2008).
[3] S.L. Cousin et al., Opt. Lett. 39, 5383 (2014).
[4] T. Popmintchev et al., Science 336, 1287 (2012).
[5] Klas et al., Optica 3(11), 1167 (2016).
[6] S. Hädrich et al., J. Phys. B: At. Mol. Opt. Phys. 49, 172002 (2016).

[#]jens.limpert@uni-jena.de

Design of an online data analysis algorithm for cryogenic microcalorimeters*

M. O. Herdrich[1,2,3], *G. Weber*[1,2], *A. Fleischmann*[4], *D. Hengstler*[4], *and Th. Stöhlker*[1,2,3]
[1]HI Jena; [2]IOQ, FSU Jena; [3]GSI, Darmstadt; [4]KIP, RKU Heidelberg

Introduction Recent developments in the field of cryogenic microcalorimeters have made metallic magnetic calorimeters - like the maXs-detectors - a particularly promising tool for x-ray spectroscopy experiments as they are proposed within the frame of the SPARC collaboration [1]. The measurement of particle energies employing the temperature sensitivity of the magnetization of the sensor requires very low temperatures (< 15 mK) [2]. Because of the low excitation energy of phonons, microcalorimeters have an intrinsically high energy resolutions ($\mathrm{E}/\Delta\mathrm{E}_{\mathrm{FWHM}} \approx 3000$) [3]. At the same time, the noise level is almost independent of the particle energy making the detector operable in a broad energy range ($\approx 0.1 - 100$ keV). Although, the currently used optimal filtering technique for event analysis extracts particle energies with almost negligable uncertainties, it so far is only applicable to offline data, therefore in some cases producing unfeasable amounts of data [4]. Furthermore the filter is very sensitive to jittering of operation parameters and does not allow pile-up correction, thus reducing the acceptable event rate enormously. This is why for multipixel detectors with even higher data rates new algorithms and read out mechanisms need to be designed.

Requirements Several requirements for the analysis procedure arise from both structure and amount of data produced by microcalorimeters. After absorbing a particle the microcalorimeter has to thermalize with the connected cold bath creating a long falling edge in the signal (> 10 ms). High event rates therefore inevitably lead to pile-up of events that has to be detected and handled. The fast rising edge ($< 1\mu$s) on the other hand determines a high sampling rate. To adequately handle the amount of data that needs to be processed (≈ 30 kSamples / event) the analysis must be performed online by a FPGA running a continuous signal analyzer. In addition to these performance requirements the system also needs to be more robust in regards of timing and baseline jittering.

State of the project A first concept for the data analysis for FPGA deployment has been designed. The processing pipeline consists of several finite response filters (see fig. 1) that deconvolute (*Moving Window Deconvolution* - MWD) and average the signal (*Moving Average Filter* - MAF). In combination with a triggering system the particle energy can be extracted from the filtered data for each individual event. So far, several tests have been performed on both simulated and measured data sets taken from experiments with elementary gamma sources as well as x-rays stemming from collision studies performed at the ESR of GSI to examine the behavior of the algorithm. First results indicate that the algorithm has a performance close to that of the optimal filtering ($\mathrm{E}/\Delta\mathrm{E}_{\mathrm{FWHM}} \approx 2700$).

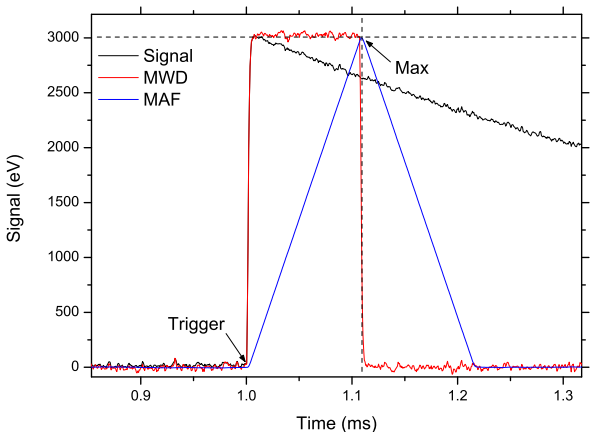

Figure 1: A typical detector signal (starting at 1 ms) as well as both filter outputs. The rectangular signal is produced by the deconvolution (MWD) and averaged into the triangular shape (MAF). The signal height decoding the particle energy can be read out directly as maximum value of the filter.

Conclusion As expected, the optimal filter yields results with better energy resolution, however the new system is more stable and prepared for large amounts of data as well as fast event rates. More tests on different parameters still need to be performed, in particular, edge cases have to be reviewed. Summarizing, first steps towards a more flexible data analysis procedure have been taken successfully. Especially, projects like ECHo (The Electron Capture ^{163}Ho Experiment) [5] as well as experiments at the CRYRING@ESR of the FAIR project could profit from such a system in the near future.

References

[1] D. Hengstler et al., Phys. Scr. T166, 2015
[2] C. Enss et al., J. Low Temp. Phys., Vol. 121, 2000
[3] S. Kempf et al., Supercond. Sci. Technol., Vol. 28, 2015
[4] A. Fleischmann et al., IEEE Trans. Appl. Supercond., Vol. 19, 2009
[5] L. Gastaldo et al., J. Low Temp. Phys., Vol. 176, 2014

*This work is supported by the European Union and the federal state of Thuringia via Thüringer Aufbaubank withing the ESF project (2015 FGR 0094). This report is also part of the GSI Scientific Report 2016 / GSI Report 2017-1.

Online monitoring of XUV spectra from high-harmonic generation by surface reflectivity measurements with particle detectors*

A. Hoffmann[†1], *C. Egelkamp*[2], *D.F.A. Winters*[3], *T.Kühl*[3,4], *and C. Spielmann*[1,4]

[1]Institute of Optics and Quantum Electronics, Abbe Center of Photonics, Friedrich Schiller University Jena, Max-Wien-Platz 1, 07743 Jena, Germany; [2]Institut für Kernphysik, Westfälische Wilhelms Universität, Wilhelm-Klemm-Straße 9, 48149 Münster, Germany; [3]GSI Helmholtz Centre for Heavy Ion Research, Planckstrasse 1, 64291 Darmstadt, Germany; [4]Helmholtz Institute Jena, Fröbelstieg 3, 07743 Jena, Germany

We present reflection measurements of cesium iodide (CsI)-coated and uncoated steel surfaces with shaped XUV pulses. We measure the spectrally integrated signal from both surfaces and show that the ratio of the two measured signals is a sensitive probe of changes in the incident XUV spectrum. Additionally, a disagreement between the measured ratio and the calculated number can be explained by a leakage of IR radiation through one of the metal filters. This simple setup allows for the monitoring of the IR leakage and spectral stability simultaneously. The benefits of our approach are a spectrally sensitive diagnosis of the XUV radiation at the interaction place of time-resolved XUV experiments and the detection of infrared leak light though metal filters in high-harmonic generation (HHG) experiments. Our obtained results are of interest for time-resolved XUV experiments presenting an additional diagnostic directly in the interaction region and for small footprint XUV beamline diagnostics.

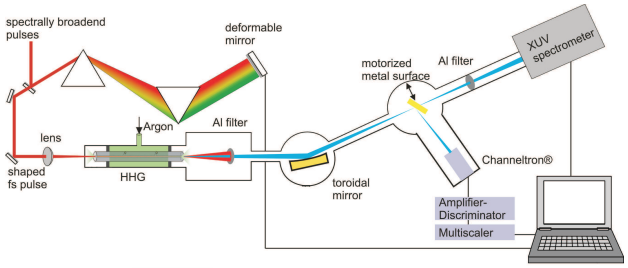

Figure 1: Experimental setup

For the experiments we used spectrally shaped XUV pulses from high-harmonic generation in an argon-filled capillary (Fig. 1, detailed experimental description in [1] and [2]). The XUV radiation is either directly launched into an XUV spectrometer or detcted with a Channeltron after reflection from an uncoated or CsI-coated stainless steel plate. The polished surfaces were coated by a vacuum evaporation process with a 300-nm-thick layer of high purity CsI [3]. The secondary electron signal from the Channeltron is amplified, discriminated and measured by a multiscaler with sub-nanosecond resolution. From the XUV spectra (Fig. 2a) the reflectivity ratio between the two surfaces can be calculated using tabulated values [4]. A comparison with reflection measurements using a Channeltron shows agreement with less then 3% difference to the calculation (Fig. 2b), but in case of residual IR light a stronger deviation is visible (∼10%).

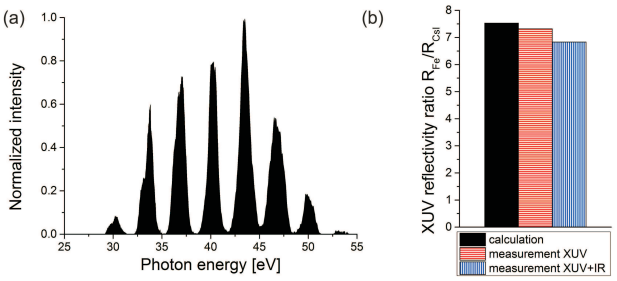

Figure 2: For an XUV spectrum (a) the reflectivity ratio between an uncoated stainless surface and a CsI-coated surface (b) can be calculated from tabulated values (black) or measured. Depending on the residual IR content in the XUV emission from HHG, a deviation from the calculation can be observed (red horizontally dashed, blue vertically dashed).

Further investigations with high-harmonics with residual IR light showed, that the Channeltron signal is sensitive to femtosecond laser light in an XUV-beam, although the Channeltron is regarded as solar blind. In the temporally resolved secondary electron signal from the Channeltron the interaction with femtosecond IR pulses can be clearly attributed to certain time windows [1].

References

[1] A. Hoffmann et al.: Online Monitoring of Laser-Generated XUV Radiation Spectra by Surface Reflectivity Measurements with Particle Detectors, Appl. Sci. 2017, 7, 70.

[2] A. Hoffmann et al.: Extremely Nonlinear Optics Using Shaped Pulses Spectrally Broadened in an Argon- or Sulfur Hexafluoride-Filled Hollow-Core Fiber, Appl. Sci. 2015, 5, 1310-1322.

[3] C. Egelkamp et al.: Detection system for forward emitted XUV photons from relativistic ion beams at ESR, GSI Scientific Report 2015 (2016)

[4] B.L. Henke et al.: X-ray interactions: photoabsorption, scattering, transmission, and reflection at E=50-30000 eV, Z=1-92, Atomic Data and Nuclear Data Tables Vol. 54 (no.2), 1993, 181-342

* Work supported by BMBF under contract numbers 05P15PMFAA and 05P15SJFFA.

† andreas.hoffmann.3@uni-jena.de

APPA R&D — BMBF collaborative research at FAIR*

S. Schippers† [1] *and Th. Stöhlker*[2,3]

[1]I. Physikalisches Institut, Justus-Liebig-Universität Gießen, 35392 Giessen, Germany; [2]Helmholtz-Institut Jena, 07743 Jena, Germany; [3]GSI Helmholtzzentrum für Schwerionenforschung, 64291 Darmstadt, Germany

The research collaboration APPA R&D [1] comprises the German university groups who have set out to perform scientific research at the future international accelerator complex FAIR (Facility for Antiproton and Ion Research) under the umbrella of APPA (Atomic, Plasma Physics and Applications). The FAIR-installations (Fig. 1) are currently under construction at the site of the GSI Helmholtz Center for Heavy Ion Research in Darmstadt, Germany. APPA is one of the four research pillars of FAIR hosting the international research collaborations BIOMAT (biophysics and material research), FLAIR (physics with low-energy antiprotons), HEDgeHOB/WDM (plasma physics), and SPARC (atomic physics) who focus on investigations of matter under extreme conditions such as strong fields, high densities, high pressures, and high temperatures [2].

The APPA R&D research collaboration pursues coordinated research projects in the area of accelerator based experiments with heavy ions at the future FAIR-installation. Central issues are i) further development of the the experimental infrastructure, in particular, research and development for enhancing the scientific capabilities of the existing installations and of the future accelerator and detector systems including the respective base technologies, and ii) set-up of the APPA experiments of the modules 0-3 of the modularized start version of FAIR.

FAIR is expected to operate fully in 2024/2025. However, the existing GSI accelerators including the existing Experimental Storage Ring (ESR) are available already now as well as the low-energy storage ring CRYRING, a Swedish in-kind contribution to FAIR, which is currently being commissioned. CRYING will receive cooled and decelerated highly charged ions from ESR, thus, permitting, e.g., precision experiments that will challenge state-of-the-art calculations within the frame-work of quantum electrodynamics (QED). In addition to ESR, a separate injector can also provide ions to CRYRING, such that it can be operated and used for experiments even when ESR is serving other purposes. First user experiments will start in 2018. From then on, a rich and diverse experimental program covering topics from atomic physics, nuclear physics, material sciences, and accelerator physics will be pursued [3].

APPA R&D is funded by the German Federal Ministry for Education and Research (BMBF) within the collaborative-research frame work (‘Verbundforschung’).

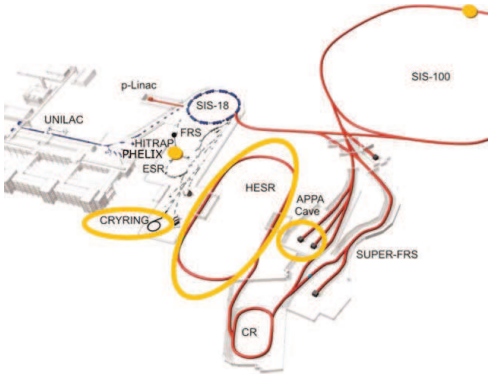

Figure 1: Experimental facilities at the Modularized Start Version (MSV) of FAIR [2]. The existing ion-beam lines and the new FAIR facilities are marked in blue and red, respectively. Sites where major APPA activities will take place are marked in yellow. Experiments in the low-energy storage ring CRYRING [3] will start in 2018. According to the current planning, FAIR will fully operate in 2024/2025.

References

[1] http://appa-rd.fair-center.eu

[2] Th. Stöhlker *et al.* 2015 *Nucl. Instrum. Meth. B* **385** 680 http://dx.doi.org/10.1016/j.nimb.2015.07.077

[3] M. Lestinsky *et al.* 2016 *Eur. Phys. J ST* **225** 797 http://dx.doi.org/10.1140/epjst/e2016-02643-6
[1]

* for the APPA collaborations

† stefan.schippers@physik.uni-giessen.de

[1]Also part of the GSI Scientific Report 2016 / GSI Report 2017-1

Development of a high-resolution x-ray spectrometer for laser-generated hot dense plasma emission *

D. Khaghani[†1], *B. Borm*[2,3], *P. Neumayer*[3], *and C. Spielmann*[1,4]

[1]Friedrich-Schiller-University, Jena, Germany; [2]Goethe-University, Frankfurt, Germany; [3]GSI, Darmstadt, Germany; [4]HI Jena, Jena, Germany

In last year's *GSI Scientific report* we reported on the generation of ultra-high energy density conditions irradiating tailored micro-pillar arrays at high laser-drive energy [1]. We carried on further experiments to better characterize these extreme plasma conditions. A high-resolution x-ray spectrometer was developed so as to measure the variety of K-shell emission lines providing accurate information about the time evolution of both temperature and density. We report here on the technical design of that instrument.

In our experiments, the target material chosen for spectroscopy purposes is copper. For this element, the K-shell transition lines of interest are emitted between 8000 and 9000 eV, ranging from quasi-neutral species' K_α ($\sim$ 8040 eV) to highly-ionized ion emission (8370 and 8680 eV for He_α and Ly_α, respectively). Furthermore, many intermediate lines from various charge states and so-called dielectronic configurations can provide accurate estimates for the plasma parameters. In order to differentiate these spectrally-close lines, we need high quality crystals which are able to perform high-resolution diffraction. α-Quartz silicon dioxide (SiO_2) crystals are commonly used for this application [2] and are widely characterized [3]. These quartz crystals are available with various lattice cuts, which has to be chosen in accordance with the corresponding Bragg angle. The ideal choice for the spectral window of interest is the lattice $22\bar{4}3$ with a $2d$-spacing of 2.024 Å. Finally, increasing the signal-to-noise ratio is made possible with spherically curved crystals which focus the spectrum into a thin line.

A commercial crystal (Golem IMS GmbH) is used. It consists of a 12×48 mm^2 quartz crystal ($22\bar{4}3$) applied onto a concave spherical glass substrate with a radius of curvature of 150 mm. We designed a holder to position the crystal onto the spectrometer board (Fig. 1). The crystal is mounted on a kinematic platform (Thorlabs KM100B/M) equipped with two tip-tilt adjusters for fine alignment of the crystal pointing. The platform is attached to an assembly of two translation stages (OptoSigma TSDH-251S and TSDS-253): one along the x-axis parallel to the spectrometer board in the crystal focus direction and another one along the z-axis for crystal height adjustment. The spectrometer board is a 10 mm-thick Delrin plate which extends in the direction of the central axis of the crystal so as to mark the position of two alignment reference points with the help of pointy metal dowel pins. These two reference points are: (**1**) the center of the Rowland circle (focus of the crystal at 0°), and (**2**) the center of curvature. They are located at 75 and 150 mm from the center of the crystal surface, respectively. Finally, the spectrometer board is mounted onto a rotation stage (Newport M-UTR80SA) whose rotation axis passes through the center of the crystal surface in order to maintain the crystal in the right position while adjusting the Bragg angle by turning the plate. The detector, an imaging plate (Fujifilm BAS-SR), is place in an enclosed aluminium box. An alignment hole (**3**) is located on the side of the box so that a laser diode shining through it would span the surface of the detector across its long side, thus symbolizing the detector axis. This method is used to finely tune the focus of the spectrum as the geometrical configuration requires that the radiation source and the center of curvature of the crystal are placed on the detector axis.

In the framework of the BMBF project "Development of x-ray spectroscopy for 'Day One' plasma physics experiments at FAIR", we will delve into further designing of similar spectrometers.

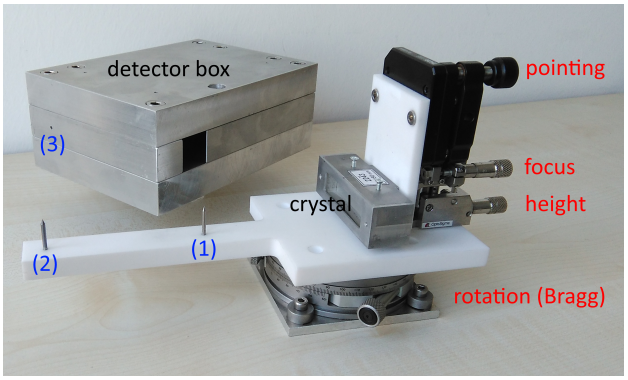

Figure 1: Photograph of the spectrometer describing its alignment features: reference points (blue) and optomechanics (red)

References

[1] D. Khaghani *et al.*, "Proton acceleration and matter at ...", GSI Scientific Report 2015 (2016) 179

[2] F.P. Condamine *et al.*, "M-shell resolved high-resolu- ...", AIP Conf. Proceedings (2017) Vol. 1811 No. 1 p. 060001

[3] L. Antonelli *et al.*, "Measurement of reflectivity of spher- ...", Review of Scientific Instruments (2015) 86(7) 073507

* This work will also be published in *GSI Scientific Report 2016*

† d.khaghani@gsi.de

First test of an improved Si(Li) Compton polarimeter for SPARC*

M. Vockert[†1,2], *G. Weber*[1], *U. Spillmann*[3], *T. Krings*[4], *Th. Stöhlker*[1,2,3], *and the SPARC collaboration*

[1]HI Jena, Germany; [2]FSU Jena, Germany; [3]GSI, Darmstadt, Germany; [4]FZ Jülich, Germany

The study of particle and photon polarization phenomena occurring in the interaction of fast ion and electron beams with matter is of great relevance for the understanding of cosmic and laboratory plasmas where high temperatures, high atomic charge-states and high field strengths prevail. In particular, the field of hard x-ray polarimetry has profited significantly from the recent development of novel highly segmented semiconductor detectors applied as Compton polarimeters, see [1] and references therein.

To strengthen the instrumentation portfolio in line with the scientific program of the SPARC pillar of FAIR a new Si(Li) Compton polarimeter was build and recently commissioned in a test experiment at the ESR storage ring at the GSI accelerator facility.

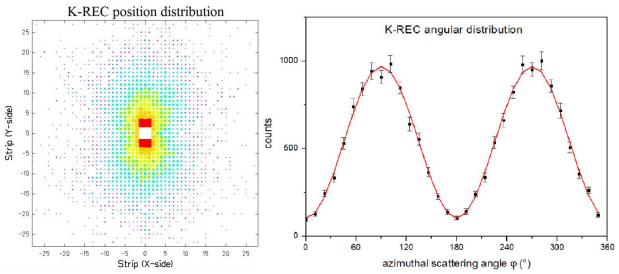

Figure 1: Left: Position distribution of the scattered Compton photons with respect to the point where the scattering took place for the K-REC peak. Right: Azimuthal scattering distribution of the same pattern, and fit based on the Klein-Nishina equation (red)

The performance of the detector as a Compton polarimeter was studied using the radiative electron capture (REC) stemming from the collision of a beam of bare xenon ions at an energy of 31 MeV/u with a hydrogen gastarget. Interestingly, the emitted radiation of the capture into the K-shell of the xenon ion is expected to be almost fully linearly polarized, as already pointed out by S. Hess et al. [2]. For the present experimental conditions the K-REC line has an energy of 60 keV, which is below the working range of previous Compton polarimeters, but was now accessible due to the improved energy resolution of the new detector.

The observed position distribution of the incident K-REC photons undergoing Compton scattering inside the detector crystal is presented in Figure 1. The strong anisotropy indicates, according to the Klein-Nishina equation [3], a high degree of linear polarization and therefore fits well with the expectation.

* Work supported by BMBF Verbundprojekt 05P2015 R&D Beschleuniger/HI Jena/GSI(ESR, SIS, UNILAC). This report is also part of the GSI Scientific Report 2016 / GSI Report 2017-1.

† Marco.Vockert@uni-jena.de

The statistical significance of the experimental data is quite good, but as the data analysis relies on modelling of the detector response and the emission pattern of the Compton process, it is important to get systematics under control. To check at which number of events the statistical uncertainty is decreasing below systematic uncertainties due to an unperfect match of the detector response function and our Klein-Nishina-based model of the emission pattern, multiple Monte Carlo simulations of the whole setup were performed.

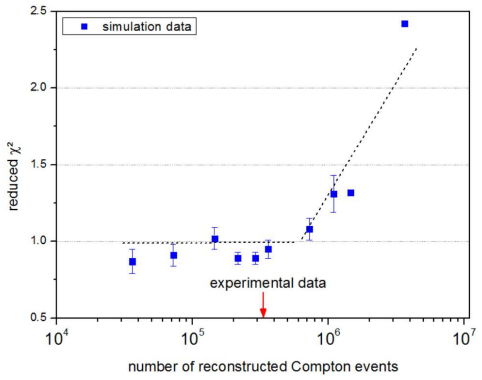

Figure 2: Deviation of the fitting model from the detector response function, indicated by the reduced χ^2 value as a function of the number of reconstructed Compton events. The number of events in the experimental data is indicated by the red arrow.

The simulations contained different amounts of statistical significance to locate the critical point where the systematical errors begin to take effect and to compare it with the experimental data. For each data point several comparable simulations were averaged to minimize random effects. The values for the reduced χ^2 of the data sets serve as an indicator of the deviation of the fitting model from the detector response function, and is shown in Figure 2. As can be seen, for up to about one million reconstructed Compton events the value of the reduced χ^2 is in the range of 1 (first part of the dashed line) and therefore the use of this fitting model is reasonable, which is also true for our experimental data point. For a higher number of events the value is increasing rapidly (second part of the dashed line) and therefore systematic effects should be taken into account.

References

[1] G. Weber et al., J. Phys.: Conf. Ser. 583, 012041 (2015)

[2] S. Hess et al., J. Phys.: Conf. Ser. 194, 012025 (2009)

[3] O. Klein, Y. Nishina, Z. Physik 52, 853 (1929)

Status report on a Si(Li)-Compton polarimeter of SPARC - 3D-readout of a thick double-sided Si(Li) strip detector*

U. Spillmann[1], Th. Krings[4], M. Vockert[2,3], G. Weber[2,], and Th. Stöhlker[1,2,3], on behalf of the SPARC collaboration

[1]GSI, Darmstadt, Germany;[2]HI Jena, Germany;[3]IOQ, FSU Jena, Germany; [4]IKP, FZ Jülich, Germany

The x-ray polarization and spectroscopy research program of the SPARC collaboration [1] at FAIR and GSI depends strongly on the performance of the available Compton polarimeter instruments within the community. During the last years we applied the our Si(Li)- and Ge(i)-Compton polarimeters in several accelerator-based beam time campaigns [2,3] at GSI, DESY, ESRF, etc.. A consequent development of the detector and readout techniques led to the design and realization of our first Si(Li)-DSSD (double-sided strip detector with 1.0mm² spatial resolution) with 64 preamplifiers with a 1st-stage at cryogenic temperature. This change in readout technique improves the energy resolution to 850eV-900eV at 60keV (ground-side) and 1200eV at 60keV (HV-side) compared to 2000eV at 60keV with a readout with all parts (except the DSSD) kept at room-temperature. The improved energy resolution enhanced the lower energy threshold for a reliable event reconstruction with respect to linear polarization detection of incident photons from 70keV down to 40keV. By this progress we are now able to study a huge variety of transitions in atomic systems that were not accessible for us up to now. Recently we studied, with a focus on future experiments at FAIR at higher event complexities and rates, the possibilities of a reliable identification of the point of interaction within the detector crystal (z-component). The relatively simple geometry of the DSSD allows for identification of the x- and y- position by superposition of the front side and back side strips of the detector. The z-position may be measured by the time of arrival of the electron cloud (hole cloud respectively) at the strip contacts. For our 9.0mm thick Si(Li)-DSSD we measured a electron drift time of 37µm/ns in the depleted bulk. These results correspond well with the values known from literature. From the edges of the drift time spectrum one can derive a time resolution of 20-30ns for the measurement of the z-component. This corresponds to a measurement with a collimated photon fan beam (approx. 1mm FWHM width at the detector surface) hitting the detector at an angle of 35 degree with respect to the surface (figure 1). With the knowledge of the z-component the quality of polarization measurements can be improved with the respect to background suppression. The same is true if we turn the argument of the z-component around. The typical time coincidence resolution with a fast (typically 10ns resolution) external signal is in the order of 80-120ns due to the different path length of the charge depending on the location of the point of interaction inside the bulk. With the z-information this uncertainty in time can be reduced significantly resulting in an improved event identification efficiency.

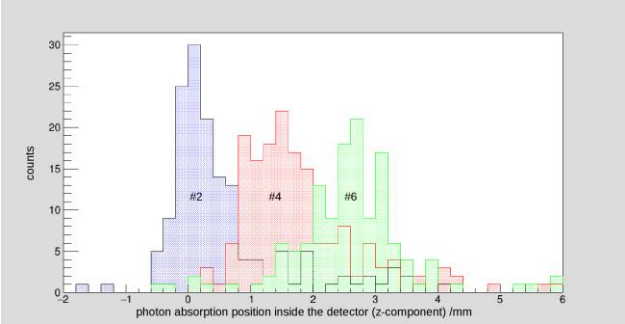

Figure 1: Photon deposition as function of the measured detector position (z-component, which is derived from the time of arrival differences of the charge between the backside contacts and the front side contacts #2, #4, #6)

References

[1] Technical Report of the SPARC collaboration, http://www.gsi.de/sparc

[2] R. Märtin et al., Phys. Rev. Lett. **108**, 26480 (2012)

[3] K.-H. Blumenhagen et al., New Journal of Physics **18**, 103034 (2016)

[4] M. Vockert et al., within this scientific report

Work supported by BMBF Verbundprojekt 05P2015 R&D Beschleuniger/HI Jena/GSI(ESR, SIS, UNILAC). This report is also part of the GSI Jahresbericht 2016 (DOI:10.15120/GR-2017-1)

**Also a part of the GSI Scientific Report* / GSI Report 2017-1

Progress of experimental systems for CRYRING@ESR*†

M. Lestinsky‡ [1], *F. Herfurth*[1], *S. Schippers*[2], *Th. Stöhlker*[1,3,4], *and the APPA collaborations*[1]
[1]GSI, Darmstadt, Germany; [2]JLU Gießen, Gießen, Germany; [3]HI Jena, Germany; [4]IOQ, FSU Jena, Germany

CRYRING@ESR is a new heavy ion storage ring facility at GSI/FAIR and is presently under construction [1-2]. The former Swedish CRYRING was modernized and adapted to its new location. After almost two years, reassembly of the ring in general has been completed and vacuum pumping could be started. Also, the beam transport from ESR to CRYRING has been completed. Figure 1 shows a photograph of the injector beamline and the ring during the end of 2016. During the course of 2016, already the first two beamtime campaigns were dedicated to the commissioning of CRYRING@ESR. During these periods, the low-energy beam extraction from ESR and transport towards CRYRING, as well as — using a beam produced in the local injector of CRYRING — the "first turn" of ions in the ring could be successfully demonstrated. More details about the commissioning are given in [3]. For the machine, the directions are set for going from first turn to a long-lived stored beam. Thus, next steps will be establishing the required ultrahigh vacuum conditions for a long ion beam lifetime, as well as electron cooler operation.

With the machine gradually progressing into regular operation, the experimental systems are presently also being prepared, and CRYRING@ESR in fact offers exciting research opportunities for research on highly charged ions for a large range of scientific fields. In the future, all ions presently available from the GSI accelerator chain can be transported and stored at low energies, between $\sim$ 0.05 to 15 MeV/u with ion beam lifetimes between few seconds to $\sim$ 15 minutes, depending on charge state and energy. Hence, SPARC and FLAIR, but also NuSTAR have formulated extensive research programmes for this facility [4]. The low energy conditions will allow for precision spectroscopy and thus, e.g., allow one to test non-perturbative strong field QED terms, or to study transient quasi-molecular systems. Further, at the border between atomic and nuclear physics, nuclear size effects, hyperfine interactions or exotic couplings between the electronic shell and the nucleus of an ion may be explored. In nuclear physics, storage of bare nuclei at low energies permits to determine fragment distributions unmasked by atomic physics. Under these conditions, e.g., nuclear reactions at the Coulomb barrier or nucleosynthesis of heavy elements in the Gamow window of the p-process may be analyzed.

A first generation of experiments at CRYRING@ESR is being prepared by the German APPA R&D collaboration [5,6] (supported by BMBF Verbundforschung). This instrumentation comprises various installations for a wide range of atomic physics experiments (SPARC collaboration): Electron-ion collision spectroscopy at the electron cooler and an intense transverse electron target, laser- and fluorescence spectroscopy from the visible to the VUV regime, particle detectors, and precise systems to measure electron- and ion energies. Most systems shall be ready for at least rudimentary operation in first experiments during the 2018 beamtime campaings. Also, details of further international projects are presently being worked out. Finally, in order to coordinate the efforts by and resources for the various experiment groups, a new mailing list and a monthly regular meeting have been established (see [1] to sign up).

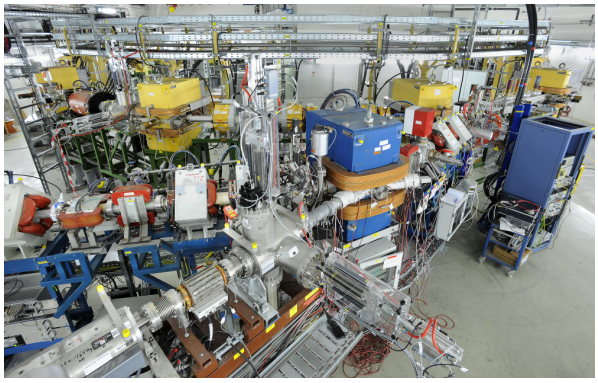

Figure 1: CRYRING@ESR overview. Ions are injected from the local injector or from ESR (diagonally from the lower left) and the ring is in the back (yellow dipole magnets). Photo by G. Otto, GSI, Dec. 2016.

References

[1] `http://www.gsi.de/cryring/`

[2] W. Geithner, et al., "Status and outlook of the CRYRING@ESR project", 2017, Hyperfine Interact., 238, 13

[3] F. Herfurth, et al., "The status of CRYRING@ESR – first turn", GSI annual report 2016, GSI Darmstadt, in print.

[4] M. Lestinsky, et al., "Physics book: CRYRING@ESR", 2016, Eur. Phys. J. Spec. Top. 225, p. 797

[5] `http://appa-rd.fair-center.eu`

[6] Z. Andelkovic, et al. and the SPARC collaboration, "Technical Design Report: Experimental Instrumentation of CRYRING@ESR", 2015, FAIR Darmstadt

*CRYRING@ESR is supported by GSI, HI Jena, Stockholm Univ., Jagiellonian Univ. Kraków, and BMBF Verbundforschung under various contracts

† Also part of the GSI Scientific Report 2016 / GSI Report 2017-1

‡ m.lestinsky@gsi.de

Design of a scintillator-based ion counter for CRYRING@ESR*

P. Pfäfflein[†1,2], *C. Hahn*[1,2], *and Th. Stöhlker*[1,2,3]

[1]Helmholtz Institute Jena, Germany; [2]FSU, Jena, Germany; [3]GSI, Darmstadt, Germany

The observation of recombination processes and their emitted light are a well-known technique that grants information about the atomic structure. This kind of experiment needs the detection of both the emitted light and the charge exchange. In a synchrotron like CRYRING, which is currently being commissioned as part of the new FAIR facility at the GSI Helmholtz Center, ions that have undergone charge exchange will leave the central trajectory, and can be readily detected by a suitably-positioned sensor. For this purpose a versatile, ultra-high vacuum (UHV) compatible and robust particle detector is necessary.

The vacuum level at CRYRING, with pressures as low as $10^{-12}\,\mathrm{mbar}$ [2], requires that all components which are brought into the vacuum are bakeable. This poses a major problem for most of the electronics, which therefore should remain outside the vacuum. We present a design that satisfies this condition, and is both easy to manufacture and convenient to use. It employs a YAP:Ce (cerium-doped yttrium aluminium perovskite) crystal scintillator together with a photomultiplier tube (PMT). YAP:Ce is a fast and comparatively affordable scintillator material, meets the vacuum requirements and is sufficiently resistant to radiation damage [3–5]. The design of the detector head is versatile so that using a different scintillator is possible. In addition, the PMT can be swapped with another optical readout.

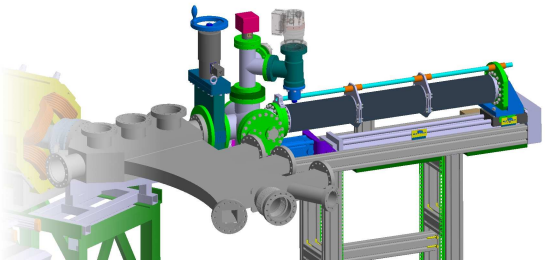

Figure 1: Sketch of CRYRING's detector manipulator, attached with a valve and a 6-way cross to the dipole chamber (viewed in beam direction, with the actual dipole magnet not shown).

The universal manipulator setup, which will be used to interface a variety of detectors to the ring, is sketched in Figure 1. For easy maintenance and installation, the assembly can be separated from the ring vacuum with a valve. A standard CF100 flange, indicated in green on the far side of the manipulator bellows, serves as the detectors' installation point. The actual detector head will rest, when parked, in the 6-way cross.

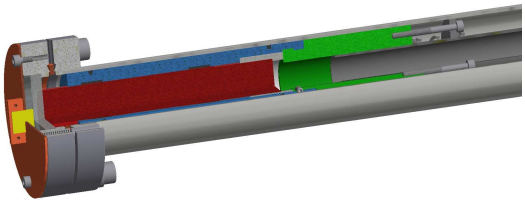

Figure 2: Cutaway view of the detector head with the scintillator (yellow), the PMT (dark red), the PMT housing and adapter to the fastening tube (green, blue and grey around the PMT). The clamp holding the scintillator crystal in place is not shown.

The design, shown in Figure 2, consists of two concentric cylindrical tubes, one as vacuum pocket capped by a window and the other one for the insertion and fastening of the PMT inside its housing. Only the scintillator will be placed inside the vaccum and mounted directly to the fused silica window which will be coupled to the PMT on the atmospheric side. The scintillator crystal can be easily changed via the 6-way cross, without needing to dismount the whole detector. The assembly of the detector and the manipulator will take place in two steps: first, inserting the outer tube into the bellows and applying the vacuum, including baking, and afterwards installing the inner tube with the PMT. The design consists mostly of standard and easy to manufacture components and is therefore adaptable to different manipulator lengths. That way, the setup can be realized as a regularly-installed, general-purpose detector.

References

[1] J. Eichler and Th. Stöhlker, "Radiative electron capture in relativistic ion–atom collisions and the photoelectric effect in hydrogen-like high-Z systems", Phys. Rep. 439 (2007) 1

[2] M. Lestinsky et al., "CRYRING@ESR: A study group report" (2012)

[3] E. Slunga et al., "Scintillation response of BaF_2 and $YAlO_3$:Ce (YAP:Ce) to energetic ions", Nucl. Instr. and Meth. A 469 (2001) 70

[4] S. Westman et al., "Heavy ion detection at extreme high vacuum by means of a YAP:Ce scintillator", Nucl. Instr. and Meth. A 481 (2002) 655

[5] G. Miersch et al., "Fast scintillators as radiation resistant heavy-ion detectors", Nucl. Instr. and Meth. A 369 (1996) 277

* This report is also part of the GSI Scientific Report 2016 / GSI Report 2017-1.

† philip.pfaefflein@uni-jena.de

YAP:Ce-based scintillation devices for heavy ion detection within the Fit-FISIC project*

C. Hahn[†1,2], *P. Pfäfflein*[1,2], *G. Weber*[1,3], *and Th. Stöhlker*[1,2,3]

[1]Helmholtz Institute Jena, Germany; [2]FSU, Jena, Germany; [3]GSI, Darmstadt, Germany

With the advancing realization of the novel FAIR accelerator and ion storage complex, in particular the impending commencement of CRYRING operations (*FAIR Phase 0*), planned experiments such as the Franco-German Fit-FISIC project (***Fi**rst steps **t**owards atomic physics of **F**ast **I**on–**S**low **I**on **C**ollisions*, [1,2]) depend on the availability of robust ion detectors. Among the quite extensive variety of established detection methods, the use of scintillation detectors provides a solution that is both economical as well as versatile with respect to the ion energies and species accessible [3]. While common plastic scintillators usually suffer from fatal radiation damage due to the localized nature of ion energy deposition – the so-called *Bragg peak* –, crystalline substances such as YAP:Ce (cerium-doped yttrium aluminium perovskite) have been known to exhibit a significant degree of radiation hardness [4].

Commonly the readout of such scintillator detectors is accomplished with a photomultiplier tube of suitable spectral sensitivity. However, some experiments require position resolution that this approach fails to provide, e.g. to distinguish the trajectories taken by different charge states. A promising alternative is the use of so-called silicon photomultiplier (SiPM) devices. This novel detector type, sometimes called "multi-pixel photon counters", can be described as an array of parallelly connected avalanche photodiodes with a typical size of $25\,\mu\mathrm{m}$, and provides a compact, low-voltage and easily tileable readout solution. In addition, the devices' inherent high gain affords single-particle detection efficiency.

Pursuing this approach, a demonstrator setup is presently investigated at Helmholtz Institute Jena. It consists of an 8×8 assembly of square SiPM devices with an edge length of $6\,\mathrm{mm}$ each, manufactured by SensL Technologies Ltd., and readout electronics furnished by Vertilon Corporation. A dedicated breakout board allows for custom signal processing, e.g. for use in experiments where timing information is critical. The actual YAP:Ce scintillator crystal has a thickness of $1\,\mathrm{mm}$ and was manufactured by CRYTUR spol.s.r.o. It is attached to the SiPM array with an aluminium frame for easy mounting; a photograph of this detector head is reproduced as an inset in figure 1. At the scintillator's primary emission wavelength of $370\,\mu\mathrm{m}$, the photon detection efficiency of the SiPMs is on the order of a favorable 40%, on par with typical values achieved with conventional photomultiplier tubes.

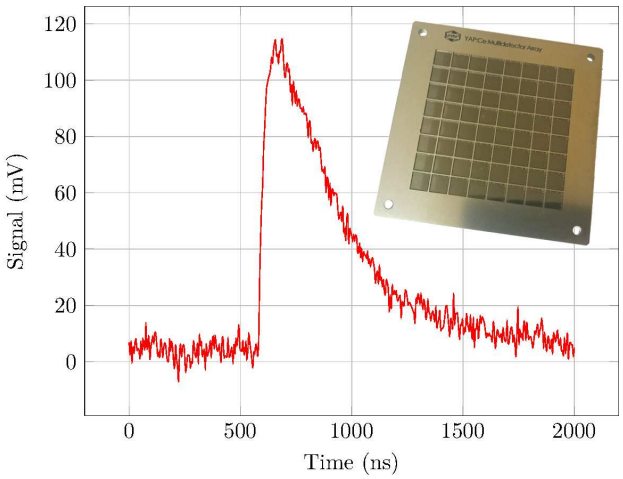

Figure 1: Oscilloscope signal from the SiPM readout of a $1\,\mathrm{mm}$-thickness YAP:Ce crystal scintillator, irradiated with $662\,\mathrm{keV}$ photons from a ^{137}Cs source. The inset shows the scintillator array bonded to the SiPM detector head, of which only the 8×8 segmentation is visible.

Figure 1 also displays the oscilloscope trace of the observed signal when the scintillator–SiPM assembly is irradiated with $662\,\mathrm{keV}$ photons from a ^{137}Cs γ source. The peak exhibits a steep rising flank with a rise time of approximately $50\,\mathrm{ns}$ (10%–90% of maximum signal). The falling flank, on the other hand, is decidedly longer, with its slope primarily determined by the quenching resistors that halt the avalanche. In any case, operation at a maximum event rate of some $100\,\mathrm{kHz}$ is obviously feasible.

Pending availability of the necessary vacuum components, a characterization measurement with ion energies of ca. $10\,\mathrm{MeV}$ is currently being set up at HI Jena.

References

[1] Fit-FISIC Collaboration, ed., "Project Fit-FISIC: Scientific Document" (2013)

[2] C. Hahn et al., "Development of ion detectors for the 1–10 MeV/u energy range", GSI Scientific Report 2014 (2015) 228

[3] W. Klamra et al., "Response of BaF_2 and YAP:Ce to heavy ions", Nucl. Instrum. and Meth. A 444 (2000) 626

[4] M. Tokman et al., "Towards a Determination of QED Effects in Cu-Like Pb Recombination Resonances Near Threshold", Phys. Scripta 2001 (2001) 406

* We gratefully acknowledge support by the DFG under grant no. STO 346/4-1. This report is also part of the GSI Scientfic Report 2016 / GSI Report 2017-1.

† christoph.hahn@uni-jena.de

Design studies for Cryogenic Current Comparators (CCC) at FAIR

F. Kurian[1#,2,3], T. Sieber[1], M. Schwickert[1], R. Stolz[4], T. Stöhlker[1,2]
[1]GSI, Darmstadt, Germany; [2]Helmholtz Institute, Jena, Germany; [3]Friedrich-Schiller University, Jena Germany,
[4]IPHT Jena, Germany

For installation in the FAIR accelerator facility, development work for an advanced Cryogenic Current Comparator (CCC-XD) system is ongoing in association with the collaborating partners at TU-Darmstadt, FSU- Jena, CERN-Geneva and IPHT-Jena [1]. The design of a universal cryostat fulfilling the special boundary conditions given in the FAIR beam lines has been worked out, with some of its components still undergoing optimization.

Optimization of the CCC Design for FAIR

The superconducting magnetic shield of the new CCC systems should cope with larger dimensions given by large beam tube diameters (160 mm) of FAIR beam lines. However it was already shown that a larger diameter of the magnetic shield results in diminished field attenuation [2]. At the same time, given by the requirement of a compact cryostat with separated insulation vacuum, a minimum possible outer diameter of the shielding had to be achieved by simulations. To ensure minimum temperature fluctuations on the liquid helium surfaces, which were previously shown to cause large drifts in the CCC output signal [3], the thermal load had to be minimized even though a room temperature UHV beam tube needed to be introduced as a 'warm-hole' through the cryostat. The cross-sectional view in figure 1 shows the design of the cryostat. Besides a stable operation at FAIR, it also has to provide easy access to all internal parts to allow for exchange of CCC components during future development work. Therefore the isolation vacuum chamber consists of a stainless steel frame with Aluminum windows, which can easily be removed.

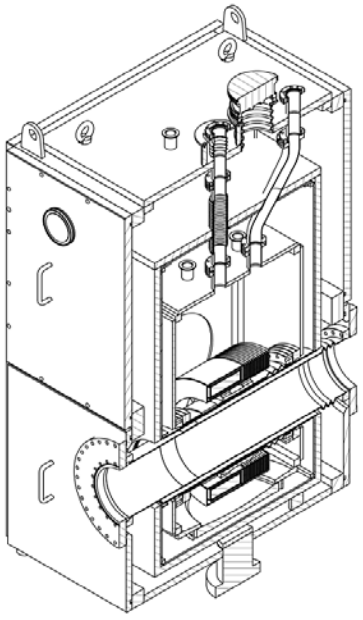

Figure 1: Schematic design of the CCC system for FAIR

Radially Stacked Magnetic Shield for CCC

For the operation of CCC system as a standard diagnostic instrument in FAIR beam lines, large baseline drifts (long term drifts as well as instantaneous drifts) due to temperature fluctuations has to be minimized. Hence to characterize both types of drifts, detailed experiments on the magnetic shield are still in progress. Preliminary results show clear indications that the high permeability ring core (which acts as a flux concentrator and enhances the magnetic field coupled to the sensor unit) is the main source of the drifts.

In order to achieve better current resolution through enhanced field attenuation and removal of ring core, which additionally is a source of Barkhausen noise, a radially stacked design of magnetic shield is proposed. In this scheme, unlike the magnetic field pickup by the pickup coil, the magnetic shield itself acts as the single turn pickup coil. The superconducting screening current will in this case be inductively coupled to a next generation dc-SQUID with an inductance matched to the shielding. This combination is planned to be tested in the new cryostat, which will in installed in the Cryring@ESR storage ring. Depending on the performance compared to the classical solution, application in the FAIR facility is foreseen.

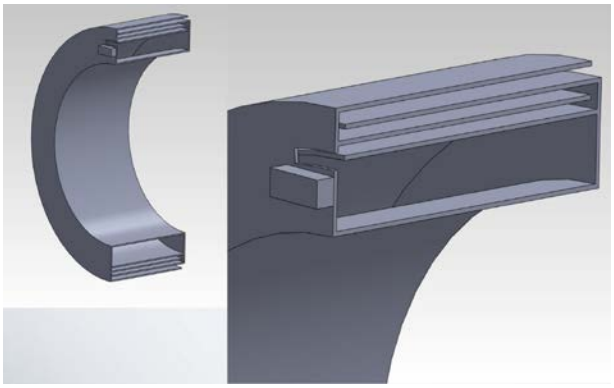

Figure 2: Radially stacked meander CCC.

References

[1] T. Sieber, F. Kurian, M. Schwickert et. al, "Optimization studies for an advanced Cryogenic Current Comparator System for FAIR", Proceedings of IBIC 2016

[2] H. De Gersem, N. Marsic, F. Kurian, T. Sieber et al. "Finite-element simulation of the performance of a superconducting meander structure shielding for a cryogenic current comparator", Nucl. Instrum. Methods Phys. Res., Sect. A, 840:77 86, 2016

[3] F. Kurian, "Cryogenic Current Comparator for Precise Ion Beam Current Measurements", PhD thesis, Goethe University, Frankfurt am Main, March 2016

Inductance measurements at the Lambda point*

J. Golm[† 1,2], *R. Neubert*[2], *and V. Tympel*[1,2]

[1]Helmholtz-Institute Jena, Jena, Germany; [2]Institute of Solid State Physics FSU, Jena, Germany

There are good physical reasons to work with superfluid He II below the Lambda-point. We have checked the pressure sensitivity of modern ferromagnetic core materials with thin nanocrystalline layers.

Introduction

Cryogenic current comparators (CCC) are using flux concentrator rings to capture the magnetic field of the moving particles. Unpublished former measurements showed a pressure sensitivity of the CCC signal. Because of the well-known relationship between pressure and temperature of helium [1] a seperation of the pressure driven change of the inductance has to be examined.

@ Lambda point

It is known that the specific heat capacity of helium has a very high peak at the λ-point [2]. To achieve this temperature with large samples (diameter 300 mm x high 100 mm) we used a stainless steel wide neck cryostat, a gas flow control unit and two scroll pumps SC15D with a suction of 15 m^3/h each. Figure Fig. 1 shows an image of the wide neck cryostat and the diagram of the pumping setup. Starting at 4.2 K @ 100 kPa we are below the λ-point (2.17 K and 5 kPa) 6 hours later as shown in Fig. 2. Now we can increase the pressure very fast with a speed of 10 kPa/min with a long hold of temperture of the liquid helium at the λ-point. As Fig. 3 shows we only find a very small change of the inductance of 0.02 %. During the measurement the change of the temperature is only about 14 mK (0.65 %) whereas the change of pressure is 90 kPa (90 % of normal pressure). The change of pressure of a running CCC at 4.2 K is only in the range of 5 kPa. The measurements at the λ-point shows that any changes of the CCC signal can not be caused by pressure on the core.

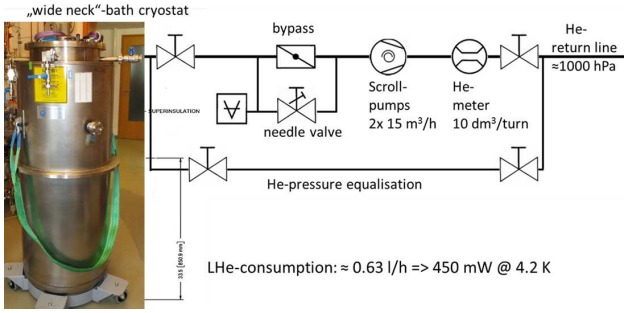

Figure 1: Image of the cryostat and the diagram of the pumping setup with gas flow control unit and scroll pumps.

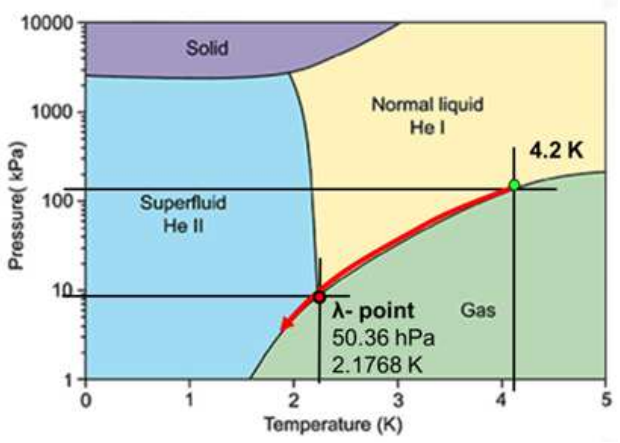

Figure 2: Phase diagram of 4He, after [3].

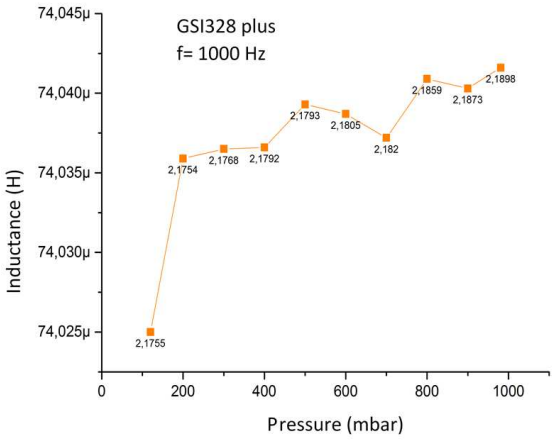

Figure 3: Pressure independence of the inductance at the Lambda point and at a frequency of f = 1000 Hz.

References

[1] R. D. McCarty, "Thermodynamic Properties of Helium-4 from 2 to 1500 K at Pressures to 108 Pa", J. Phys. Chem. Ref. Data, Vol. 2, No. 4, 1973

[2] M. J. Buckingham, W. M. Fairbank, "The nature of the λ-transition in liquid helium", Progress in Low Temperature Physics, Vol. 3, 1961, pp. 80–112

[3] www.superfluid.cz/?lang=en&page=intro

* supported by BMBF 05P15SJRBA and CERN collaboration agreement KE2915/BEA; larger version published in annual report 2016 of [2].

† Jessica.Golm@cern.ch

Precision induction measurements of flux concentrators*

V. Tympel† [1,2], *R. Neubert*[2], *and J. Golm*[1,2]
[1]Helmholtz-Institute Jena, Jena, Germany; [2]Institute of Solid State Physics FSU, Jena, Germany

Cryogenic current comparators are using flux concentrators. We are now able to design and to characterise large flux concentrators for applications at temperatures below 2 K.

Introduction

Cryogenic current comparators (CCC) as non-destructive, highly-sensitive charge particle properties beam monitoring devices are using flux concentrator rings to capture the magnetic field of the moving particles. The new FAIR accelerator facility at GSI Darmstadt requires extended versions of CCCs with larger diameters called CCC-XD [1].

Flux concentrator

Figure 1 shows the complete core package consisting of three single ribbon cores of approximately 1500 thin layers of special tempered NANOPERM®. For the core package characterisation a high-precision L_S-R_S-measurement setup based on an Agilent E4980A LCR-meter for the measurement of the series inductance L_S and the series resistance R_S, a LabVIEW script to control the hardware, a C++ programme for the data analysis and a wide-neck cryostat were developed. Two scroll pumps (SC 15D) allow a temperature range from 300 K down to below 2 K. Due to the thermomagnetic annealing process of the amorphous basic material (recipe) a variation of the electrical parameter is possible.

Figure 1: Core package GSI328plus with an outer diameter of 300 mm and a depth of 100 mm.

* supported by BMBF 05P15SJRBA and CERN collaboration agreement KE2915/BEA; larger version published in annual report 2016 of [2].
† v.tympel@gsi.de

Figure 2 shows that different recipes lead to different electro-magnetic properties. The results of an orderd recipe can be different but the sample variation of the same batch is very small (Fig. 3).

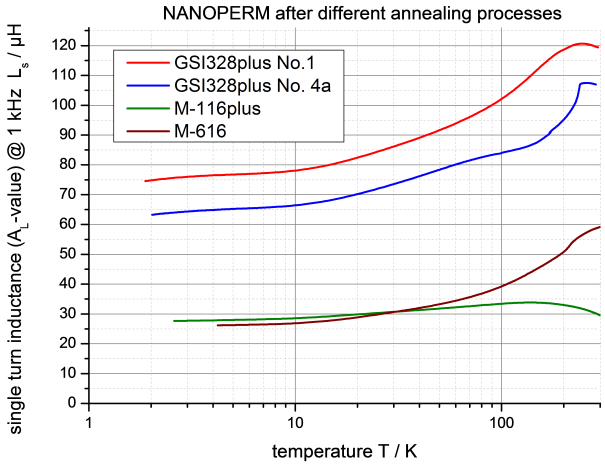

Figure 2: Results of different thermo-magnetic recipes [2].

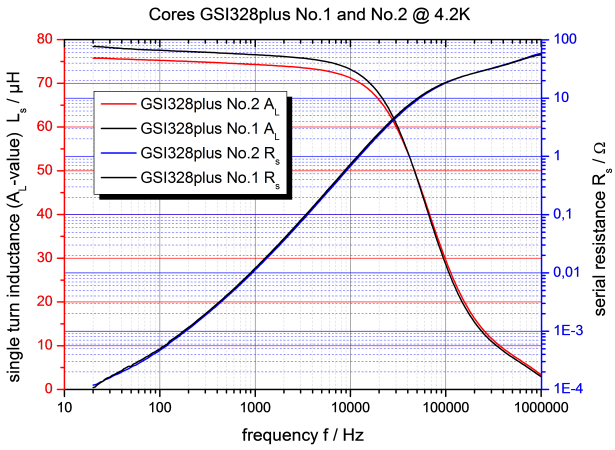

Figure 3: Two core packages of the same batch [2].

References

[1] M. Schwickert et al., "Status of beam current transformer developments for FAIR", Proceedings of IBIC2016, Barcelona, Spain, Pre-Release Snapshot TUPG50

[2] V. Tympel et al., "The next generation of cryogenic current comparators for beam monitoring", Proceedings of IBIC2016, Barcelona, Pre-Release Snapshot TUPG43

Hyperfine splitting in ^{209}Bi^{80+}, ^{209}Bi^{82+} and beyond*

R. Sánchez[1], J. Ullmann[2,3], Z. Andelkovic[1], C. Brandau[1,4], A. Dax[5], W. Geithner[1], Ch. Geppert[3], C. Gorges[3], M. Hammen[6,7], V. Hannen[8], S. Kaufmann[3], K. König[3], Y. Litvinov[1], M. Lochmann[3], B. Maass[3], J. Meisner[9], T. Murböck[10], M. Schmidt[9], S. Schmidt[3,7], M. Steck[1], Th. Stöhlker[1,2], R. C. Thompson[11], C. Trageser[4], J. Vollbrecht[8], C. Weinheimer[8], and W. Nörtershäuser[3]

[1]GSI Helmholtzzentrum für Schwerionenforschung, Darmstadt, Germany; [2]HIJ, Jena, Germany; [3]IKP, TU Darmstadt, Germany; [4]I. Physikalisches Institut, JLU, Germany; [5]PSI, Villigen, Switzerland; [6]HIM, Mainz, Germany; [7]IKC, Universität Mainz, Germany; [8]IKP, Universität Münster, Germany; [9]PTB, Braunschweig, Germany; [10]IAP, TU Darmstadt, Germany; [11]QOLS Group, Department of Physics, Imperial College London, UK

The specific difference between the ground state hyperfine splittings (hfs) in hydrogen-like and lithium-like ions of the same isotope was suggested about fifteen years ago as the ultimate tool to prove bound-state QED in the strong magnetic field generated by the heavy nucleus [1].

The isotope of bismuth, ^{209}Bi, exhibits both ground-state hyperfine transitions very close to the visible spectrum and therefore they can be probed by laser spectroscopy. The $1s$ hfs in hydrogen-like bismuth (^{209}Bi^{82+}) was measured by direct laser spectroscopy at the experimental storage ring (ESR) in 1994 [2]. Seventeen years later and using an improved laser spectroscopic technique [3] at the same ring we found the $2s$ hfs in lithium-like bismuth (^{209}Bi^{80+}) [4]. Combined with a new measurement of the $1s$ hfs in the hydrogen-like we found good agreement with the theoretical prediction. Yet the accuracy of our result was limited at that time by the calibration of the electron-cooler voltage, determining the velocity of the ions in the ring [4].

We have repeated this experiment in 2014. This time we were able to monitor the electron-cooler voltage *in situ* using a voltage divider provided by PTB in Braunschweig. First results on the $1s$ hfs in hydrogen-like bismuth using a coasting beam have been already published in [5].

After two years for studying potential systematic errors we have now achieved relative accuracies at the 10^{-5} level for both hyperfine transitions [6]. These are the most accurate transition wavelengths measured in a heavy highly charged ion so far. This improvement has finally allowed us to improve the accuracy on the specific difference by an order of magnitude. A significant fact is that our new result shows now a 7σ-difference to the latest theoretical prediction [7]. Such a large discrepancy was not expected by theory and therefore it has put the specific difference into question as a tool to test QED in strong fields.

It has, however, been pointed out that the specific difference is still sensitive to the nuclear magnetic moment of $\mu(^{209}\mathrm{Bi})$ [7, 8]. A small variation from the tabulated value could bring theory and experiment into agreement. Therefore, there is also a need to remeasure this ground state nuclear property. A new measurement of $\mu(^{209}\mathrm{Bi})$ via nuclear magnetic resonance is in preparation at TU Darmstadt and on a long-term perspective, a measurement of the hfs in both ion species is planned at the SpecTrap Penning trap [9] and of the magnetic moment directly on hydrogen-like bismuth at the Penning trap ARTEMIS, which are both installed at HITRAP/GSI.

In order to confirm both, the reliability of the proposed nuclear structure independence in the specific difference as well as any assumption of a different nuclear magnetic moment value, we are now considering to measure the hfs in hydrogen-like and lithium-like of a second isotope. Two candidates are envisaged: ^{207}Bi and ^{208}Bi. Their magnetic moments are ascribed to the single proton outside the ^{208}Pb-core and the additional neutron holes below the $N = 126$ shell-closure.

The specific difference in ^{207}Bi is expected to have a deviation that scales with the magnetic moment compared to that in ^{209}Bi because of the similar magnetic moment and spin. In the case of ^{208}Bi, a new measurement of the magnetic moment relative to $\mu(^{209}\mathrm{Bi})$ has recently been perform at COLLAPS/ISOLDE by collinear laser spectroscopy [10]. If the moment of ^{209}Bi is really different from the literature value, then we expect a similar disagreement for the specific difference in the case of ^{208}Bi. In case that our disagreement with theory is an artifact due to an incomplete cancellation of the Bohr-Weisskopf effect in the specific difference, the deviation for ^{208}Bi should not scale with the magnetic moment since a considerably different Bohr-Weisskopf effect is expected for this isotope with a different spin and nuclear magnetism distribution. Bound-state strong-field QED can only be proven if this cancellation works as proposed in [1].

* Work supported by BMBF under Contract 05P15RDFAA, 05P12PMFAE, 06GI947 and 05P12R6FAN, by the Helmholtz-Association under Contract HGF-IVF-HCJRG-108, the Helmholtz International Center HIC4FAIR, and by HGS-HiRe.

References

[1] V. Shabaev *et al.* Phys. Rev. Lett **86** (2001) 3959.

[2] I. Klaft *et al.* Phys. Rev. Lett. **73** (1994) 2425.

[3] R. Sánchez *et. al.* J. Phys. B. (2017)

[4] M. Lochmann *et al.* Phys. Rev. A **90** (2014) 030501.

[5] J. Ullmann *et al.* J. Phys. B **48** (2015) 144022.

[6] J. Ullmann *et al.* submitted.

[7] A. V. Volotka *et al.* Phys. Rev. Lett. **108** (2012) 073001.

[8] A. V. Volotka *priv. comm.* (2016).

[9] T. Murböck *et al.* Phys. Rev. A **94** (2016) 043410.

[10] S. Schmidt *et al.* to be published.

High-resolution wavelength-dispersive spectroscopy of K-shell transitions in hydrogen-like gold

T. Gassner[1,2], M. Trassinelli[3], R. Heß[2], U. Spillmann[1,2], D. Banaś[4], K.-H. Blumenhagen[1], F. Bosch[2], C. Brandau[2,5], W. Chen[2], Chr. Dimopoulou[2], E. Förster[1,6], R.E. Grisenti[2,7], A. Gumberidze[2], S. Hagmann[2,7], P.-M. Hillenbrand[2], P. Indelicato[8], P. Jagodzinski[4], T. Kämpfer[1], Ch. Kozhuharov[2], M. Lestinsky[2], D. Liesen[2], Yu. A. Litvinov[2], R. Loetzsch[1], B. Manil[9], R. Märtin[1], F. Nolden[2], N. Petridis[2,7], M. S. Sanjari[2], K.S. Schulze[1], M. Schwemlein[1], A. Simionovici[10], M. Steck[2], Th. Stöhlker[1,2,6], C. I. Szabo[11], S. Trotsenko[1], I. Uschmann[1,6], G. Weber[1,6], O. Wehrhan[1], N. Winckler[2], D.F.A. Winters[2], N. Winters[2], E. Ziegler[1,2], and H.F. Beyer[2]

[1]Helmholtz-Institut Jena, Jena, Germany; [2]GSI Helmholtzzentrum, Darmstadt, Germany; [3]Institut des NanoSciences de Paris, CNRS-UMR 7588, Sorbonne Universités, UPMC Univ Paris 06, 75005, Paris, France; [4]Institute of Physics, Jan Kochanowski University, PL-25-406 Kielce, Poland; [5]Institut für Atom und Molekülphysik, Justus-Liebig-Universität, Gießen, Germany; [6]Inst. für Optik und Quantenelektronik, Friedrich-Schiller-Universität, Jena, Germany; [7]Institut für Kernphysik, Goethe-Universität, Frankfurt am Main, Germany; [8]Laboratoire Kastler Brossel, CNRS-UMR 8552, Collège de France, ENS-PSL Research University, Sorbonne Universités, UPMC Univ Paris 06, 75005, Paris, France; [9]Laboratoire de Physique des Lasers (LPL) UMR 7538 CNRS - Université Paris 13, Villetaneuse, France; [10]ISTerre, Observatoire des Sciences de l'Univers, BP 53, 38041 Grenoble, France; [11]Laboratoire Kastler Brossel, Sorbonne Universités, UPMC Univ. Paris 06, Case 74; 4, place Jussieu, 75005 Paris, France; [12]ESRF, Grenoble, France

Aiming for an accurate testing of the QED effects on the ground state binding energy in high-Z, H-like ions, novel high resolution x-ray spectrometer apparatus has been developed for experiments at the Experimental Storage Ring (ESR) at GSI, Darmstadt. Namely, the twin crystal-spectrometer assembly, Bi-FOCAL, operated in the FOcusing Compensated Asymmetric Laue geometry has been arranged for accurate x-ray spectroscopy at the ESR gas jet [1]. In a dedicated beamtime at the ESR, Lyman-α transitions of H-like Au^{78+} were measured in high resolution via spectroscopy of the corresponding x rays located near 63 keV in the laboratory system [2].

This experiment represents the first high-resolution wavelength-dispersive measurement of hard x-rays stemming from a high-Z H-like ion. It demonstrates the feasibility of this method at heavy-ion storage rings, such as ESR and represents an important milestone towards achieving a sensitivity to higher-order QED effects.

Since this is a new measurement method dealing with crystal spectroscopy of relativistic high-Z ions, for obtaining at accurate result, particular attention has to be paid to systematic effects. Therefore, in the aftermath of the main experiment, few auxiliary measurements have been conducted each of the them addressing different possible sources of systematic uncertainties [3, 4, 5].

In table 1, we show a summary of the different systematic effects and the associated uncertainties on the Lyman-α_1 transition energy which is used to deduce the 1s Lamb shift in H-like gold. As one can see from the table, the statistical uncertainty (stemming from the determination of the peak position) of only 2.2 eV has been achieved which is unique for a crystal spectrometer operated in the region of hard x rays of H-like high- Z ions. The systematic effects give the main contribution to the total uncertainty and have to be reduced in future runs. The ion-beam velocity can already be determined with a much higher accuracy using a high-voltage divider from the Physikalisch-Technische Bundesanstalt (PTB) in the electron-cooler terminal. With a slightly modified assembly it will also be possible to measure the gas-target position relative to the detector-crystal position in situ, which will almost entirely eliminate these systematic uncertainties avoiding supplementary experiments alltogether.

Table 1: Different systematic effects and the associated uncertainties on the total Lyman-α_1 transition energy (preliminary results).

Contribution	Value (eV)
Preliminary Transition Energy	$71\,539.8(2.2)$
Temporal Drift	(2.8)
Gas-Target Position	(13.0)
Ion-Beam Velocity	(4.3)
Detector-Crystal Position	(5.1)

References

[1] H. F. Beyer, *et al.* 2015 *J. Phys. B* **48** 144010

[2] H. F. Beyer, *et al.* GSI Report 2013-1, 310 p. (2013)

[3] H. F. Beyer, *et al.* GSI Report 2014-1, 155-156 p. (2014)

[4] T. Gassner, H. F. Beyer GSI Report 2015-1, 216 p. (2015)

[5] T. Gassner, *et al.* GSI Report 2016-1, 135 p. (2016)

[1]

[2]

[1]Also part of the GSI Scientific Report 2016 / GSI Report 2017-1

[2]supported by contract ENSAR 262010

Asymmetries of the electron cusp in heavy-ion atom collisions*†

P.-M. Hillenbrand‡ [1,2], *S. Hagmann*[1], *D. Banaś*[3], *M. Benis*[4], *C. Brandau*[5], *E. De Filippo*[6], *O. Forstner*[1,7,8], *T. Gassner*[1,7,8], *J. Glorious*[1], *R. Grisenti*[1], *A. Gumberidze*[1], *D. Guo*[9], *B. Hai*[9], *M. O. Herdrich*[7,8], *C. Kozhuharov*[1], *M. Lestinsky*[1], *Yu. A. Litvinov*[1], *E. V. Pagano*[10], *N. Petridis*[1], *S. Sanjari*[1], *D. Schury*[1,5], *U. Spillmann*[1], *C. Trageser*[1,5], *S. Trotsenko*[1], *M. Vockert*[7,8], *G. Weber*[8], *and Th. Stöhlker*[1,7,8]

[1]GSI, Darmstadt, Germany; [2]Columbia University, New York City, USA; [3]Jan Kochanowski University Kielce, Poland; [4]University of Ioannina, Greece; [5]Justus-Liebig-Universität Giessen; [6]INFN Catania, Italy; [7]Friedrich-Schiller-Universität, Jena, Germany; [8]Helmholtz Institut, Jena, Germany; [9]IMP Lanzhou, China; [10]INFN-LNS, Catania, Italy

The well-known experimental technique of zero-degree cusp electron spectroscopy has been extended towards heavy-ion atom collisions at near-relativistic collision velocities, at which new effects of asymmetries in the electron cusp arise.

In collisions of heavy highly-charged projectile ions with atomic targets, the energy distribution of the emitted electrons is a characteristic observable for the underlying elementary charge-transfer processes [1]. At the experimental storage ring ESR of the heavy-ion accelerator facility GSI, a dedicated magnetic electron spectrometer was installed downstream from the supersonic gas-jet target, which enables the measurement of high-energetic electrons emitted in ion-atom collisions, with electron velocities similar to the projectile velocity, emitted within a small cone in the forward direction (Figure 1). This technique provides the ability to extend the well known study of zero-degree cusp electrons towards heavy-ion atom collisions at near-relativistic projectile energies.

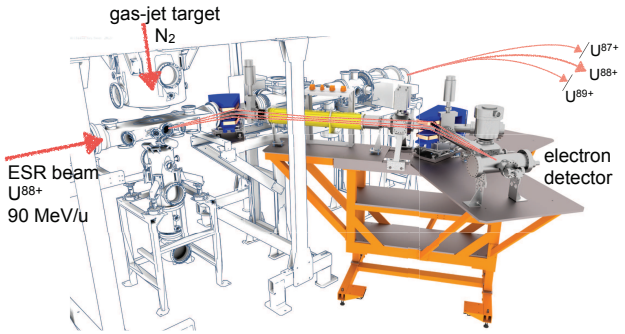

Figure 1: Magnetic electron spectrometer at the ESR.

Through the electron-loss-to-continuum (ELC) cusp, double-differential cross sections of projectile ionization can be studied even for the heaviest few-electron projectiles [2]. But also a new channel opens up, the radiative electron capture to continuum [3], which can be directly compared to its non-radiative counterpart [4]. Using the electron spectrometer in combination with detectors for emitted x rays and charge-exchanged projectiles, the study of the collision system $U^{88+}(1s^2 2s^2) + N_2$ @ 90 MeV/u revealed all three processes, each characterized by a unique shape of the electron cusp [5].

Furthermore, the process of electron loss to continuum was investigated for multi-electron projectiles in the collisions of U^{28+} with gaseous targets of H_2, N_2, and Xe at collision energies of 30 and 50 MeV/u. The experimental data revealed a significant electron cusp asymmetry, which increases towards heavier targets. This observation is inconsistent with presently available theories [6].

As a next step, the electron spectra for $U^{89+}(1s^2 2s)$ ions colliding with gaseous targets of N_2 and Xe have recently been measured in the beamtime of 2016, at a projectile energy of 76 MeV/u, i.e., just above the threshold for electron impact ionization of the L-shell of uranium. In these measurements, the studied electron emission energy was extended considerably, stretching both over the full electron cusp and the binary-encounter peak. At the studied collision velocity, relativistic continuum-distorted-wave (CDW) calculations of projectile ionization show a deviation of the electron energy distribution from first-oder perturbation theory due to the effect, that the electron emitted by the projectile is attracted by the target nucleus. The experimental results motivate further developments of relativistic theories describing charge-changing processes in heavy-ion atom collisions.

References

[1] D. H. Jakubaßa-Amundsen 2003 *J. Phys. B* **36** 1971

[2] P.-M. Hillenbrand *et al.* 2014 *Phys. Rev. A* **90** 042713

[3] P.-M. Hillenbrand *et al.* 2014 *Phys. Rev. A* **90** 022707

[4] P.-M. Hillenbrand *et al.* 2015 *Phys. Rev. A* **91** 022705

[5] P.-M. Hillenbrand *et al.* 2015 *J. Phys. Conf. Ser.* **635** 012011

[6] P.-M. Hillenbrand *et al.* 2016 *Phys. Rev. A* **93** 042709

* also part of the GSI Scientific Report 2016 / GSI Report 2017-1.

† This work was supported by the Helmholtz-CAS Joint Research Group HCJRG-108. C.B. acknowledges support by BMBF (contracts 05P12R6FAN and 05P15RGFAA). This project has received funding from GSI Helmholtzzentrum für Schwerionenphysik GmbH under the grant number GSI-TNA-002.

‡ p.m.hillenbrand@gsi.de

Proton and α capture studies for nuclear astrophysics at GSI storage rings*

Jan Glorius[1,#], C. Langer[2], Z. Slavkovská[2], Y. Litvinov[1], R. Reifarth[2], C. Brandau[1,7], B. Brückner[2], X. Cheng[3], T. Davinson[4], P. Erbacher[2], S. Fiebiger[2], T. Gassner[1], A. Gumberidze[1], G. Gyürky[5], K. Göbel[2,1], M. Heil[1], R. Hess[1], P. M. Hillenbrand[1], O. Hinrichs[2], B. Jurado[6], C. Kozhuharov[1], D. Kurtulgil[2], G. Lane[8], C. Lederer-Woods[4], M. Lestinsky[1], S. Litvinov[1], B. Löher[1], F. Nolden[1], N. Petridis[1], U. Popp[1], M. Reed[8], S. Sanjari[1], H. Simon[1], U. Spillmann[1], M. Steck[1], T. Stöhlker[1,9], T. Szücs[5], B. Thomas[2], M. Träger[1], H. Törnqvist[1], S. Torilov[10], C. Trageser[1], S. Trotsenko[1], M. Volknandt[2], M. Weigand[2], C. Wolf[2] and P. J. Woods[4]

[1]GSI Darmstadt, Germany | [2]Goethe University Frankfurt, Germany | [3]Institute of Modern Physics, Lanzhou, China
[4]University of Edinburgh, UK | [5]ATOMKI Debrecen, Hungary | [6]CENBG, France | [7]JLU Gießen, Germany
[8]Australian National University, Australia | [9]HI Jena, Germany | [10]Saint Petersburg State University, Russia

The ^{124}Xe(p,γ) reaction has been measured for the first time at energies around the Gamow window by using stored ions at the ESR facility. The desired beam energies below 10 MeV/u introduced new experimental challenges like windowless ions detection under UHV conditions, extremely short beam lifetimes and efficient beam deceleration and cooling, all of which have been successfully met.

In the nucleosynthesis of the so-called *p* nuclei radiative capture reactions like (p,γ) or (α,γ) play an important role to model the reaction network and to explain the stellar production yields in different explosive scenarios [1]. Most of the key reactions involve radioactive nuclei [2] and can be studied solely in inverse kinematics. The GSI facility offers the unique possibility to produce such exotic ions and to store them in the experimental storage ring, ESR, and eventually in the CRYRING. This setting allows one to use the limited intensities available for radioactive ions with maximum efficiency.

In a first step, fully-stripped ions are stored at beam energies below 10 MeV/u. Subsequently, nuclear reactions are introduced by colliding the stored ions with the internal jet target that consists of either hydrogen or helium gas for (p,γ) or (α,γ) reactions, respectively. Ions, which capture a proton or an α particle at the target, are separated from the stored beam in the next dipole magnet and are detected by UHV compatible double-sided silicon-strip detectors (DSSSD) with a 100% efficiency. Due to atomic interactions the lifetime of the highly charged beam is on the order of seconds. However, the dominant mechanism reflected by this is the well-known radiative electron capture (REC), which can be used for normalization by employing high resolution x-ray spectroscopy around the target.

The very first measurement in the ESR was performed with a beam of stable $^{124}Xe^{54+}$ ions decelerated to and stored at energies between 5.5 MeV/u and 8 MeV/u to study the reaction ^{124}Xe(p,γ)^{125}Cs. The spacial resolution of the employed DSSSD allowed a clear identification
of the (p,γ) signal sitting on a background of elastically scattered ions, as shown in Fig. 1. Similar signals could be identified for five different beam energies in the aforementioned energy range. The analysis of the data set is ongoing within a phd project.

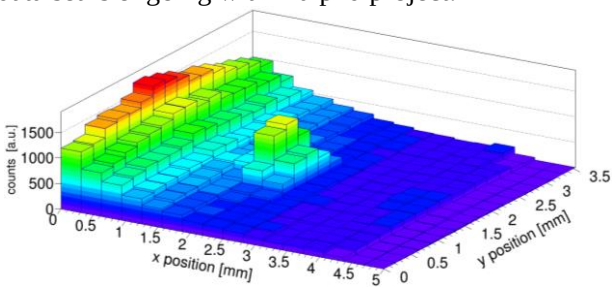

Figure 1. 2D map of the DSSSD data taken at 7 MeV/u. The peak contains the (p,γ) products sitting on a distribution of elastically scattered ions.

In the future, first reaction studies on radioactive nuclei are planned and will be carried out using the ESR setup described above. For energies below 4 MeV/u the newly installed CRYRING facility [3] is ideally suited to serve as a low-energy extension of the ESR. Corresponding experimental equipment is already being designed and will be ready for first experiments in 2018.

This project has received funding from the European Research Council (ERC) under the European Union's Horizon 2020 research and innovation programme (grant agreement No 682841 "ASTRUm")

References

[1] M. Pignatari *et al.* 2016
Int. J. Mod. Phys. E **25** 1630003
[2] T. Rauscher *et al.* 2016
Mon. Not. R. Astron. Soc. **463** 4153
[3] M. Lestinsky *et al.* 2016 *EPJ ST* **255** 5

* also part of the GSI Scientific Report 2016 / GSI Report 2017-1

j.glorius@gsi.de

A new semi-empirical formular for total electron loss by energetic ions*

G. Weber[1,2]

[1]HI-Jena, Germany; [2]GSI, Darmstadt, Germany

Charge-changing processes, i. e. loss or capture of electrons, occurring in ion-atom and ion-ion collisions belong to the most basic interactions in all types of plasmas. Moreover, in accelerators interactions between projectile ions and the residual gas can lead to a change of the projectile charge state. In the presence of dispersive ion optical elements, the trajectories of up- or down-charged ions do not match the one of the reference charge state, resulting in a successive defocussing and, as a consequence, loss of beam intensity. Moreover, ions impinging on the beam line walls give rise to several unwanted effects, such as increased radiation levels and significant degraded vacuum conditions due to ion-impact induced desorption. For the FAIR project, in order to reach highest beam intensities, while minimizing the limitations induced by space charge, and avoiding losses in stripper targets, the use of low- to medium-charged, many-electron ions is planned [1]. However, in the relevant energy region from 10 MeV/u up to a few GeV/u the number of bound electrons of these ions is far above that of the corresponding equilibrium charge state, making projectile stripping, sometimes also referred to as electron loss, the dominant beam loss process. Thus, for the planning of future accelerators and ion beam experiments, precise knowledge of the stripping cross sections of many-electron projectiles is necessary [2]. However, as the theoretical treatment of such many-body atomic physics problems is quite challenging and experimental data is sparse, the development of a semi-empirical cross section formula might be a pragmatic provisional solution for the time being.

Here I report on a new semi-empirical formula for total electron loss cross section of many-electron ions penetrating through matter. The equation is based on a treatment of the energy dependence of total electron loss proposed by Shevelko et al. [3] and a scaling formula for the dependence on target Z of the projectile electron loss developed by DuBois et al. [4]. In Fig. 1 all experimental data considered in this study is presented (top) together with the prediction of the new electron loss formula (bottom). Note that for the latter the energy axis was converted to a reduced energy $u = (\beta/\alpha)^2 / (I_p/Ry)$ with β being the collision velocity, α being the fine strucutre constant, I_p denoting the ionization potential of projectile ion and Ry denoting the Rydberg energy. One finds that most of the experimental data lies within a ± 30 % range around the formula and almost all data are matched within less than a factor of 2. This is remarkable taking into account that the projectiles reach from Fe^{4+} to U^{86+} and the collision energies from less than 1 MeV/u to roughly 1 GeV/u, also noting that the targets considered reach from hydrogen to gold. Further work is needed to evaluate the range of validity of the new electron loss formula and to optimize, i. e. reduce, the number of free parameters.

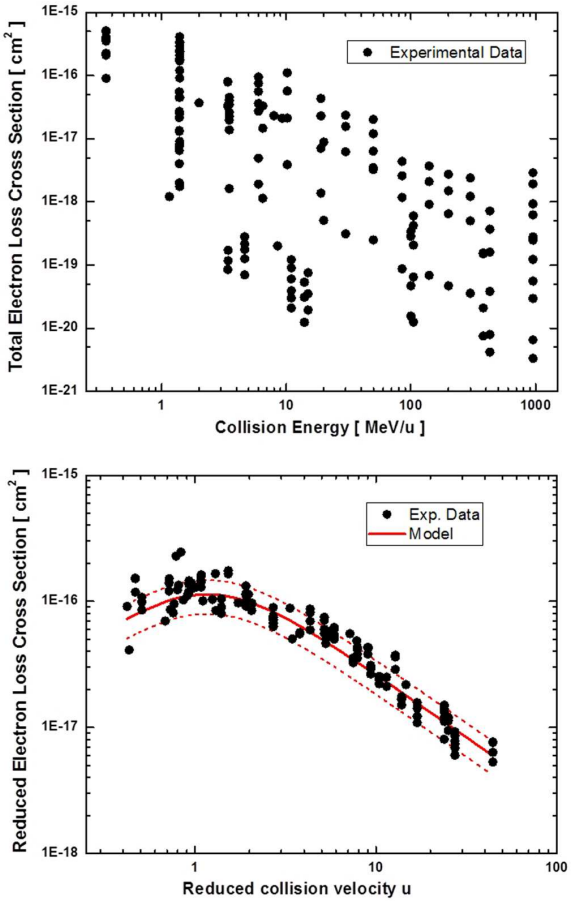

Figure 1: Top: Overview of all experimental total electron loss cross section considered in the present study. Bottom: Semi-empirical formula for total electron loss of many-electron ions penetrating through matter in comparison to the experimental data.

References

[1] FAIR - Baseline Technical Report (2006)

[2] V. P. Shevelko et al., *Electron Loss and Capture Processes in Collisions of Heavy Many-Electron Ions with Neutral Atoms*, in: Atomic Processes in Basic and Applied Physics **68**, 125, Springer (2012)

[3] V. P. Shevelko et al., NIM B **269**, 1455 (2011)

[4] R. D. DuBois., Phys. Rev. A **84**, 022702 (2011)

*This report is also part of the GSI Scientific Report 2016 / GSI Report 2017-1.

A continuous data logger for the ESR current transformer

S. Sanjari[1], *Yu. A. Litvinov*[1], *H. Reeg*[1], *and Th. Stöhlker*[1,2]
[1]GSI Helmholtzzentrum Darmstadt; [2]Helmholtz-Institut Jena

In this work we introduce a new read-out electronic for the existing DCCT current transformer of the ESR.

Motivation

As long as coherent effects are not dominant in the beam, which is the case for beams of very high intensity, the integral power within Schottky bands are proportional to the ion beam current and hence the number of particles [1]. So a measured absolute value of current intensity is needed so that the integral power of Schottky spectra can be normalized to it. To this end usually a DC current transformer (DCCT) or alternatively a cryogenic current comparator (CCC) can be used.

This approach has two advantages: in the absense of a CCC, sensitivities out of reach to the DCCT can be realized by properly designed resonant Schottky detectors. Furthermore using time resolved Fourier analysis it is possible to quickly follow the beam intensity within the same injection cycle. This method has been tested at ESR storage ring at GSI using the resonant Schottky pickup [2] and the ESR's DC Current Transformer [3]. Results are available in [4].

The Hardware

The GSI DCCT electronics provides an analog signal, which after passing through a differential to serial converter in GSI's operation area BG2.009, reaches the main control room. Additionally a second output was connected to a circuit based on a voltage to frequency converter, in order to make the signals available in the atomic physics data acquisition system over a 50 ohm transfer line [5]. A third low impedance output was left unused. The circuit described here has been designed to sample this output, after adaptation, using a 12-bit serial successive approximation analog to digital converter MCP3208. As the main controller, a single board computer (Raspberry Pi) running Linux operating system has been utilized. The circuit is placed directly underneath the DCCT in the ESR in order to keep a short analog signal path. The digitized values are transferred over the network.

The Software

The code is written entirely in Python using a client/server structure [6]. The circuit acts as a message queue (ZeroMQ) server in the publisher/subscriber mode and broadcasts the value of the DCCT current to any subscriber available on the network. The sampling rate is set to 5 sps. Any number of clients can subscribe to the publishing server, either using the command line or the GUI and can run on any number of computers inside the network. The command line interface can be set to write out files of certain length, thereby allowing practically unlimited and continuous monitoring of ESR current over weeks of beam time. While providing a unique time stamp for every recorded sample, the server updates its clock regularly using an internet time server. The resulting data can be easily plotted or processed offline together with Schottky spectra. During the beam time of 2016, this device was successfully tested, where data were stored directly on GSI's central computing cluster.

Future extensions

The electronics of the DCCT allow for certain amplification ranges. Although already implemented in the software, currently the ranges are set manually. In order to get the ranges automatically form the control system, an optically decoupled module has been designed in order to separate ground loops from that of the ESR. The test of this module is planned for a future beam time. The proper connection to the to the FAIR Control System still needs to be implemented. A similar design may be planned for experimental purposes in future storage rings of FAIR.

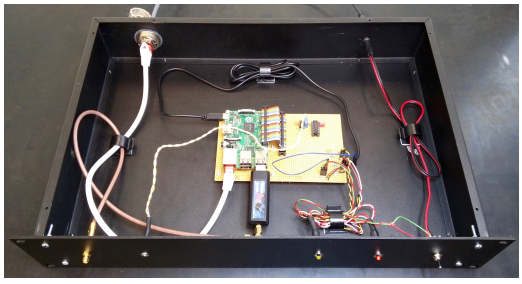

Figure 1: The new readout electronic for the ESR DCCT

References

[1] S. Chattopadhyay, CERN-1984-011 (1984)
[2] S. Sanjari et. al., Phys. Scr. (2013) 014088
[3] H. Reeg, N. Schneider, Proc. DIPAC Grenoble (2001) PS08
[4] S. Sanjari, GSI Scientific Report (2012) PNI-ACC-03
[5] R. Steiner, private communication (2016)
[6] S. Sanjari, *https://github.com/xaratustrah/rasdaq* (2016)

S-EBIT facility: Status Report*

S. Trotsenko[1,2], N. Bauer[3], A. Gumberidze[3,4], G. Vorobjev[3], D. Racano[3], C. Kozhuharov[3], F. Herfurth[3], R. Schuch[5], and Th. Stöhlker[1,2,3]

[1]Friedrich-Schiller-Universität Jena, D-07743 Jena, Germany; [2]Helmholtz-Institut Jena, D-07743 Jena, Germany; [3]GSI Helmholtzzentrum für Schwerionenforschung, D-64291 Darmstadt, Germany; [4]ExtreMe Matter Institute EMMI, GSI, D-64291 Darmstadt, Germany; [5]Department of Physics, Stockholm University, SE-10691 Stockholm, Sweden

S-EBIT [1] facility currently installed at GSI shall facilitate research and development works for SPARC experiments at FAIR. This accelerator-independent source of HCI shall provide ions necessary for R&D of HITRAP [2] experimental stations and serve as a standalone device for research and R&D activities (e.g. development of x-ray spectrometers, calorimeter detectors, x-ray optics etc. [3]). Furthermore, the combination of S-EBIT with the available laser infrastructure e.g. JETI200 will be a unique platform for the study of highly charged ions subject to intense laser radiation [4]. During the FAIR construction related shutdown period of the GSI accelerator complex, when little to no beam time can be provided, such an accelerator-independent source of ions is of particular importance (Fig. 1).

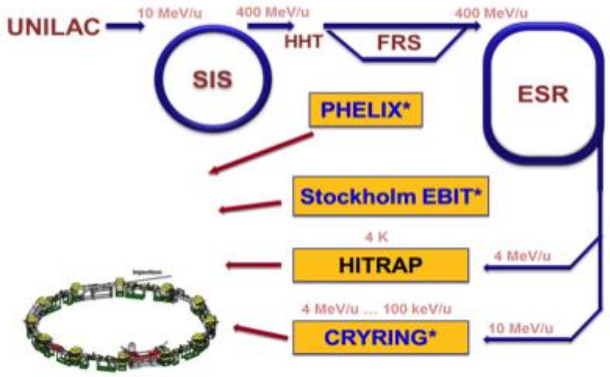

Figure 1: *Schematic of interrelated experimental arrangements (for description compare text).*

The EBIT-I of the S-EBIT facility [5] has been succsessfully commissioned at the Helmholtz Institute Jena/GSI and can be stably operated. This EBIT is equipped with a few windows providing line of sight to the middle drift tube (trap) region at an angle of 90◦ with respect to the electron beam axis. On one of the windows a gas injection is realized in a colimated differentially pumped drift region, which is providing an atomic beam that is pointed directly on the electron beam. A buffer volume of the gas injection can be filled by a leak valve and/or a pulsed valve allowing for mixing a cooling gas. The trap pressure during the continuous gas injection is lower than 10^{-10} mbar. Another port, equiped with a Be-window, was used in ordert to characterize the EBIT by recording spectra of the x-rays emitted from interactions between the ions and electrons inside the trap region. A Si-pin diode detector (Amptek XR-100CR) with a measured resolution of about 300 eV at 10 keV was used for these measurements.

A typical x-ray spectrum with Xe and Ar injection is shown in figure 2 with the relevant peaks labeled. The spectrum was taken with the electron beam of a 10kV energy (and a current of 30 mA), which was compressed by 1 Tesla magnetic field provided by the superconducting coils. The Ar-K and Xe-L peaks can be seen along with the peaks due to radiative recombination (RR) into the xenon L-, M- etc shells.

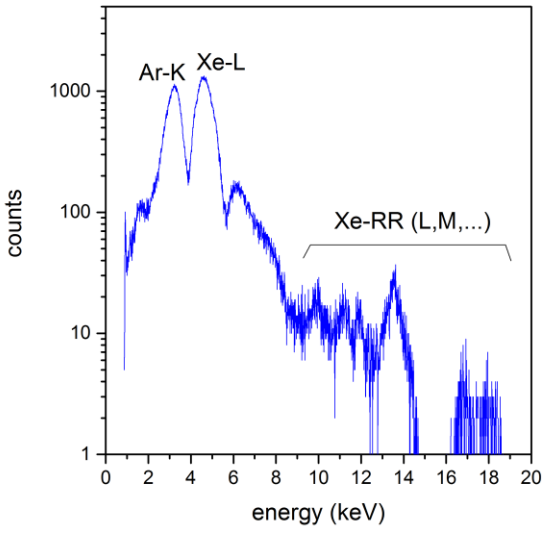

Figure 2: *X-ray spectrum of Xe and Ar from the EBIT-I (for description compare text).*

Currently a fast multi-parameter data acquisition system is being prepared for the future x-ray measurements that will combine the EBIT with a dedicated Si(Li) detector as well as with novel techniques based on combination of crystal- and microcalorimeter-spectroscopy up to the hard x-ray regime [3]. Moreover, a time-resolved x-ray measurements is being prepared, which is necessary for a characterization of the charge breeding process. This along with the time of flight (and/or magnet scan) for the evaluation of the charge state distribution of extracted ions is also vital for the experiments where the EBIT can serve as a source of ions, e.g. HITRAP, CRYRING.

[1] R. Schuch et al., JINST5, C12018 (2010)
[2] F. Herfurth et al., Phys. Scr. T166, 014065 (2015)
[3] D. Hengstler et al., Phys. Scr. T166, 014054 (2015)
[4] M. Vogel et al., Nucl. Instr. Meth. B 285, 65 (2012)
[5] S. Trotsenko et al., HIJ/GSI Sci. Rep. 2015 (2016)

**Part of the GSI Scientific Report 2016/* /GSI Report 2017-1

Status of the HILITE Penning trap experiment*

S. Ringleb[1], *N. Stallkamp*[1,2], *M. Vogel*[2,3], *S. Kumar*[4], *M. Kiffer*[1], *W. Quint*[5], *G. Paulus*[1,3], *and Th. Stöhlker*[1,2,3]

[1]Universität Jena; [2]GSI, Darmstadt; [3]Helmholtz-Institut Jena; [4]Inter-University Accelerator Centre, New Delhi; [5]Ruprecht Karls-Universität Heidelberg

The HILITE Penning trap is an ion trap developed to capture, detect and confine ions in order provide well-defined ion-targets for laser-ion interaction studies. Therefore we apply several techniques for ion detection, ion selection and ion confinement.[1]
We have implemented the SWIFT technique to be able to form ion targets of only one ion species. This technique has been tested at the similar ion trap ARTEMIS. Based on the results of this test we have adapted our electronic circuits for noise-reduction such that we enable fast switching of the electrodes with time constants of the order of nanoseconds. These modified filters have been built and connected to the trap electrodes.

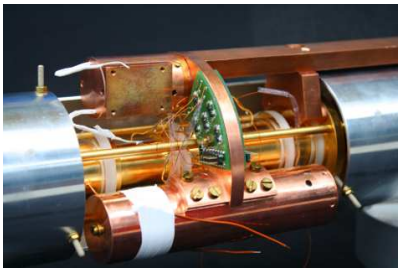

Figure 1: Picture of the assembled Penning trap - electrodes inside inner tube with applied filter boards and resonators.

For non-destructive ion detection we use resonant amplification of image currents induced in the trap electrodes by ion oscillations. To improve the sensitivity of the detection of stored ions inside the Penning trap we have built two resonators and tested them at cryogenic temperatures. To enlarge the ion spectrum, that can be detected by the resonant circuit, we will employ a varactor-diode for each resonator. We have tested the varactor-diode concerning its behaviour in the magnetic field at temperatures down to 4 K. Based on the results we have built dedicated varactor diode boards, which also support a wide tunability even at low temperatures and high magnetic fields.

In order to achieve long ion storage times the design residual gas pressure is better than 10^{-12} mbar. To compromise the open-endcap design of the Penning trap with a sufficient vacuum in the interaction region, a set of baffles at cryogenic temperatures is applied on each side of the trap-electrodes. As these baffles will also be used as a pulsed drift tube for ion deceleration, they are electrically isolated from the inner shield by ceramic spacers, which also support good thermal conductivity.

Figure 2: Picture of the assembled baffle system for vacuum improvement and ion deceleration.

As an ion source for the first commissioning experiments we have set up an EBIT and verified its functionality. We have produced ions inside the EBIT and have measured the extraction with a faraday cup. The next steps will be the connection of the EBIT with our ion trap to capture ions produced inside the EBIT and check the functionality of the measurement-principles of the ion trap.

Figure 3: Experimental stand with equipped device rack.

Our recent results and the status of our experiment have been presented at the PSAS in Jerusalem, at the SPARC workshop in Krakow and at the MML workshop in Hamburg.

References

[1] S. Ringleb, M. Vogel, S. Kumar, W. Quint, G. Paulus, Th. Stöhlker, Journal of Physics Conference Series **635** (2015) 092124

* also part of the GSI Scientific Report 2016 / GSI Report 2017-1

Theory

A Systematic Approach to Numerical Dispersion in Maxwell Solvers

David Schinkel[1], *Alexander Blinne*[1], *Stephan Kuschel*[1,2], *Nina Elkina*[1], *Sergey G. Rykovanov*[1], *and Matt Zepf*[1,3]

[1]Helmholtz Institute Jena, Fröbelstieg 3, 07743 Jena, Germany; [2]Institute for Optics- and Quantumelectronics, Friedrich Schiller University Jena, Max-Wien-Platz 1, 07743 Jena, Germany; [3]Department of Physics and Astronomy, Queen's University Belfast, Belfast, BT7 1NN, UK

The numerical approach to Particle-In-Cell simulations may introduce a number of unphysical artifacts. Different schemes exist that remedy some of those problems, but may introduce other problems of their own. A systematic approach to one class of modified schemes is presented here. We show that it is possible to optimize the free parameters of an extended stencil such that the deviation from the physical dispersion relation is minimized.

The finite-difference time-domain (FDTD) method is a well established method for solving the time evolution of Maxwell's equations and especially a scheme introduced by Yee [1] is frequently used in plasma simulations. Unfortunately the scheme introduces numerical dispersion, and therefore phase and group velocities deviate from the correct value. As a result, the solution to Maxwell's equations leads to unphysical predictions such as Cherenkov radiation emitted by a relativistic electron beam propagating in a vacuum or plasma [2].

Improved solvers generally modify the spatial derivative operator in the Maxwell-Faraday equation by increasing the computational stencil, while keeping the staggered Yee-type grid for electric and magnetic fields [3, 4]. The Maxwell-Faraday and Maxwell-Ampere equations take the form

$$\frac{1}{c}\partial_t \vec{B} = -\vec{\nabla}^* \times \vec{E}$$
$$\frac{1}{c}\partial_t \vec{E} = \vec{\nabla} \times \vec{B} - \frac{4\pi}{c}\vec{j}$$

where $\vec{\nabla}$ denotes the stencil that is used in the original Yee scheme while $\vec{\nabla}^*$ denotes the extended stencil used in the Maxwell-Faraday equation. These modified solvers can be characterized by different sets of coefficients, leading to different dispersion properties.

In order to ensure the conservation of $\vec{\nabla} \cdot \vec{B} = 0$ we demand

$$0 = \partial_t \vec{\nabla} \cdot \vec{B} \propto \vec{\nabla} \cdot \left(\vec{\nabla}^* \times \vec{E} \right) ,$$

which translates into demanding the symmetry of second derivatives for the different stencils

$$\nabla_i \nabla_j^* = \nabla_j \nabla_i^* \qquad i \neq j \, .$$

This yields additional consistency constraints for the coefficients that define the extended stencil $\vec{\nabla}^*$.

We introduce a norm function

$$|\omega_G| = \int_{k_x} \mathrm{d}k_x \int_{k_y} \mathrm{d}k_y \int_{k_z} \mathrm{d}k_z \, w \cdot (\omega_G - c|\vec{k}|)^2$$

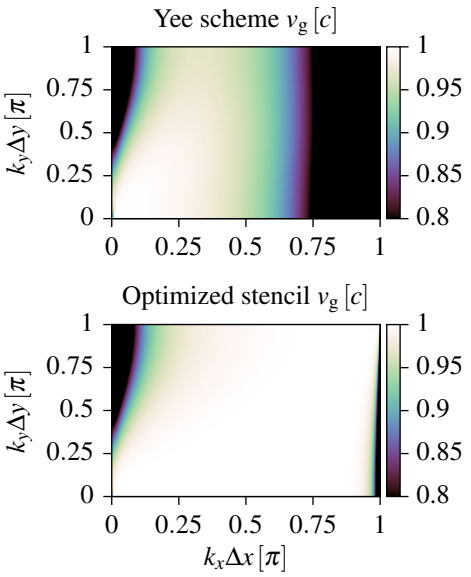

Figure 1: Numerical group velocities of the Yee scheme [4] (upper panel) and a numerically optimized stencil (lower panel) on a $\frac{\Delta y}{\Delta x} = 10$ grid.

to rewrite the choice of coefficients into a minimization problem. The numerical dispersion relation ω_G enters here as a function of the coefficients, while a weight function w might be introduced to put emphasis on a region of wave vector space which is of special interest for a given setup.

When the minimization problem is solved for $w = 1$, we find a set of coefficients which leads to considerably less artificial dispersion as compared to schemes with manually set coefficients available in the literature, see Fig. 1. We show that, depending on a specific problem at hand (e.g. electron beam propagation in plasma, high-order harmonic generation from plasma surfaces, etc), the norm function can be chosen accordingly, for example, to minimize the numerical dispersion in a certain given propagation direction.

References

[1] K. S. Yee, IEEE Trans. Antennas Propag. **14**, 302–307 (1966)

[2] B. B. Godfrey, Journal of Computational Physics **15**, 504 – 521 (1974)

[3] A. Pukhov., Journal of Plasma Physics **61**, 425–433 (1999)

[4] R. Lehe, A. Lifschitz, C. Thaury, V. Malka, and X. Davoine, Phys. Rev. ST Accel. Beams **16**, 021301 (2013)

Spectral caustics for optimization of nonlinear Compton sources *

V. Yu. Kharin[†1], *S. G. Rykovanov*[1], *and D. Seipt*[2,3]

[1]Helmholtz Institute Jena, Germany; [2]Lancaster University, Physics Department, Lancaster, UK; [3]Cockcroft Institute, Daresbury Laboratory, Warrington, UK

One of the schemes for obtaining bright tunable X- and γ-ray sources is the scattering of the intense laser light on the accelerated electron beams. When the electron beam has a Lorentz factor γ, the scattered light is roughly of frequency $4\gamma^2\omega_L$, where ω_L is the laser frequency. The quantum nature of light leads to the corrections due to recoil and spin effects. If the laser pulse is relativistically intense, the scattered light will also gain harmonics. And every harmonic will be broadened and Doppler down-shifted due to ponderomotive effects. This whole process is called nonlinear Compton scattering.

The nonlinear Compton scattering process by the virtue of Furry picture can be represented as a first-order perturbation theory process. The transition occurs between the two dressed states. In the case of plane electromagnetic pulsed wave these are the Volkov solutions of the Dirac equation. General analysis of the scattering amplitudes is a complex task even for this simple setting. There are two problems to investigate: direct and inverse. Direct one consists in prediction of the scattered specra for a given an incident pulse. It is usually solved either numerically, or with some approximations (such as contant crossed-field, or stationary phase). Some closed-form analytic solutions are known for specific pulse shapes [1]. Inverse problem is tailoring the laser pulse in order to obtain the given spectra of the scattered light. This problem is not so well-studied. The usual approach here is brute-force numerics.

Our new method of dealing with both of these problems consists in application of the techniques known for a long time in the catastrophe optics [2]. For sufficiently long incident pulses, the scattering amplitude may be decomposed into the set of harmonics. Each of them is affected by the ponderomotive broadening and the recoil. The precise structure of the integrals defining the harmonic shape is similar to the ones describing interference pattens. The decomposition is valid for arbitrary scattering angle and scattered frequency. On the language of the catastrophe theory it means, that the system naturally has 2 control parameters (the polar angle does not contribute to stationary phase point position). The map being studied is the projection $\pi : (\omega, \theta, \varphi) \mapsto (\omega, \theta)$, where ω is the frequency of the scattered photon, θ is the azimuthal angle, φ determines the point of the laser pulse ($\varphi = t - z$ for the pulse propagating in z-direction). The restriction of some point φ being stationary phase point defines the ray surface in $(\omega, \theta, \varphi)$.

Projection of the ray surface on the space of control parameters may have singular points (i.e. those, where the projection derivative matrix is degenerate). According to the catastrophe theory, for the 2-dimensional spaces there are only 2 types of stable singularities (caustics) which may arise: folds and cusps.

From the physical point of view, the caustics result in the bright spots in the scattered spectra (See Fig. 1, yellow curve). The spectrum in the vicinity of fold is described by Airy function, and cusp spectrum corresponds to the Pearcey pattern [2].

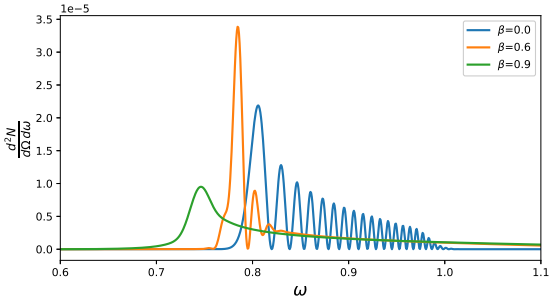

Figure 1: On-axis scattered spectra in electron rest frame for various values of the chirp. Instantaneous frequency is $\omega_L = 1 + \beta\varphi/\tau$. Laser pulse envelope is $a_0 \cos^2(\pi\varphi/\tau)$; $a_0 = 0.7$, $\tau = 400\pi$. Circular polarization.

The analysis of the ray surfaces can be conducted in a much more straightforward manner, than a full-scale calculation. Therefore, it provides a nice tool of qualitative analysis of the nonlinear Compton scattering. It allows qualitative predictions on the solutions of both direct and inverse scattering problems, and complements the full-scale numerics. The inverse scattering problem has particular importance in the design of narrowband tunable Compton sources. Hence the stability of the catastrophe theory under small variations of initial conditions is property which looks very attractive for possible applications.

References

[1] D. Seipt, V. Kharin, S. Rykovanov, A. Surzhykov, and S. Fritzsche "Analytical results for nonlinear Compton scattering in short intense laser pulses", J. Plasma Phys., **82**, 2, 655820203 (2016)

[2] Nye, J. F., "Natural Focusing and Fine Structure of Light: Caustics and Wave Dislocations", CRC Press, 1999

[3] V.Yu. Kharin, et al, *submitted*

* Work supported by the Helmholtz Association (Helmholtz Young Investigators group VH-NG-1037).

† v.kharin@gsi.de

γ-ray Generation from Plasma-based Resonant Wiggler*

B. Lei[#], *J. Wang, S.G. Rykovanov*
Helmholtz-Institut Jena, 07743 Jena, Germany

Abstract

We propose a concept to generate γ-rays in a plasma-channel undulator [1], in which the betatron oscillations are resonant with the laser pulse centroid oscillations. The frequency of latter is proportional to the inverse of Rayleigh length of the laser pulse. As a result, the betatron amplitude is largely increased in the early interaction section, as seen in Figure 1. It was demonstrated analytically and with the help of numerical simulations that the amplitude of electron oscillations is fast increased in a short early section, and then it can keep a semi-steady pattern for a long distance due to the energy gain. Thus, wide-bandwidth, flexible polarization γ-ray radiation can be obtained.

Wiggler field generation

In the case when a short laser pulse enters a plasma channel off-axis or under an angle, the centroid oscillates with the period of Rayleigh length. The polarization of laser centroid oscillations could be well controlled by carefully choosing the initial injection parameters, e.g. injection position and angle.

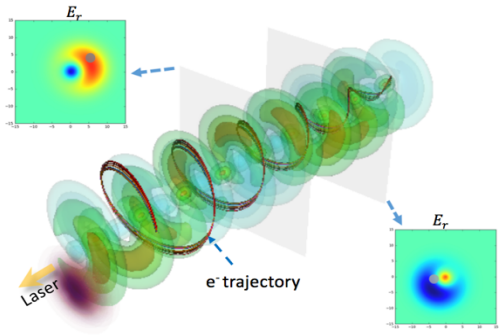

Figure 1: Resonant betatron oscillation of electron bunch in plasma parabolic channel.

As a result, the ponderomotively driven laser plasma wakefield oscillates following the laser pulse and generates a wiggler field [1].

Electron resonant oscillation

By injecting a relativistic electron ($\gamma_0 \gg 1$) into such a wakefield, dynamics of the electron is determined by time-dependent weakly damped harmonic oscillator.

If we initially make such a condition, $\Omega = \Omega_\beta\sqrt{-\sin\xi}$, the electron is resonant during the early section as seen in Figure 2(a). Here, we have introduced the betatron frequency $\Omega_\beta = (4a_0^2C/\gamma_0 r_m^2)^{1/2}$. In case the electron keeps moving in resonance with the laser pulse centroid oscillations, it will eventually get out of the focusing structure and get lost. However, after further acceleration, the energy gain breaks the resonance, and as a result, a semi-steady pattern of oscillation is generated, as seen in Figure 2(a).

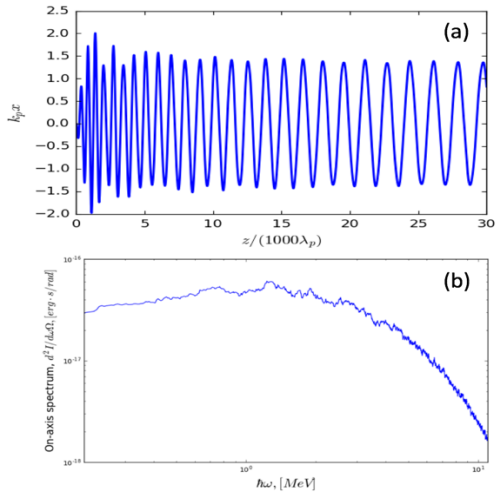

Figure 2: (a) Trajectory of an electron in a resonant plasma wakefield; (b) On-axis radiation spectrum for one electron undergoing the resonant oscillation with parameters: $\xi_0 = -1.5\pi/2, \gamma_0 = 1800, a_0 = 0.9$. The oscillation strength of steady oscillation is $K_R \simeq 40$.

γ-ray radiation

Since the oscillation strength, K_R could be much larger than unity in this resonant configuration, a series of harmonics $\omega_n \simeq n2\overline{\gamma_z}^2\Omega$ could be emitted within a half-angle $\psi = K_R/\gamma$ [2], where $\overline{\gamma_z} = \gamma(1 + K_R^2/2)^{-1/2}$ is the average longitudinal Lorentz factor, and n is the harmonic number. Thus, the radiation spectrum becomes synchrotron-like and can reach gamma-ray region.

References

[1] S. G. Rykovanov, et al, Plasma Undulator Based on Laser Excitation of Wakefields in a Plasma Channel, Physical Review Letters, 114, 145003 (2015)

[2] S. Kiselev, et al, X-ray Generation in Strongly Nonlinear Plasma Waves, Phys. Rev. Lett. **93**, 135004 (2014)

* Work supported by Helmholtz Association (Young Investigator's Group No. VH-NG-103)
# b.lei@gsi.de

Plasma channel undulator excited by high-order laser modes*

Jingwei Wang[#], *and Sergey Rykovanov*
Helmholtz Institute Jena, Jena 07743, German

Principles of the plasma undulator

Laser pulses with transverse profile given by Hermite-Gaussian (HG) modes will propagate inside the channel without changing their transverse shape given that their spot size is matched to the channel radius. Plasma undulator can be generated by propagating a mixture of different HG laser modes in a matched plasma channel. An oscillatory behaviour of intensity envelope appears when the modes with the same polarization co-propagate in the plasma channel, since the phase velocities for different modes are dependent on the mode numbers. For example, three y-polarized HG modes, |0, 0>, |0, 1>, and |1, 0>, propagate in a matched plasma channel. In both the (x, z) plane and the (y, z) plane, the profile of the total intensity oscillates with a wavelength proportional to the Rayleigh length Z_R of the pulse. The wakefield generated by the modes will also oscillate while propagating in the channel, which provides an additional control of the focusing field. The focusing fields of the induced plasma wakefield serve as an undulator. Electrons injected into the wakefield will experience undulator oscillations and emit bright radiation.

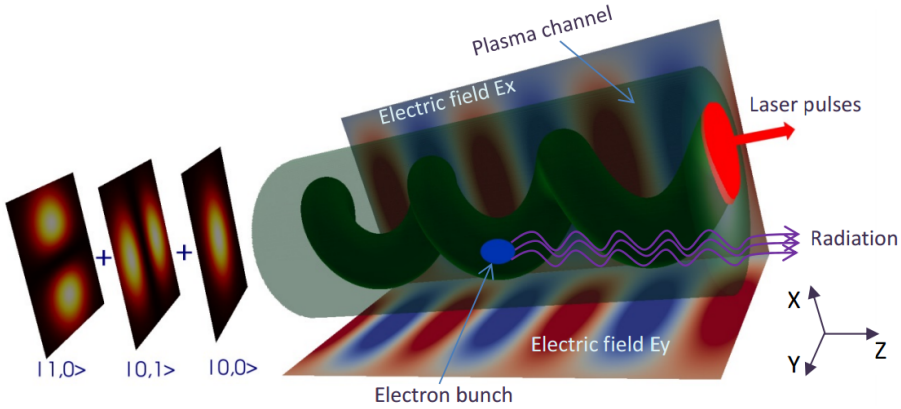

Figure 1: Schematic of the plasma channel undulator.

Electron dynamics and radiation

Energetic electrons injected in such a plasma undulator will experience both betatron oscillations and undulator oscillations. By choosing appropriate laser intensities, the focusing field disappears because the sum of the intensities of the modes keeps constant near the axis. Electrons injected into such a particular wakefield will oscillate only with the undulator frequency, and the undulator strength parameter is independent of the electron transverse positions, analogous to a magnetic undulator. To extend the length of the undulator, the phase of the electrons in the wakefield is locked by longitudinally tapering the plasma channel. One can see that the beam keeps a constant radius while oscillating in the undulator with a wavelength $2\pi Z_R$ for about 20 undulator periods. The spectrum bandwidth is as narrow as 6%, which is very close to the theoretical bandwidth. Higher frequency radiation can be obtained by using higher order mode mixed with the fundamental mode.

The polarization of the radiation can be controlled by changing the phase difference of the modes. The beam loading limit indicates that the tolerated beam charge can lead to currents as high as 0.3 kA, theoretically approaching the kA level. Such a plasma undulator, together with a laser plasma accelerator, may open the way to realize an extremely compact FEL.

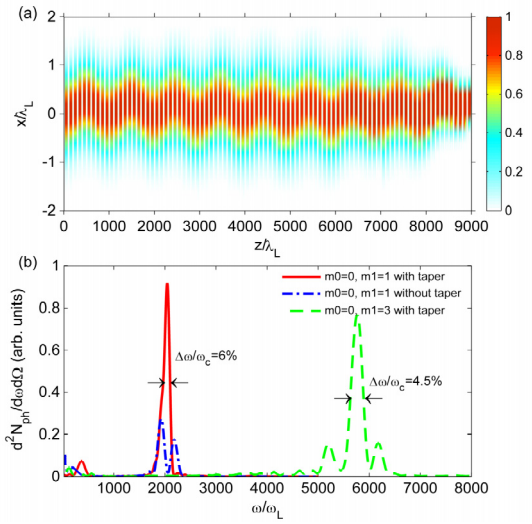

Figure 2: Trajectory and radiation spectrum of the electron beam propagating through the plasma undulator.

* Work supported by Helmholtz Association (Young Investigator's Group No. VH-NG-103)
# J.Wang@gsi.de

References

[1] J. Wang *et al.* "Plasma channel undulator excited by high-order laser modes", submitted.

Pair production in bichromatic fields

Alexander Blinne and Holger Gies
Helmholtz Institut Jena, Fröbelstieg 3, D-07743 Jena, Germany
Theoretisch-Physikalisches Institut, FSU Jena, Max-Wien-Platz 1, D-07743 Jena, Germany

Due to the required field strengths, it remains a challenge to observe pure Schwinger pair production in a laboratory setup. There is a large regime between Schwinger pair production and multiphoton pair production, where both effects show a complex interplay [1]. When the field strength is insufficient to observe Schwinger pair production in a slowly varying field, the pair production probability can be increased by adding a weaker, but quickly varying field. This is called the dynamically assisted Schwinger mechanism [2]. Specifically in the presence of two dominant frequency scales, one expects bichromatic pair production. Here, we present transverse particle production as a new feature which we have identified in bichromatic pair production.

Using the modified quantum kinetic equation [1] we are able to compute the pair production spectra for spatially homogeneous electric fields with arbitrary temporal variation. Our Ansatz for the electric field results from the superposition of two oscillating fields under an sech^2 envelope,

$$E_x(t) = \frac{E_{\mathrm{cr.}}}{\cosh^2\left(\frac{t}{\tau}\right)} \left(\varepsilon_0 \cos(\Omega t) + \varepsilon_1 \cos(n\Omega t + \varphi)\right) . \tag{1}$$

Both the low and high frequency component are oscillating fields and correspond to linear polarization.The prefactors $\varepsilon_{0/1}$ correspond to the dimensionless field-strengths of both contributions. The spectra created by linearly polarized purely electric fields are cylindrically symmetric, thus $p_y \mathrel{\hat{=}} |\vec{p}_\perp|$ and $p_x = p_\parallel$.

After conducting a number of parameter scans we found, for some choices of the parameters, that pairs would be produced in bunches with a transverse momentum. In order to quantify this we assume a circular detector surface which would be seen from the interaction region as a circular disc with a diameter of 60°. This would collect all particles with momenta that are within 30° of the axis pointing to the center of the disc. Using spherical coordinates, we define

$$f(p) := p^2 \int_0^{\frac{\pi}{6}} \mathrm{d}\vartheta \sin(\vartheta) \int_0^{2\pi} \mathrm{d}\phi\, f(p,\vartheta,\phi)$$
$$\mathcal{N}_{\mathrm{det}} := \frac{1}{(2\pi)^3} \int \mathrm{d}p\, f(p) .$$

As an example we present results obtained from a two-dimensional parameter scan for $\phi = 0, \ldots, 2\pi$ and $\Omega = 0.15, \ldots, 0.25m$ and a fixed $n = 5$. Within this dataset, we can search for parameters which optimize various variables. Choosing parameters such that the detector yield is maximized leads to $\phi = \pi$ and $\Omega = 0.238m$ which produces the spectrum shown in Fig. 1.

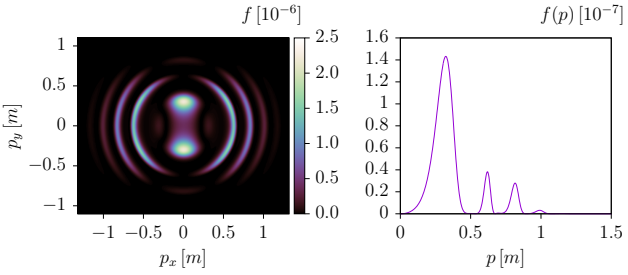

Figure 1: Full spectrum and detector spectrum for maximum $\mathcal{N}_{\mathrm{det}}$ with $\phi = \pi$ and $\Omega = 0.238m$.

A brilliant electron bunch can be defined as having a large mean momentum as compared to its momentum spread

$$\overline{p} := \frac{\int \mathrm{d}p\, p\, f(p)}{\int \mathrm{d}p\, f(p)} \qquad \sigma_p^2 := \frac{\int (p-\overline{p})^2 f(p)}{\int \mathrm{d}p\, f(p)} .$$

Searching, for example, for parameters that produce a brilliant electron bunch, we can maximize $\frac{\overline{p}}{\sigma_p} \cdot \frac{\mathcal{N}_{\mathrm{det}}}{\mathcal{N}}$. This leads to $\phi = 0$ and $\Omega = 0.202m$ (see Fig. 2).

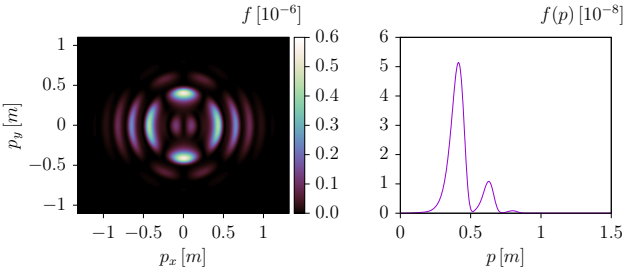

Figure 2: Full spectrum and detector spectrum for maximum $\frac{\overline{p}}{\sigma_p} \cdot \frac{\mathcal{N}_{\mathrm{det}}}{\mathcal{N}}$ with $\phi = 0$ and $\Omega = 0.202m$.

In summary, we have established transverse pair production as a new characteristic of the quantum interference nature of pair production by bichromatic fields.

References

[1] A. Blinne, "Electron Positron Pair Production in Strong Electric Fields," PhD Thesis (2016), arXiv:1701.00743.

[2] R. Schutzhold, H. Gies and G. Dunne, "Dynamically assisted Schwinger mechanism," Phys. Rev. Lett. **101** (2008) 130404 doi:10.1103/PhysRevLett.101.130404, arXiv:0807.0754.

On the effect of time-dependent inhomogeneous magnetic fields in electron-positron pair production*

C. Kohlfürst† [1,2] *and R. Alkofer*[3]

[1]HI-Jena, Germany; [2]University of Jena, Germany; [3]NAWI Graz, University of Graz, Austria

Electron-positron pair production attracted renewed attention over the last decade [1], because upcoming laser facilities, *e.g.*, ELI and XFEL are expected to deepen our understanding of matter creation [2].

In the special case of constant crossed and homogeneous fields the Lorentz invariant $\mathcal{F} = \frac{1}{2}\left(\mathbf{E}^2 - \mathbf{B}^2\right)$ determines the particle production rate [3]. Electric and magnetic fields appear in equal magnitude in the quantity $\mathcal{F}$, but magnetic fields are usually ignored in theoretical investigations of time-dependent set-ups. This may be motivated by the fact that for perfect settings the magnetic field vanishes in the vicinity of two colliding laser beams. However, especially in view of a possible experimental verification, such an approximation could be unsatisfactory.

We devoted a recent work [4] to investigate the effect of inhomogeneous magnetic fields in particle production using a phase-space approach (DHW formalism). In this work, we chose a vector potential of the form

$$\boldsymbol{A}(z,t) = \varepsilon\,\tau \exp\left(-\frac{z^2}{2\lambda^2}\right) \left(\tanh\left(\frac{t+\tau}{\tau}\right) - \tanh\left(\frac{t-\tau}{\tau}\right)\right) \boldsymbol{e}_x, \quad (1)$$

with field strength ε, pulse length τ and spatial extent λ. Moreover, we introduced a "modified effective field energy"

$$\mathcal{E}\left(\mathbf{E},\mathbf{B}\right) = \int dz\, dt\, \tilde{E}\left(z,t\right)^2\, \Theta\left(\tilde{E}\left(z,t\right)^2\right), \quad (2)$$

with the Heaviside function $\Theta\left(x\right)$ and the "effective field amplitude" $\tilde{E}\left(z,t\right)^2 = \mathbf{E}\left(z,t\right)^2 - \mathbf{B}\left(z,t\right)^2$, compare with Ref. [3].

In the limit $\lambda \gg \tau$, the electric field can be considered as quasi-homogeneous and the magnetic field becomes negligible. Generally, however, spatial restrictions on the electric field and the effect of a magnetic field growing in strength for decreasing λ have to be taken into account to compute the particle production rate. Analyzing $\mathcal{E}\left(E,B\right)$ one observes a faster than linear decrease with decreasing λ. This is in qualitative agreement with the particle yield N, as illustrated in Fig. 1.

For the case $\boldsymbol{E} = -\dot{\boldsymbol{A}}$ and $\boldsymbol{B} = 0$ simply calculating the corresponding effective field energy ($\mathcal{E}\left(E,0\right)$) is not sufficient, because the homogeneous Maxwell equations are not fulfilled. Hence, we suggested to add the missing part of the effective field energy to the electric field energy.

In this way, the increase in the particle yield in Fig. 1 can be understood assuming that a magnetic field hinders matter creation. Ignoring contributions from $\boldsymbol{\nabla} \times \boldsymbol{A}$ therefore leads to an overestimation of the effective field energy and consequently of the total particle number. The sharp drop off on the left side of Fig. 1 is connected to the fact, that for $\lambda \to 0$ the energy stored in the background field is not sufficient anymore to overcome the particle rest mass.

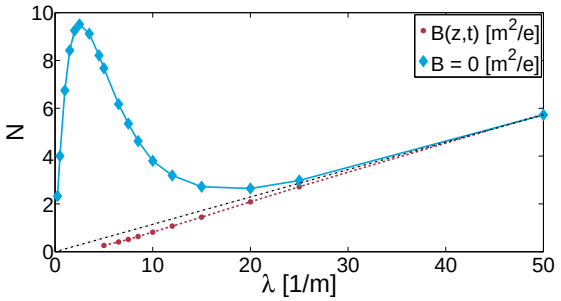

Figure 1: Particle yield for a configuration with $\tau = 10/m$ and $e\varepsilon = 0.707\, m^2$. In case of a sizable magnetic field the calculation for $B = 0$ (blue solid line) leads to an overestimation compared to the correct result (dashed red line). Extrapolated homogeneous result: dashed black line.

We have verified in a quantitative manner that in the case of spatially strongly localized fields the results can be explained assuming that pair production is only possible in regions where the electric field exceeds the magnetic field. In this parameter region the correct treatment of the magnetic field is of utter importance.

References

[1] T. Heinzl and A. Ilderton, Eur. Phys. J. D **55** (2009) 359;

[2] F. Sauter, Z. Phys. **69**, 742 (1931); W. Heisenberg and H. Euler, Z. Phys. **98**, 714 (1936); J. S. Schwinger, Phys. Rev. **82**, 664 (1951);

[3] G. V. Dunne, In *Shifman, M. (ed.) et al.: From fields to strings, vol. 1* 445-522;

[4] C. Kohlfürst and R. Alkofer, Phys. Lett. B **756** (2016) 371;

*Work supported by HI Jena in cooperation with Friedrich Schiller University Jena. Funded by the Helmholtz Association through the Impuls- und Vernetzungsfonds, Helmholtz Postdoc Programme (PD-316).

† C.Kohlfuerst@gsi.de

Probing vacuum birefringence using x-ray free electron and optical high-intensity lasers

F. Karbstein[1,2] *and C. Sundqvist*[1,2]

[1]Helmholtz-Institut Jena, Germany; [2]Theoretisch-Physikalisches Institut, FSU Jena, Germany

Vacuum birefringence is one of the most striking predictions of strong field quantum electrodynamics: Probe photons traversing a strong field region can indirectly sense the applied "pump" electromagnetic field via quantum fluctuations of virtual charged particles which couple to both pump and probe fields. We have performed a dedicated theoretical analysis of the proposed discovery experiment of vacuum birefringence at an x-ray free electron laser/optical high-intensity laser facility. Our study facilitates stringent quantitative predictions and optimizations of the signal in an actual experiment.

The quantum vacuum amounts to a highly nontrivial state, characterized by the omnipresence of fluctuations of virtual particles. While the microscopic theory of quantum electrodynamics (QED) does not provide for a direct (tree-level) interaction among photons, effective interactions of this kind are induced by quantum fluctuations of electrons and positrons. Specifically in strong electromagnetic fields quantum fluctuations give rise to effective, nonlinear interactions among photons and macroscopic electromagnetic fields [1]. One of the most famous optical signatures of QED vacuum nonlinearity is vacuum birefringence [2] experienced by probe photons traversing a strong field region (cf. Fig. 1).

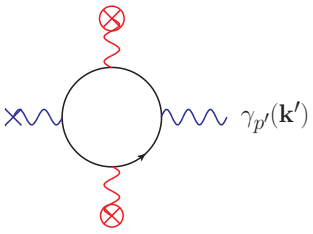

Figure 1: Microscopic origin of vacuum birefringence. Incident probe photons ($\times$) sense the strong field of the high-intensity laser ($\otimes$) via a virtual electron-positron fluctuation. This effective coupling can change the kinematic and polarization properties of probe photons originally prepared in a well-defined state.

A recent study [4] emphasized the feasibility of the detection of vacuum birefringence with state-of-the-art technology, employing x-ray free electron lasers (FELs) and high-power optical lasers [3]. The key idea is to exploit the scattering of signal photons out of the cone of the incident probe beam. The demands on the polarization purity are less stringent for detection under such angles due to the significantly lower background photon flux. In Ref. [4] this scenario was studied under idealized conditions, assuming the beam axes of the pump and the probe to be perfectly aligned and the pulses to be exactly counter-propagating. While the pump was realistically modeled as a Gaussian laser pulse in the paraxial approximation, the description of the probe was less elaborate and only its essential features were explicitly accounted for.

In the present study [5] we go beyond these limitations and consider probe beams of finite width and generic elliptically shaped cross-sections, see Fig. 2. Besides, we account for several additional parameters of experimental relevance, like a finite angle between the beams' axes and finite impact parameters. These refinements facilitate unprecedented theoretical predictions of the experimental signals attainable in a dedicated discovery experiment of QED vacuum birefringence at an FEL/high-intensity laser facility, like the upcoming Helmholtz International Beamline for Extreme Fields (HIBEF) at the European XFEL at DESY (cf. also [6]).

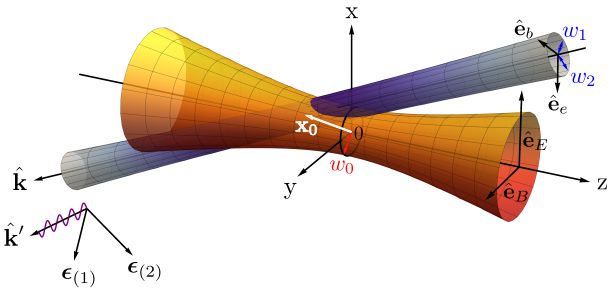

Figure 2: Sketch of the considered scenario. The transverse profiles of the pump and probe laser beams are depicted in orange and blue, respectively. We look for signal photons scattered into $\hat{\mathbf{k}}'$ direction in the far-field.

We are confident that our analysis [5] will facilitate stringent quantitative predictions and optimizations of the signal of vacuum birefringence in an actual experiment.

References

[1] W. Heisenberg and H. Euler, Z. Phys. **98**, 714 (1936).

[2] J. S. Toll, Ph.D. thesis, Princeton Univ., 1952 (unpublished).

[3] T. Heinzl, B. Liesfeld, K. U. Amthor, H. Schwoerer, R. Sauerbrey and A. Wipf, Opt. Commun. **267**, 318 (2006).

[4] F. Karbstein, H. Gies, M. Reuter and M. Zepf, Phys. Rev. D **92**, 071301 (2015)

[5] F. Karbstein and C. Sundqvist, Phys. Rev. D **94**, 013004 (2016).

[6] H. -P. Schlenvoigt, T. Heinzl, U. Schramm, T. Cowan and R. Sauerbrey, Physica Scripta **91**, 023010 (2016).

Critical Schwinger Pair Production

H. Gies[1,2] *and T. Torgrimsson*[3]

[1]Helmholtz Institute Jena, Germany; [2]Theoretisch-Physikalisches Institut, Abbe Center of Photonics, Friedrich Schiller University Jena, Germany; [3]Fakultät für Physik, Universität Duisburg-Essen, Lotharstraße 1, Duisburg 47048, Germany

We study electron-positron pair production by spatially inhomogeneous electric fields. Depending on the localization of the field, a critical point (critical surface) exists in the space of field configurations where the pair production probability vanishes. Near criticality, pair production exhibits universal properties similar to those of continuous phase transitions. We extend results previously obtained in the semi-classical (weak-field) critical regime to the deeply critical regime for arbitrary peak field strength. We find an enhanced universality, featuring a unique critical exponent $\beta = 3$ for all sufficiently localized fields.

Universality is a paradigm that often arises from the dominance of long-range fluctuations near critical points, washing out the effect of microscopic details on the long-range observables. This form of universality can be cast into scaling laws of observables which are characterized by universal critical exponents that depend only on a few gross features of the system such as dimensionality, symmetries and the number and nature of the long-range degrees of freedom. Standard examples are provided by critical phenomena in spin systems or liquid-gas transitions.

In a previous work [1], we had found aspects of universality also in Schwinger pair production [2], where an analogue of a critical point exists in the form of field configurations that provide the minimum of electrostatic energy to produce a (real) pair from vacuum. This makes universality in Schwinger pair production a rather special example, the origin of which has a clear physical picture: the relevant long-range fluctuations average over the local details of the pair-producing field profile, giving rise to a scaling law that depends only on the large-scale properties of the field.

In addition to the previously studied *semiclassical critical regime*, we have now been able to address the *deeply critical regime* in the immediate vicinity of the critical point, exhibiting even enhanced universality properties [3]. Criticality occurs if the work done by an electric field on a virtual particle-antiparticle fluctuation equals their rest mass. This point of energetic criticality can be summarized in a dimensionless parameter γ approaching $\gamma \to 1$. The deeply critical regime supports an even higher degree of universality, with the same scaling law as a function of the Keldysh parameter γ,

$$\mathrm{Im}\,\Gamma \sim (1-\gamma^2)^\beta, \quad \beta = 3, \tag{1}$$

for all fields that asymptotically vanish faster than $|x|^{-3}$. The result holds for scalar and spinor QED in all field-strength regimes.

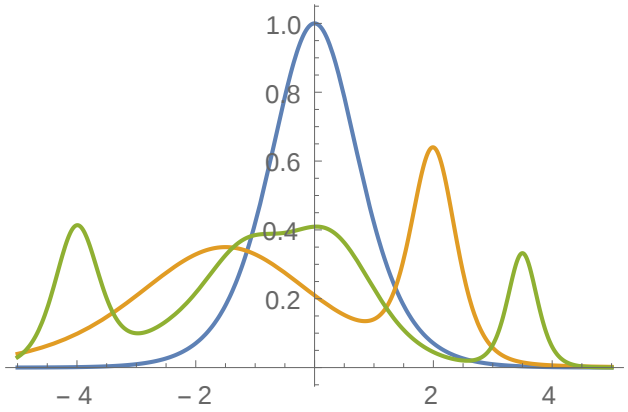

Figure 1: Various examples for critical field profiles with exponent $\beta = 3$ in the deeply critical regime. The onset of criticality is determined by the asymptotic behavior (exponential in these examples. The critical scaling law Eq. (1) is independent of the local details of the field profiles.

The highest degree of universality is found for spinor QED in the strong-field regime, where paraelectric dominance also establishes a universal prefactor. The scaling law Eq. (1) is modified for more gradually vanishing fields. E.g., fields that vanish as $|x|^{-2}$ obey the same scaling law as in the semiclassical regime.

In summary, we have corroborated an analogy between Schwinger pair production and continuous phase transitions. This analogy is quantitatively manifest in universal scaling laws for the onset of pair production in spatially inhomogeneous electric backgrounds. The scaling laws show a high degree of universality, being enhanced in the deeply critical regime, as the corresponding scaling law only depends on the large-scale properties of the background and become insensitive to the microscopic details.

References

[1] H. Gies and G. Torgrimsson, Phys. Rev. Lett. **116**, no. 9, 090406 (2016).

[2] J. S. Schwinger, Phys. Rev. **82** (1951) 664.

[3] H. Gies and G. Torgrimsson, Phys. Rev. D **95**, no. 1, 016001 (2017).

MCDF Isotope-Shift and Hyperfine Calculations for Heavy Elements *

R. Beerwerth† [1,2] *and S. Fritzsche*[1,2]

[1]Helmholtz Institute Jena, Jena, Germany; [2]Theoretisch-Physikalisches Institut, Universität Jena, Jena, Germany

Today, laser-spectroscopic studies are performed at reactor facilities in on-line experiments and allow to investigate long chains of short-lived radioactive nuclei. Methods such as the resonant laser ionization and spectroscopy technique are applied to measure hyperfine spectra and isotope shifts. These atomic data is subsequently utilized to obtain information about the produced nuclei such as the shape, size, spin and nuclear moments [1]. The isotope shift has two contributions, the mass shift that arises from the nuclear recoil and the field shift that is caused by a change in the nuclear charge distribution between different nuclei. These contributions can be parametrized by two parameters, the mass-shift factor and the field-shift factor, both of which can be computed from atomic theory [2].

We apply the relativistic multi-configuration Dirac-Fock (MCDF) method to compute the isotope-shift parameters and hyperfine coupling constants for heavy elements. This method is implemented in the GRASP2K [3] package, which is utilized to obtain approximate wave functions that are subsequently used to compute the isotope-shift parameters and hyperfine coupling constants. The computed isotope-shift parameters are then utilized to separate the mass and field-shift contribution to the total isotope shift and to extract the mean-squared charge radii of the nucleus [1]. The computed hyperfine coupling constants are used to extract the nuclear magnetic dipole and electric quadrupole moments from the measured HFS A and B values [1].

Here, we report on our calculations for the $6d7s^2\,{}^2D_{3/2} \rightarrow 6d7s7p\,{}^4P^o_{5/2}$ transition at $438.58\,\mathrm{nm}$ ($22801.1\,\mathrm{cm}^{-1}$) in neutral actinium, which was recently studied by resonant laser ionization spectroscopy [1]. For these computations, the multiconfiguration basis was generated by virtual excitations from a set of reference configurations to an active space that is systematically enlarged by adding up to five layers of correlation orbitals, and with angular momenta up to g. We take single, double and triple excitations from the 6d7s valence shells into account. Furthermore, core-valence correlation is accounted for by performing single excitations from the 6p-shell together with a second excitation from one of the valence shells and core polarization is included by single excitations from all core orbitals into the active space.

The mass-shift constant was found to be approximately $M = 500\ \mathrm{GHz\,amu}$, which is negligible when compared to the field-shift constant $F = -39(2)\,\mathrm{GHz/fm^2}$, as it is expected for heavy elements.

To estimate the uncertainty of the field shift, several independent calculations were carried out. In Fig. 1 a), we show the computed transition energy and in Fig. 1 b) the corresponding field-shift factor for three different calculations as a function of the size of the active space. The experimental value of the transition energy is marked by the horizontal line. Each model calculation is denoted by one color, where the dots mark the computed value of the energy and field-shift factor for a given size of the active space. Here, the lines are just drawn to guide the eye. As seen from this figure, both the transition energy as well as the field-shift factor F stabilize as the size of the active space is increased, though differences between the models remain. The agreement with the experimental transition energy is best for the green curve, and hence the corresponding field-shift factor was rounded and selected as the final value. The deviation between the different models shows that an estimated uncertainty of roughly 5% for the field shift seems reasonable. We also note, that the nuclear radius of all actinium isotopes is currently not known, which leads to an additional uncertainty of the field-shift factor, that is estimated to be below $1\,\mathrm{GHz/fm^2}$.

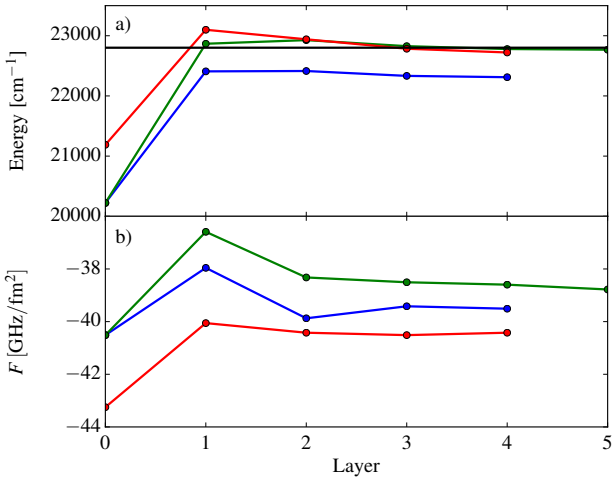

Figure 1: a) The computed $6d7s^2\,{}^2D_{3/2} \rightarrow 6d7s7p\,{}^4P^o_{5/2}$ transition energy as obtained from different model computations as a function of the size of the active space. b) The corresponding field-shift factors within the same computational models.

References

[1] R. Ferrer et al., Nat. Commun. 8 (2017) 14520

[2] B. Cheal, T. E. Cocolios, S. Fritzsche, Phys. Rev. A 86 (2012) 042501

[3] P. Jönsson et al., Comput. Phys. Commun. 177 (2007) 597-622

*This work has been supported by the BMBF (Grant No. 05P15SJCIA).

† Randolf.Beerwerth@uni-jena.de

Energy levels, lifetimes and transition rates in Ni XII

M. Bilal[*1,2], *R. Beerwerth*[1,2], *and S. Fritzsche*[1,2]

[1]Helmholtz Institute Jena, Fröbelstieg 3, 07743 Jena, Germany; [2]Theoretisch-Physikalishes Institut, Freidrich-Schiller-Universität Jena, D-07743, Germany

The astrophysics and experimental atomic physics communities require new and increasingly accurate theoretical predictions for the identification and interpretation of the observed spectral data of ionized atoms in all ionization stages. Chlorine like nickel Ni XII is an important member in the group of iron-peak elements. Such nickel ions exist in different astronomical objects, for instance in black hole x-ray binaries, clusters of galaxies, supernova remnants and the center of the Milky Way galaxy. Indeed nickel has been found second most abundant transition element in our sun after iron. Similarly, nickel is also an important impurity element in the Joint European Torus (JET) as well as in many other tokamak fusion test reactor plasmas.

Despite the importance of Ni^{11^+} ions only few of the level energies are well characterized in the literature [1]. This is mainly because the experimental data can only be compared with less accurate *ab initio* calcualtions or even semi-empirically computed values. For these ions the theoretical complexity arises due to the near degeneracy characteristic and strong mixing of levels with the same J values and parity. There has been much theoretical effort in the past in order to improve the structure data for Ni^{11^+}. Until today, however, these computations do not provide consistent data for future measurements except for the few lines.

Very recently Del Zanna & Badnell reported new observed and semi-empirical theoretical data for the excitation energies, transition rates and electron impact excitation rates for Ni^{11^+} [2]. Their semi empirical adjusted values for strong transition are in excellent agreement with observed values. For week forbidden transitions, however, their data is less accurate as compared to observed values. To improve the *ab initio* database on Ni^{11^+}, we carried out a detailed computation for the transition rates, oscillator strengths, and lifetimes by taking into account all allowed E1 and forbidden M1, E2, and M2 transitions among the first 31 lowest energy levels. In LS coupling, these lines arise from three configurations $3s^23p^5$, $3s3p^6$ and $3s^23p^43d$. We used the multi-configuration Dirac Hartree-Fock (MCDHF) method in jj-coupling [3] which is impelemented in the code GRASP2K [4].

In some more detail, we performed the calculations for two odd parity states which belong to the $3s^23p^5$ ground configuration with total angular momentum $J = 1/2$ and $J = 3/2$ and for the 29 even parity states from the $3s3p^6$ and $3s^23p^43d$ configurations with total angular momenta in the range $J = 1/2, ..., 9/2$. All important relativistic and correlation contributions have been incorporated in to the systematically enlarged MCDHF computations. In total, correlation layers up to the principal quantum number $n = 7$ and orbital quantum number $l = h$ are used in the expansion of odd and even atomic states, and which results in approximately two million configuration state function basis.

Table 1: Selection of few M1 transition rates A (s^{-1}) and wavelengths λ in $\mathring{A}$ between levels with $J = 7/2$ and $J = 9/2$.

Trans	$A_{_P}$	$A_{_{CHI}}$	$\lambda_{_P}$	λ_{obs}
8-5	2.45e+01	2.111e+01	3129.913	3171.18
21-8	1.69e+02	1.538e+02	2375.826	2398.08
2-1	2.35e+02	2.373e+02	4241.258	4232.09
16-5	7.53e+01	6.029e+01	1684.884	1686.74
10-5	1.72e+01	1.599e+01	2561.926	2580.38
16-8	4.35e+01	3.835e+01	3649.437	3603.34
20-10	6.29e+01	5.246e+01	2894.917	2923.12
24-8	2.10e+02	1.979e+02	1224.073	1225.05

$_P$: Present calculation including core-valence correlations
$_{CHI}$: Semi-empirical values of CHIANTI V. 8 [5]
$_{obs}$: Experimental values of [2]

A very good agreement with experiment is obtained for most of the energy levels. In table 1, a brief comparison of our M1 transition probabilities and transition wavelengths is given. Our predicted wavelengths for strong transitions deviate only about 0.8%, while they excellently match for forbidden transition within the range of 1% deviation. Overall, our results are better than obtained before in any *ab initio* investigation and may provide a benchmark for the future experiments.

References

[1] T. Shirai , J. Sugar, A. Musgrove and W. L. Wiese , *J. Phys. Chem. Ref. Data*, 8 (2000) 360.

[2] G. Del Zanna and N. R Badnell, *A & A*, A118 (2016) 585 .

[3] I. P. Grant, Relativistic Quantum Theory of Atoms and Molecules, *Springer* (2007) New York .

[4] P. Jönsson *et al*, *Comput. Phys. Commun.*, 184 (2013) 2197 .

[5] G. Del Zanna, K. P. Dere, P. R. Young, E Landi and H. E. Mason, *A & A*, A56 (2015) 582, .

* moazzam.bilal@uni-jena.de

Two-color photoionization by twisted X-waves in strong infrared fields*

B. Böning[†1], *W. Paufler*[1], *and S. Fritzsche*[1,2]

[1]University of Jena, Germany; [2]Helmholtz-Institute Jena, Germany

During the past decade, the generation of attosecond laser pulses enabled one to perform experimental studies of the electron dynamics in atoms. In particular, the photoionization by XUV pulses in the presence of an additional strong low-frequency laser field has attracted much interest. Such a setup allows, for example, to extract timing information about the ionization process and to characterize the participating laser pulses.

Until the present, however, most theoretical and experimental studies in this field have been performed by just using plane-wave laser pulses. In contrast to these previous investigations, we explore the two-color photoionization if the plane-wave XUV pulse is replaced by a twisted X-wave that carries additional orbital angular momentum (OAM). Detailed studies of the excitation and ionization by twisted light have revealed that the selection rules of both the bound-bound and bound-free transitions are modified [1, 2]. However, the presence of an additional plane-wave infrared field also affects the continuum states of the outgoing photoelectron and, hence, may lead to the formation of sidebands in the recorded spectra. It was shown that these sidebands exhibit asymmetries (or dichroisms) due to a flip of the OAM quantum number of the twisted beam and/or the helicities of the twisted and the NIR beams [3].

A question of particular interest is how the sidebands are modified and how the streaking regime arises if the duration τ_X of the twisted pulse is reduced to the order of the infrared cycle length T_{IR}. For plane-wave pulses, this transition is displayed in Fig. 1. For $\tau_X < T_{IR}$, the photoelectrons all appear at a definite time in the infrared field and are streaked to the same energy. Therefore, the energy-differential ionization probability exhibits a single peak in the streaking regime (black curve). If τ_X is increased, the photoelectrons enter the infrared field at different times, and their interference may then lead to the formation of sidebands ($\tau_X > T_{IR}$, blue and red curves). It was recently demonstrated that the angular distribution of photoelectrons in the transition regime provides information about the initial atomic state [4].

Due to the OAM of the twisted beam, the two-color photoionization with twisted X-waves of variable duration will enrich the angular distribution of photoelectrons in both the sideband and streaking regimes. We therefore expect that angle-resolved measurements of this ionization process will help to better understand the X-waves as well as the electron dynamics during the ionization process. Such experiments will soon be possible due to progress in the creation of short pulses carrying OAM.

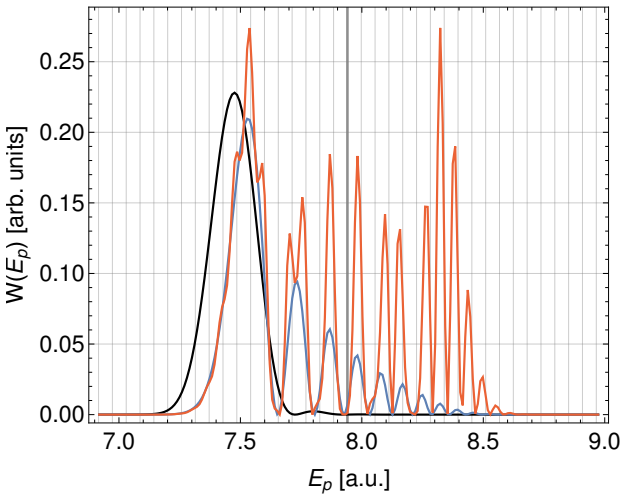

Figure 1: Energy-differential ionization probability $W(E_p)$ for three durations τ_X of the ionizing XUV pulse with photon energy $\omega_X = 230$ eV. Red curve: sideband regime for $\tau_X = 7$ fs; black curve: streaking regime for $\tau_X = 1$ fs; blue curve: transition for intermediate $\tau_X = 3$ fs. The central black line marks the position of the XUV photoline without infrared field. Further laser parameters are $\lambda_{IR} = 800$ nm, $I_{IR} = 2 \times 10^{12}$ W/cm^2 and $I_X = 10^9$ W/cm^2. The black curve is magnified by a factor of 3.

References

[1] O. Matula *et al.* , *J. Phys. B* **46** 205002 (2013)

[2] M. Scholz–Marggraf *et al* , *Phys. Rev. A* **90** 013425 (2014)

[3] D. Seipt *et al.* , *Phys. Rev. A* **94** 053420 (2016)

[4] A. Kazansky *et al.* , *Phys. Rev. A* **82** 033420 (2010)

* Work supported by the DFG priority programme 1840, "Quantum Dynamics in Tailored Intense Fields".

† birger.boening@uni-jena.de

Use of atomic processes in particle-in-cell computations of solid-density plasmas

D. Wu[1,2] *and S. Fritzsche*[2,3]

[1]Shanghai Institute of Optics and Fine Mechanics, China; [2]Helmholtz-Institut Jena, Germany;
[3]Friedrich-Schiller-Universität Jena, Germany

A physical model based on a Monte-Carlo approach is proposed to calculate the ionization dynamics of hot-solid-density plasmas within particle-in-cell simulations, and where the impact (collision) ionization (CI), electron-ion recombination (RE) and ionization potential depression (IPD) by surrounding plasmas are taken into consideration self-consistently [1]. When compared with other models, which are applied in the literature for plasmas to thermal equilibrium, the temporal relaxation of ionization dynamics can also be simulated by the proposed model. The proposed model is implemented into a particle-in-cell (PIC) code, and where the (final) ionization equilibrium is formed by competitions between CI and its inverse process (i.e., RE). Comparisons between the full model and model without IPD or RE are performed. Our results, as shown in Fig. 1, indicate that for bulk aluminium at temperature of 1 to 1000 eV, i) the averaged ionization degree increases by including IPD; ii) the averaged ionization degree is significantly over estimated when the RE is neglected. A direct comparison from the PIC code is made with the existing models for the dependence of averaged ionization degree on thermal equilibrium temperatures, and shows good agreements with that generated from Saha-Boltzmann model or/and FLYCHK code.

A Monte-Carlo approach to proton stopping in warm dense matter is also implemented into our particle-in-cell code [2]. This approach is based on multiple electron-electron, electron-ion and ion-ion binary collision and accounts for both, the free and bound electrons in the plasmas. As shown in Fig. 2, in the low-temperature limit, when "all" electrons are bound to the nucleus, the stopping power coincides with the predictions from the Bethe-Bloch formula and is consistent with the data from the NIST database. At higher temperatures, some of the bound electrons are ionized and this increases the stopping power in the plasmas as demonstrated by Zylstra et al. [3]. At even higher temperatures, the degree of ionization reaches a maximum and thus decrease the stopping power due to the suppression of collision frequency between projected proton beam and hot plasmas in the target.

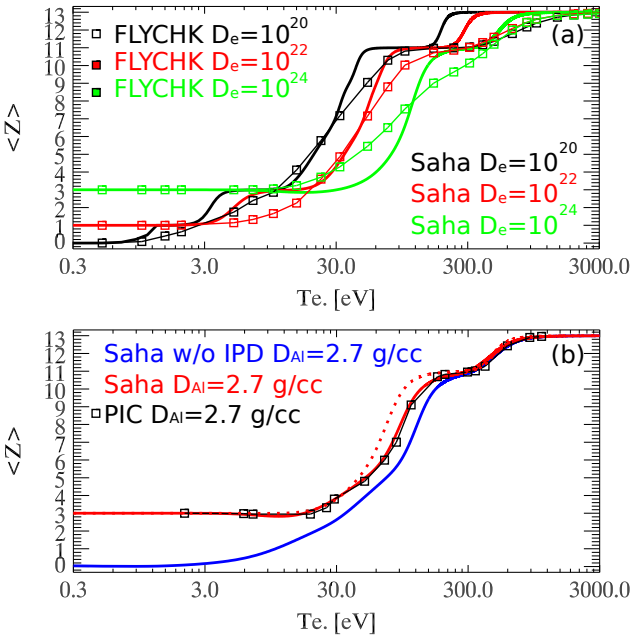

Figure 1: The averaged ionization degree of bulk aluminium as a function of plasma temperature. (a) Blue, red and green lines (square) are the results calculated by Saha-Boltzmann Equation (FLYCHK code). (b) Red and green lines are the results calculated by Saha-Boltzmann Equation with updated numerical scheme, including IPD and excluding IPD.

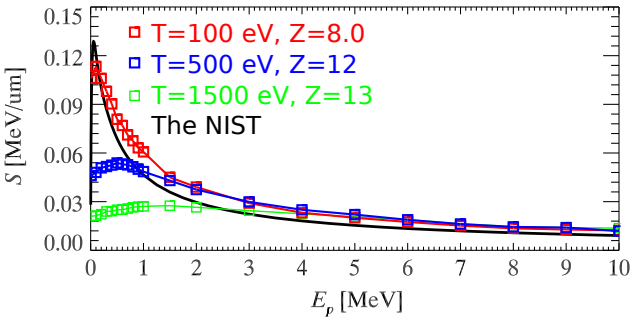

Figure 2: Stopping power as a function of projected proton energy. Results from our PIC simulations are compared with that from the NIST database.

References

[1] D. Wu, X. T. He, W. Yu, and S. Fritzsche, Phys. Rev. E 95 (2017) 023207.

[2] D. Wu, X. T. He, W. Yu, and S. Fritzsche, Phys. Rev. E 95 (2017) 023208.

[3] A. B. Zylstra et al., Phys. Rev. Lett. 114 (2015) 215002.

Spin evolution of two valence electrons in two separated ions

B. Goswami[1], *A. V. Volotka*[1], *and S. Fritzsche*[1,2]
[1]Helmholtz Institute Jena, Germany; [2]University of Jena, Germany

Understanding of the spin evolution of two or more qubits is a key task in physics and quantum engineering. In particular, the transport and relaxation of spin waves in metals and semiconductor are of fundamental interest not only in basic research, but also in the field of spintronics [1], in which the spin of electrons is utilized *instead of* or *in addition* to the charge degrees of freedom. In spin-field effect transistors, for example, the spin-orbit interaction is known to control the motion of electrons inside the semiconductor channel.

The evolution of two coupled spins has been measured recently by Kotler *et al* [2] for two separated ions. In their simplified model, however, these authors describe the associated spin-magnetic moment of the electrons as point-like dipole, an approximation that breaks down at small distances. More generally, therefore, all the spatial and spin degrees of freedom have to be accounted for the two valence electrons. In present work, we aim to work out a theory which goes beyond the leading order in dealing with the spin-dependent interactions of electrons.

In more detail, we have explored probable spin-flip transitions of the two electrons. Since the spin-flip of different spin states can be represented by a parity sign, we have studied the difference in parity for the different spin states. We especially considered the initial spin state of two electrons at $|\uparrow\downarrow\rangle$ and calculated the time evolution of this state as a function of interaction time (t) at different inter-ionic distances (d) and for a typical strength of the external magnetic field ($\vec{B}$).

Fig. 1 displays how the parity changes with t, if terms beyond the leading order interactions are taken into account in the electron-electron interaction operator. Our results show that the spin-spin interaction always changes the spin of two electrons together, while the additional terms in the Hamiltonian may flip also the spin of just a single electron, and which results in a different behaviour of the entangled Bell states. Moreover, it is found that the parity difference (of Fig. 1), is highly sensitive to the inter-ionic distances as well as to the strength of the external magnetic field.

In this work, an attempt to correlate our theory to the experiment of Kotler *et al* [2] is also undertaken. For this purpose, the difference in parity of $|\uparrow\downarrow\rangle$ is calculated by using their experimental [2] inter-ionic distance (d = 2.4 μm) and strength of external magnetic field ($|\vec{B}|$ = 0.44 mT). It is found that the difference in parity of $|\uparrow\downarrow\rangle$ is 1.5×10^{-7} at 15 second, which is expected to slightly effect on the electron-electron interaction-strength in their simplied model. Based on the discrepancy of their simplified model and their experiment [2], a new constraint on exotic dipole-dipole interactions between electrons were established by Kotler *et al* [3]. Since the effect of beyond leading order interactions is minor at the micrometer scale, it doesn't change the conclusion of their article. However, if the two ions are located at much closer, then it could be helpful to include the terms beyond the leading order interactions.

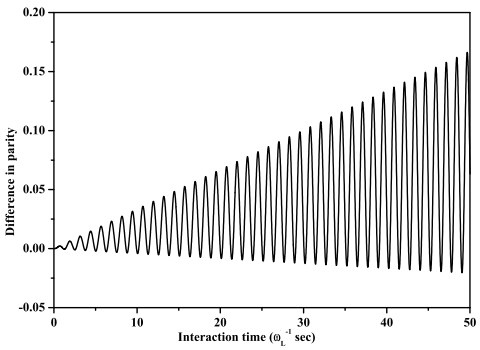

Figure 1: The difference of parity of $|\uparrow\downarrow\rangle$ at $d = 10^3 a_0$ and ω_L = 1.4 MHz (where, a_0 is Bohr radius and ω_L is spin Larmor frequency) with $|\vec{B}|$ = 0.1 mT.

In summary, the spin evolution of two spin-1/2 valence electrons, located at two separated ions, is investigated with the help of Breit equation. This evolution that arise solely depends on their dipole-dipole magnetic interaction. Special attention is paid to the effects beyond the leading order of the dipole-dipole magnetic interaction. In contrast to just including the leading order, it is found that the spin-spin interactions flips the spin of both electrons together, while the spin-orbit interactions typically changes the spin of just single electron. As a consequence, different behaviour is observed in the time evolution of two different entangled Bell states.

References

[1] S.A. Wolf *et al.*, Science 294 (2001) 1488.

[2] S. Kotler *et al.*, Nature 510 (2014) 376.

[3] S. Kotler *et al.*, Phys. Rev. Lett. 115 (2015) 081801.

Two-photon K-shell ionization cross sections for neutral atoms

J. Hofbrucker [*1,2], *A. V. Volotka*[1,3], *and S. Fritzsche*[1,2]

[1]Helmholtz Institute Jena; [2]Friedrich-Schiller Universitat Jena; [3]St. Petersburg State University

Deep understanding of nonlinear processes became desirable with the recent development of bright and high-energetic free-electron laser sources. Two-photon ionization is one of the fundamental nonlinear processes, and a benchmark for studying the interaction of intense light with matter. Although recent experiments measured the two-photon K-shell ionization of mid-Z elements, the comparison of experiment with theory was based so far on the Schrödinger's nonrelativistic theory, and with little account of many-electron effects. To understand the interplay of relativistic and many-electron effects upon the two-photon K-shell ionization of mid- and high-Z elements, further theoretical effort had to be paid to this fundamental process.

In our recent works [1, 2], we carried out relativistic computations for the non-resonant two-photon K-shell ionization of neutral atoms, where we applied the independent-particle approximation. This allows us to consider only a single active electron and account for all the other electrons by a screening potential in the interaction Hamiltonian of the Dirac equation. Within this framework, we analysed the importance of relativistic effects as well as the screening effects on the total cross section. We found, that relativistic effects may decrease the total cross section of ionization of heavy elements by a factor of up to three. Moreover, we analysed the individual relativistic contributions to the cross section. While the dominant contribution arises from the relativistic contraction of the K-shell orbital (direct relativistic effect), higher multipoles of the electron-photon interaction operator are less important. However, higher multipoles need to be incorporated into the calculations of the angle-differential cross section, as they significantly distort the electron distribution along the incident photon direction [3]. Effects beyond no-pair approximation, i.e. summation runs over both over positive *and* negative energy states of the intermediate state, were found to be gauge-dependent. While in the velocity gauge going beyond no-pair approximation yields slightly larger cross section, no effects were found in the length gauge.

The screening of the active electron by all the other electrons results in an unexpected decrease of the total cross section for light atoms and near to the ionization threshold. A closer inspection of this behaviour reveals a more physical explanation of the drop in the cross section. For slow photoelectrons, in particular, the screened wavefunction of the dominant d-wave shifts away from the nucleus. As a consequence, the overlap integral of this dominant ionization channel with bound state wavefunctions is low, hence, the total cross section is reduced. This influence occurs even more pronounced in the photoelectron angular distribution, where it leads to an elliptical dichroism in the photoelectron distribution, see Figure 1. As this effect is strongest for Ne atom, the detection of the dichroism is feasible and could serve for an experimental verification of the importance of screening effects.

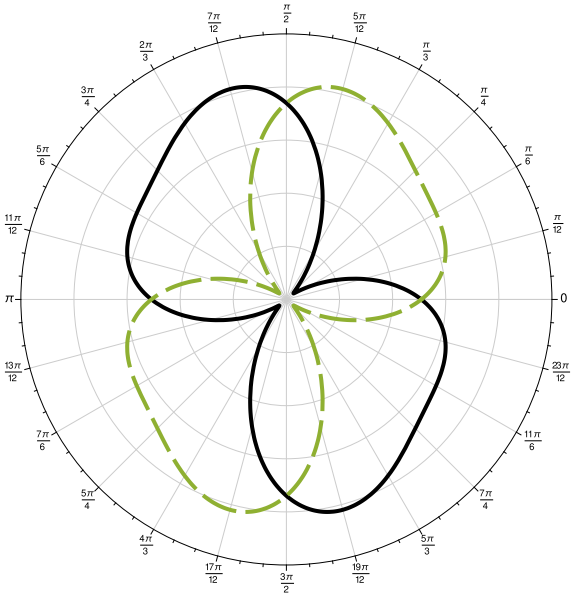

Figure 1: Elliptical dichroism in the non-resonant two-photon K-shell ionization of neutral Ne. Different electron angular distributions are obtained depending whether the photons are left- or right- elliptically polarized. This behaviour has a high potential to be used for experimental verification of the importance of screening effects.

References

[1] J. Hofbrucker, A. V. Volotka, and S. Fritzsche, Phys. Rev. A 94 (2016) 063412.

[2] J. Hofbrucker, A. V. Volotka, and S. Fritzsche, submitted to Nucl. Instr. Meth. Phys. Res.

[3] J. Hofbrucker, A. V. Volotka, and S. Fritzsche, to be published.

* email: jiri.hofbrucker@uni-jena.de

Absorption of twisted light by a mesoscopic atomic target

A. A. Peshkov[*1], *V. G. Serbo*[2,3], *S. Fritzsche*[1,4], *and A. Surzhykov*[1]

[1]Helmholtz-Institut Jena, Germany; [2]Novosibirsk State University, Russia; [3]Sobolev Institute of Mathematics, Novosibirsk, Russia; [4]Friedrich-Schiller-Universität Jena, Germany

The beams of light possessing a nonzero projection of the orbital angular momentum on their propagation direction are known as twisted (or vortex) beams. Twisted light beams with a wide range of energy $10\,\text{meV} < \hbar\omega < 100\,\text{eV}$ became experimentally accessible in the last few years. This has stimulated a number of theoretical and experimental studies of light-matter interaction processes with twisted light: Compton scattering by free electrons, ionization and excitation of atoms and molecules, transition in quantum dots, generation of the atomic vortex state in a Bose-Einstein condensate. In a recent work [1], we have performed a theoretical study of the absorption of a twisted (Bessel) light beam by hydrogen atoms. Here the atoms were assumed to be confined and localized in the target that corresponds to experiments on the photoexcitation of atoms or ions in traps. We also supposed that the atoms have a Gaussian spatial distribution in the target with the dispersion w characterizing the target size. The calculations were carried out for the $1s \to 2p$ atomic transition driven by the Bessel beam of the helicity λ, which propagates along the quantization z axis and is characterized by the projection m_γ of the total angular momentum (TAM). The beam, in addition, has well-defined longitudinal momentum k_z as well as absolute value of the transverse momentum $\varkappa$, which determine the so-called opening angle $\theta_k = \arctan(\varkappa/k_z)$.

Within the nonrelativistic framework, the density matrix formalism and first-order perturbation theory were used to derive the alignment parameters $\mathcal{A}_{20}$ and $\mathcal{A}_{21}$ of the excited atomic state. The parameter $\mathcal{A}_{20}$, in particular, describes the relative population of magnetic sublevels of excited atoms, while $\mathcal{A}_{21}$ characterizes the coherence between between the sublevels. Our calculations have shown that the more pronounced difference between alignment parameters for different TAM m_γ of the beam is found when the target is small $w < 200$ nm. For such sufficiently small atomic targets, in Fig. 1 we present the alignment parameters $\mathcal{A}_{20}$ and $\text{Im}(\mathcal{A}_{21})$ (real part of $\mathcal{A}_{21}$ is always zero) as functions of the distance b_t from the beam axis to the target center. As can be seen from Fig. 1, the parameter $\mathcal{A}_{21}$ is zero if the center of the target lies at the beam axis ($b_t = 0$). This can be explained by symmetry: if the system "atoms-beam" has axial symmetry, which is the case when the target center lies at the beam axis, the alignment parameter $\mathcal{A}_{21}$ must vanish. For the targets displaced from the beam axis, the alignment parameters $\mathcal{A}_{20}$ and $\mathcal{A}_{21}$ are both nonzero and oscillate as functions of the distance b_t. These oscillations are revealed because of the oscillatory transverse structure of the field for Bessel beams. We note that these changes in the alignment of atoms can be observed experimentally by measuring the linear polarization of the subsequent fluorescence radiation.

In summary, it was shown that the alignment parameters of excited atomic states are very sensitive to the size of the atomic target and its position with respect to the beam axis. Moreover, we demonstrated that the TAM of the incident Bessel beam can be transferred to the target atoms.

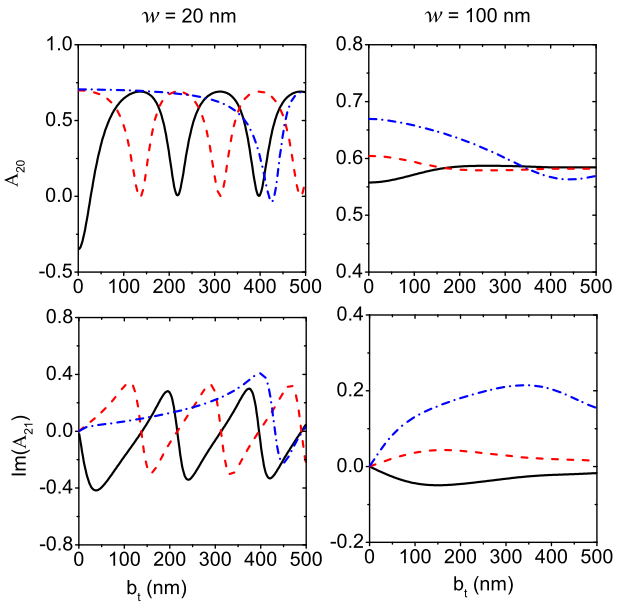

Figure 1: Alignment parameters $\mathcal{A}_{20}$ (top) and $\text{Im}(\mathcal{A}_{21})$ (bottom) as functions of the distance b_t to the center of the atomic target for the $1s \to 2p$ excitation by the Bessel light beam. Results are shown for three different TAM projections of the beam: $m_\gamma = 0$ (black solid lines), $m_\gamma = 1$ (red dashed lines), and $m_\gamma = 5$ (blue dash-dotted lines), when the sizes of target $w = 20$ nm (left) and $w = 100$ nm (right) are assumed. The opening angle of the beam $\theta_k = 20°$, its helicity $\lambda = +1$, and the photon energy $\hbar\omega = 10.2$ eV are fixed.

References

[1] A. A. Peshkov, V. G. Serbo, S. Fritzsche, and A. Surzhykov, Phys. Scr. 91 (2016) 064001.

* anton.peshkov@uni-jena.de

Auger cascades in resonantly excited neon*

S. Stock[†1,2], *R. Beerwerth*[1,2], *and S. Fritzsche*[1,2]

[1]Friedrich Schiller University Jena, Germany; [2]Helmholtz Institute Jena, Germany

Auger electron spectroscopy is an important tool for studying the electronic structure of atoms and molecules. In particular, cascade Auger decays of inner-shell vacancies in noble gases have been investigated extensively in the past decades. In such a (two-step) cascade, the first Auger electron leaves the atom in an autoionizing state which subsequently decays by emission of a second Auger electron, leading to double autoionization.

Until the present, almost all theoretical studies of these decay cascades were restricted to a few specific decay paths. In contrast to this, we investigated the complete two-step Auger cascades that follow resonant excitation of the $1s^{-1}3p\ ^1P_1$ and $1s^{-1}4p\ ^1P_1$ levels in neutral neon [1]. For this purpose, we performed extensive MCDF calculations by systematically including a large number of intermediate and final states. For the first step, especially, we considered all possible participator and spectator decays and took into account also (single-electron) shake processes of the 3p and 4p electron. For the second step, we included all (energetically allowed) transitions from the autoionizing Ne^+ levels to levels of the $2s^22p^4$, $2s2p^5$, and $2s^22p^3n\ell$ configurations of Ne^{2+}. In many of the second-step transitions, Auger electrons with very low energy are emitted. In order to accurately simulate the low-energy spectra, we employ experimental energies for the (known) energy levels of Ne, Ne^+, and Ne^{2+}.

We compare our simulated Auger electron spectra with available experimental data and found satisfying agreement. Fig. 1, for example, shows the dominant part of the Auger electron spectra of the first step of the cascade together with recent experimental data from Ref. [2]. Based on the simulated electron spectra, we are able to predict ion yields and shake probabilities that are in good agreement with experimental findings.

Our theoretical study demonstrates that complete electron spectra of Auger decay cascades can be simulated with quite satisfying accuracy. This requires extensive computations with correlated wave functions, for which the MCDF method has been found versatile. While the here considered autoionization of inner-shell excited neon atoms still refers to a rather simple system, these computations can be extended towards more complex Auger cascades. A careful (theoretical) analysis of such cascades may support also ongoing developments of new (magnetic-bottle) coincidence techniques as well as of time- and position-resolved detectors.

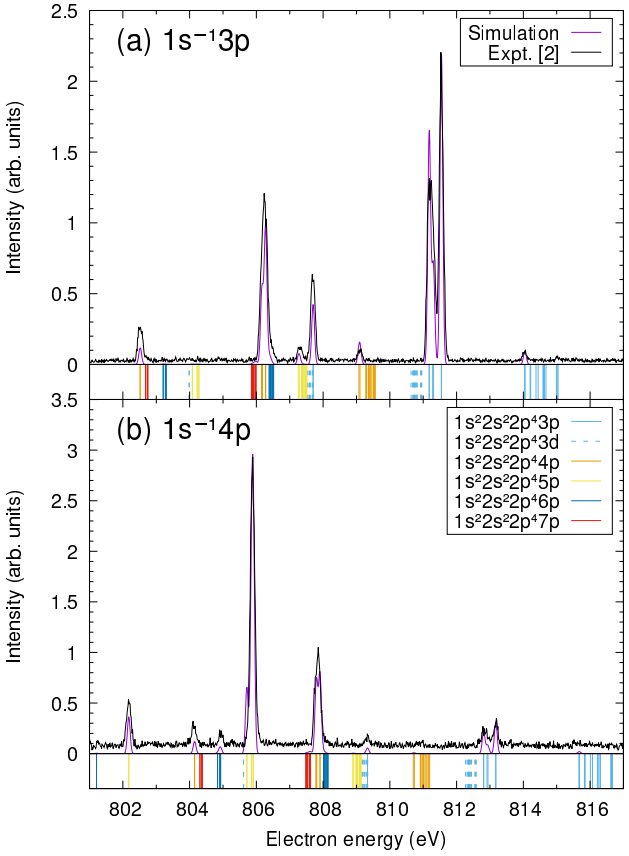

Figure 1: Part of the simulated electron spectra showing the transitions from the initially excited Ne $1s^{-1}np\ ^1P_1$ level to several fine-structure levels of the $2s^22p^4n\ell$ configurations of Ne^+. Experimental data from Ref. [2] is shown for comparison. Here, it should be noted that we employ experimental level energies in the calculations, so the energies of the observed transitions naturally match the experimental ones.

References

[1] S. Stock, R. Beerwerth, and S. Fritzsche, "Auger cascades in resonantly excited neon", to be submitted.

[2] Y. Tamenori and I. H. Suzuki, "Multiplet exchange Auger transitions following resonant Auger decays in Ne 1s photoexcitation", J. Phys. B 47 (2014) 145001.

* Work supported by BMBF contract No. 05K16SJA.

† sebastian.stock@uni-jena.de

Nuclear excitation by two-photon electron transition

A. V. Volotka[*1,2], *A. Surzhykov*[3,4], *S. Trotsenko*[1,5], *G. Plunien*[6], *Th. Stöhlker*[1,5,7], *and S. Fritzsche*[1,5]

[1]Helmholtz-Institut Jena, Germany; [2]St. Petersburg State University, Russia; [3]Physikalisch-Technische Bundesanstalt, Braunschweig, Germany; [4]Technische Universität Braunschweig, Germany; [5]Friedrich-Schiller-Universität Jena, Germany; [6]Technische Universität Dresden, Germany; [7]GSI, Darmstadt, Germany

Atomic physics has kept a tenable position for many decades in the foundation and development of our knowledge on nuclear properties. In particular, much informations about the nuclear spins, nuclear magnetic moments, and mean-square charge radii originate from atomic spectroscopy. Apart from the properties of the nuclear ground or isomeric states, atomic spectroscopy provides access also to the internal nuclear dynamics, e.g., to single nuclear resonances that can be accessed via certain electron transitions.

One of the intriguing applications concerns the low-lying isomeric nuclear excitation of the thorium isotope ^{229m}Th with an excitation energy of just a few eV, which could lead to a nuclear clock technology of unprecedented accuracy. Other potential applications refer to isotope separation as well as to energy storage and its controlled release.

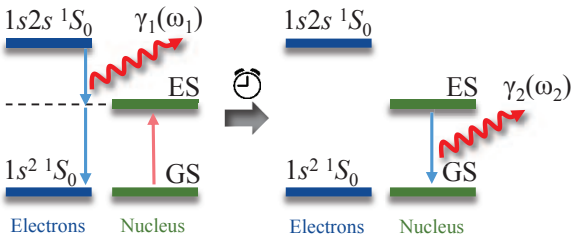

Figure 1: NETP mechanism.

In Ref. [1], we presented and discussed a new mechanism for nuclear excitation to which we refer as nuclear excitation by two-photon electron transition (NETP). An electron transition can proceed not only via the emission of one photon but also the simultaneous emission of two photons that just share the transition energy. In contrast to the one-photon transitions, where the photon frequency equals the transition energy, the energy distribution of the spontaneously emitted photons then forms a continuous spectrum. This implies, that some of the photons exactly match in their frequency with the nuclear transition energy as long as the nuclear excitation energy is smaller than the total electron transition energy. In this way, a nucleus may resonantly absorb the photon and gets excited. The NETP process is shown in Fig. 1 in a more picturesque way. The initial state (left panel), which is characterized by the $1s2s\ ^1S_0$ electronic state and the nuclear ground state (GS), decays into the final state (right panel) where both, the electrons and nucleus are in their $1s^2\ ^1S_0$ nuclear ground states, respectively. This decay occurs however via the intermediate cascade state with the nucleus being in the excited state (ES). During this process, again, two photons γ_1 (electron decay photon) and the delayed γ_2 (nuclear fluorescence photon) are emitted.

For the E1E1 two-photon transition $1s2s\ ^1S_0 \to 1s^2\ ^1S_0$ of heliumlike ^{225}Ac^{87+} ions with a (known) nuclear excited $3/2+$ level at energy $\omega_{\rm ES} = 40.09(5)$ keV, we found that the probability of the two-photon decay via nuclear excitation is surprisingly large, $P_{\rm NETP} = 3.5 \times 10^{-9}$, when compared with the overall and continuous two-photon emission. In order to verify the proposed mechanism, we have suggested to observe the delayed emission of the nuclear fluorescence γ_2 photons at the current GSI Heavy-Ion Research Facility in Darmstadt) facility. The initial $1s2s\ ^1S_0$ state can be efficiently produced in the collisions of lithiumlike ions of the given isotope with N_2 gas target via the selective K-shell ionization. The x-ray emission will be measured in coincidences with the detection of the up-charged (heliumlike) ions, whose efficiency is near to 100%. This experimental setup enables one to measure a very clean spectrum of the two-photon decay. In order to observe the delayed nuclear fluorescence photons γ_2, a high-efficiency in-vacuum x-ray detector use to be installed in order to cover a solid angle as large as possible. Moreover, fast transitions, that will mostly decay in the vicinity of the gas-target, will be shielded in order to reduce background in the measurement of the delayed photons. At the experimental storage ring (ESR) at GSI beams of $\gtrsim 10^8$ cooled ions can be provided in a such bunch and stored for collisions with the gas-jet target with areal densities above 10^{14} cm^{-2}. Because of the high revolution frequencies of ions in the storage ring (about 2 MHz) and, thus, the steadily recurring interaction of ions and target electrons, a very high luminosity can be achieved. We therefore expect to stimulate up to few hundreds NETP fluorescence photons per day of beamtime. Indeed, this looks feasible for the successful observation and characterization of the NETP process. Moreover, once the new FAIR accelerator complex has been built, the experiment will profit from a much higher luminosity as well as from the ability of measuring closer to the ion beam.

References

[1] A. V. Volotka, A. Surzhykov, S. Trotsenko, G. Plunien, Th. Stöhlker, and S. Fritzsche, Phys. Rev. Lett. 117 (2016) 243001.

* a.volotka@gsi.de

Access to the hyperfine splitting in highly charged helium-like ions via angle-resolved spectroscopic analysis

Z. W. Wu[1,2], *A. V. Volotka*[1,3], *A. Surzhykov*[4,5], *and S. Fritzsche*[1,6]

[1]Helmholtz Institute Jena, Germany; [2]Northwest Normal University, Lanzhou, China; [3]St. Petersburg State University, St. Petersburg, Russia; [4]Physikalisch-Technische Bundesanstalt, Braunschweig, Germany; [5]Technische Universität Braunschweig, Germany; [6]Friedrich-Schiller-Universität Jena, Germany

The hyperfine splitting of energy levels occurs mainly due to the interaction of bound electrons with a magnetic field generated by a nucleus. The strength of the nuclear magnetic field increases rapidly with an increase of the nuclear charge, e.g., for the case of ^{209}Bi nucleus the magnetic field at the nuclear surface reaches 10^9 T, which is several orders of magnitude higher than the field of the most powerful magnets. For this reason the investigation of the hyperfine splitting in highly charged ions attracts a continuous attention both from theory and experiment with the aim to probe the bound-state QED at extreme electric and magnetic fields. As the simplest atomic system, several high-precision measurements of the hyperfine structure in hydrogen-like ions have been performed since the pioneering experiment by Klaft *et al.* [1], which stimulated a number of theoretical calculations and developments on this topic, see review [2] and references therein.

Helium-like ions are still simple enough to be expected to serve also for such QED tests. To the best of our knowledge, however, there have been no such kind of experimental studies up to now, although the hyperfine quenching in helium-like ions was investigated. When compared to hydrogen- or lithium-like ions, the ground state of helium-like ions does not split into hyperfine levels. Moreover, as for the excited levels like $1s2p\ ^{1,3}P_1, F$, their linewidth is comparable to or even larger than their hyperfine splitting, which are hardly resolved due to their mutual overlap.

For this reason, we here propose a new scheme to measure the hyperfine splitting in helium-like ions by analyzing the angular distribution and degree of linear polarization of emitted x-ray fluorescence photons. To be more specific, we consider the two-step radiative decay

$$\begin{aligned} 1s2s\ ^1S_0, F_i + \gamma_1(\hbar\omega_1) \quad &\longrightarrow \quad 1s2p\ ^3P_1, F \\ &\longrightarrow \quad 1s^2\ ^1S_0, F_f + \gamma_2 \quad (1) \end{aligned}$$

of helium-like ions in order to resolve the hyperfine splitting of the intermediate level $1s2p\ ^3P_1$. In this scheme, the initial level $1s2s\ ^1S_0, F_i$ can be populated via the K-shell ionization of lithium-like ions at ion storage rings [3], or alternatively, via the prompt $2s2p\ ^1P_1, F \rightarrow 1s2s\ ^1S_0, F'$ decay following the resonant electron capture of initially hydrogen-like ions into the $2s2p\ ^1P_1$ level [4]. In the process (1), the first-step decay is stimulated by a laser light which has a proper intensity and an adjustable photon energy $\hbar\omega_1$ in order to compete with dominant $2E1$ decay of the initial $1s2s\ ^1S_0, F_i$ level. Finally, the x-ray fluorescence photons γ_2 as emitted in the subsequent spontaneous $1s2p\ ^3P_1, F \rightarrow 1s^2\ ^1S_0, F_f$ decay are observed.

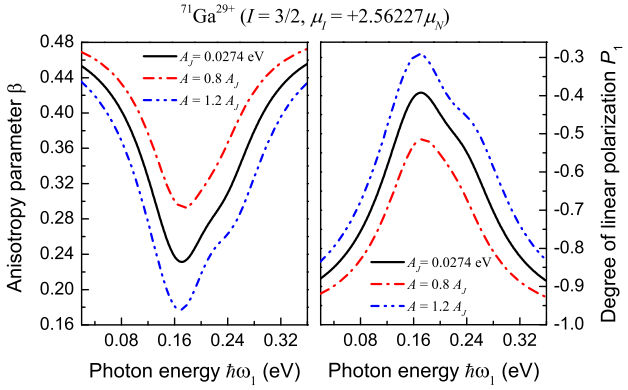

Figure 1: Anisotropy parameter β (left panel) and degree of linear polarization P_1 (right panel) of the x-ray γ_2 fluorescence photon emissions from helium-like isotopic $^{71}Ga^{29+}$ ($I = 3/2$, $\mu_I = +2.56227\,\mu_N$) ions as functions of photon energy $\hbar\omega_1$ of the incident light γ_1. Results are given for the calculated hyperfine constant $A_J = 0.0274$ eV (black solid lines) as well as for two assumed values $0.8A_J$ (red dash-dotted lines) and $1.2A_J$ (blue dash-dot-dotted lines).

Figure 1, as an example, shows the presently calculated γ_2 anisotropy parameter (angular distribution) and linear polarization for helium-like $^{71}Ga^{29+}$ ions as functions of the photon energy $\hbar\omega_1$ of the incident laser light. As can be seen clearly, these angle- and polarization-resolved properties depend strongly on the hyperfine structure values of the intermediate energy level, which is very similar to the case of (partially) overlapping fine-structure level splitting as discussed in Ref. [5]. This could be a clear "signature" for determining the associated hyperfine splitting. Therefore, we suggest that accurate x-ray measurements may indeed serve as a promising tool to determine the hyperfine splitting in highly charged helium-like ions.

References

[1] I. Klaft *et al.*, *Phys. Rev. Lett.* **73**, 2425 (1994).

[2] A. V. Volotka, D. A. Glazov, G. Plunien, and V. M. Shabaev, *Ann. Phys. (Berlin)* **525**, 636 (2013).

[3] S. Trotsenko *et al.*, *Phys. Rev. Lett.* **104**, 033001 (2010).

[4] P. H. Mokler *et al.*, *Phys. Rev. Lett.* **65**, 3108 (1990).

[5] Z. W. Wu *et al.*, *Phys. Rev. A* **93**, 063413 (2016).

Publications

S. Breitkopf, S. Wunderlich, T. Eidam, E. Shestaev, S. Holzberger, T. Gottschall, H. Carstens, A. Tünnermann, I. Pupeza, and J. Limpert
Extraction of enhanced, ultrashort laser pulses from a passive 10-MHz stack-and-dump cavity
Applied Physics B **122**, 297 (2016).

M. Yeung, S. Rykovanov, J. Bierbach, L. Li, E. Eckner, S. Kuschel, A. Woldegeorgis, C. Rödel, A. Sävert, G. G. Paulus, M. Coughlan, B. Dromey, and M. Zepf
Experimental observation of attosecond control over relativistic electron bunches with two-colour fields
Nature Photonics **239**, 1 (2016).

M. Dragowski, M. Wlodarczyk, G. Weber, J. Ciborowski, J. Enders, Y. Fritzsche, and A. Poliszczuk
Monte Carlo study of the effective Sherman function for electron polarimetry
NIM B **389**, 48 (2016).

L. Filippin, R. Beerwerth, J. Ekman, S. Fritzsche, M. Godefroid, and P. Jönsson
Multiconfiguration calculations of electronic isotope shift factors in Al I
Phyical Review A **94**, 062508 (2016).

J. Hofbrucker, A. V. Volotka, and S. Fritzsche
Relativistic calculations of the nonresonant two-photon ionization of neutral atoms
Phyical Review A **94**, 063412 (2016).

K. Minamisono, D. M. Rossi, R. Beerwerth, S. Fritzsche, D. Garand, A. Klose, Y. Liu, B. Maass, P. F. Mantica, A. J. Miller, P. Müller, W. Nazarewicz, W. Nörtershäuser, E. Olsen, M. R. Pearson, P.-G. Reinhard, E. E. Saperstein, C. Sumithrarachchi, and S. V. Tolokonnikov
Charge Radii of Neutron Deficient ^{52,53}Fe Produced by Projectile Fragmentation
Physical Review Letters **117**, 252501 (2016).

A. V. Volotka, A. Surzhykov, S. Trotsenko, G. Plunien, Th. Stöhlker, and S. Fritzsche
Nuclear Excitation by Two-Photon Electron Transition
Physical Review Letters **117**, 243001 (2016).

J. Körner, J. Hein, and M. Kaluza
Compact Aberration-Free Relay-Imaging Multi-Pass Layouts for High-Energy Laser Amplifiers
Applied Sciences **6**, 353 (2016).

H. Li, X. M. Tong, N. Schirmel, G. Urbasch, K. J. Betsch, S. Zherebtsov, F. Süssmann, A. Kessel, S. A. Trushin, G. G. Paulus, K.-M. Weitzel, and M. F. Kling
Intensity dependence of the dissociative ionization of DCl in few-cycle laser fields
Journal of Physics B: Atomic, Molecular and Optical Physics **49**, 015601 (2016).

K.-H. Blumenhagen, S. Fritzsche, T. Gassner, A. Gumberidze, R. Märtin, N. Schell, D. Seipt, U. Spillmann, A. Surzhykov, S. Trotsenko, G. Weber, V. A. Yerokhin, and Th. Stöhlker
Polarization transfer in Rayleigh scattering of hard x-rays
New Journal of Physics **18**, 103034 (2016).

R. Klas, S. Demmler, M. Tschernajew, S. Hädrich, Y. Shamir, A. Tünnermann, J. Rothhardt, and J. Limpert
Table-top milliwatt-class extreme ultraviolet high harmonic light source
Optica **3**, 1167 (2016).

M. Hornung, H. Liebetrau, S. Keppler, A. Kessler, M. Hellwing, F. Schorcht, G. A. Becker, M. Reuter, J. Polz, J. Körner, J. Hein, and M. C. Kaluza
54 J pulses with 18 nm bandwidth from a diode-pumped chirped-pulse amplification laser system
Optics Letters **41**, 5413 (2016).

G. K. Tadesse, R. Klas, S. Demmler, S. Hädrich, I. Wahyutama, M. Steinert, C. Spielmann, M. Zürch, T. Pertsch, A. Tünnermann, J. Limpert, and J. Rothhardt
High speed and high resolution table-top nanoscale imaging
Optics Letters **41**, 5170 (2016).

D. Seipt, R. A. Müller, A. Surzhykov, and S. Fritzsche
Two-color above-threshold ionization of atoms and ions in XUV Bessel beams and intense laser light
Phyical Review A **94**, 053420 (2016).

H. Heylen, C. Babcock, R. Beerwerth, J. Billowes, M. L. Bissell, K. Blaum, J. Bonnard, P. Campbell, B. Cheal, T. Day Goodacre, D. Fedorov, S. Fritzsche, R. F. Garcia Ruiz, W. Geithner, Ch. Geppert, W. Gins, L. K. Grob, M. Kowalska, K. Kreim, S. M. Lenzi, I. D. Moore, B. Maass, S. Malbrunot-Ettenauer, B. Marsh, R. Neugart, G. Neyens, W. Nörtershäuser, T. Otsuka, J. Papuga, R. Rossel, S. Rothe, R. Sánchez, Y. Tsunoda, C. Wraith, L. Xie, X. F. Yang, and D. T. Yordanov
Changes in nuclear structure along the Mn isotopic chain studied via charge radii
Physical Review C **94**, 054321 (2016).

M. Fernandes, R. Geithner, J. Golm, R. Neubert, M. Schwickert, Th. Stöhlker, J. Tan, and C. P. Welsch
Non-perturbative measurement of low-intensity charged particle beams
Superconductor Science and Technology **30**, 015001 (2016).

S. Keppler, M. Hornung, P. Zimmermann, H. Liebetrau, M. Hellwing, J. Hein, and M. C. Kaluza
Tunable filters for precise spectral gain control in ultra-short-pulse laser systems
Optics Letters **41**, 4708 (2016).

R. Müller, D. Seipt, R. Beerwerth, M. Ornigotti, A. Szameit, S. Fritzsche, and A. Surzhykov
Photoionization of neutral atoms by X waves carrying orbital angular momentum
Phyical Review A **94**, 041402 (2016).

S. Schippers, R. Beerwerth, L. Abrok, S. Bari, T. Buhr, M. Martins, S. Ricz, J. Viefhaus, S. Fritzsche, and A. Müller
Prominent role of multielectron processes in K-shell double and triple photodetachment of oxygen anions
Phyical Review A **94**, 041401 (2016).

I. P. Ivanov, D. Seipt, A. Surzhykov, and S. Fritzsche
Elastic scattering of vortex electrons provides direct access to the Coulomb phase
Physical Review D **94**, 076001 (2016).

H. Bernhardt, B. Marx-Glowna, K. Schulze, B. Grabiger, J. Haber, C. Detlefs, R. Lötzsch, T. Kämpfer, R. Röhlsberger, E. Förster, Th. Stöhlker, I. Uschmann, and G. G. Paulus
High purity x-ray polarimetry with single-crystal diamonds
Applied Physics Letters **109**, 121106 (2016).

M. Lestinsky, V. Andrianov, B. Aurand, V. Bagnoud, D. Bernhardt, H. Beyer, S. Bishop, K. Blaum, A. Bleile, At. Borovik, F. Bosch, C. Bostock, C. Brandau, A. Bräuning-Demian, I. Bray, T. Davinson, B. Ebinger, A. Echler, P. Egelhof, A. Ehresmann, M. Engström, C. Enss, N. Ferreira, D. Fischer, A. Fleischmann, E. Förster, S. Fritzsche, R. Geithner, S. Geyer, J. Glorius, K. Göbel, O. Gorda, J. Goullon, P. Grabitz, R. Grisenti, A. Gumberidze, S. Hagmann, M. Heil, A. Heinz, F. Herfurth, R. Hess, P.-M. Hillenbrand, R. Hubele, P. Indelicato, A. Källberg, O. Kester, O. Kiselev, A. Knie, C. Kozhuharov, S. Kraft-Bermuth, T. Kühl, G. Lane, Y. Litvinov, D. Liesen, X. Ma, R. Märtin, R. Moshammer, A. Müller, S. Namba, P. Neumayer, T. Nilsson, W. Nörtershäuser, G. G. Paulus, N. Petridis, M. Reed, R. Reifarth, P. Reiss, J. Rothhardt, R. Sanchez, M. Sanjari, S. Schippers, H. Schmidt, D. Schneider, P. Scholz, R. Schuch, M. Schulz, V. Shabaev, A. Simonsson, J. Sjöholm, Ö. Skeppstedt, K. Sonnabend, U. Spillmann, K. Stiebing, M. Steck, T. Stöhlker, A. Surzhykov, S. Torilov, E. Träbert, M. Trassinelli, S. Trotsenko, X. Tu, I. Uschmann, P. Walker, G. Weber, D. Winters, P. Woods, H. Zhao, and Y. Zhang
Physics book: CRYRING@ESR
European Physical Journal Special Topics **225**, 797 (2016).

I. P. Ivanov, D. Seipt, A. Surzhykov, and S. Fritzsche
Double-slit experiment in momentum space
Europhysics Letters **115**, 41001 (2016).

T. Tanikawa, A. Hage, M. Kuhlmann, J. Gonschior, S. Grunewald, E. Plönjes, S. Düsterer, G. Brenner, S. Dziarzhytski, M. Braune, M. Brachmanski, Z. Yin, F. Siewert, T. Dzelzainis, B. Dromey, M. Prandolini, F. Tavella, M. Zepf, and B. Faatz
First observation of SASE radiation using the compact wide-spectral-range XUV spectrometer at FLASH2
Nuclear Instruments and Methods in Physics Research Section A: Accelerators, Spectrometers, Detectors and Associated Equipment **830**, 170 (2016).

I. S. Wahyutama, G. K. Tadesse, A. Tünnermann, J. Limpert, and J. Rothhardt
Influence of detector noise in holographic imaging with limited photon flux
Optics Express **24**, 22013 (2016).

S. Hädrich, M. Kienel, M. Müller, A. Klenke, J. Rothhardt, R. Klas, T. Gottschall, T. Eidam, A. Drozdy, P. Jójárt, Z. Várallyay, E. Cormier, K. Osvay, A. Tünnermann, and J. Limpert
Energetic sub-2-cycle laser with 216 W average power
Optics Letters **41**, 4332 (2016).

C. Gaida, M. Gebhardt, F. Stutzki, C. Jauregui, J. Limpert, and A. Tünnermann
Thulium-doped fiber chirped-pulse amplification system with 2 GW of peak power
Optics Letters **41**, 4130 (2016).

V. A. Yerokhin, S. Y. Buhmann, S. Fritzsche, and A. Surzhykov
Electric dipole polarizabilities of Rydberg states of alkali-metal atoms
Phyical Review A **94**, 032503 (2016).

A. Surzhykov, D. Seipt, and S. Fritzsche
Probing the energy flow in Bessel light beams using atomic photoionization
Phyical Review A **94**, 033420 (2016).

S. G. Rykovanov, C. G. R. Geddes, C. B. Schroeder, E. Esarey, and W. P. Leemans
Reply to "Comment on 'Controlling the spectral shape of nonlinear Thomson scattering with proper laser chirping"'
Physical Review Accelerators and Beams **19**, 098002 (2016).

S. G. Rykovanov, J. W. Wang, V. Yu. Kharin, B. Lei, C. B. Schroeder, C. G. R. Geddes, E. Esarey, and W. P. Leemans
Tunable polarization plasma channel undulator for narrow bandwidth photon emission
Physical Review Accelerators and Beams **19**, 090703 (2016).

S. Höfer, T. Kämpfer, E. Förster, T. Stöhlker, and I. Uschmann
The formation of rarefaction waves in semiconductors after ultrashort excitation probed by grazing incidence ultrafast time-resolved x-ray diffraction
Structural Dynamics **3**, 051101 (2016).

J. Borchardt, H. Gies, and R. Sondenheimer
Global flow of the Higgs potential in a Yukawa model
European Physical Journal C **76**, 472 (2016).

S. Hädrich, J. Rothhardt, M. Krebs, S. Demmler, A. Klenke, A. Tünnermann, and J. Limpert
Single-pass high harmonic generation at high repetition rate and photon flux
Journal of Physics B: Atomic, Molecular and Optical Physics **49**, 172002 (2016).

X. Chen, M. Sanjari, P. Hülsmann, Y. Litvinov, F. Nolden, J. Piotrowski, M. Steck, Th. Stöhlker, and P. Walker
Intensity-sensitive and position-resolving cavity for heavy-ion storage rings
Nuclear Instruments and Methods in Physics Research Section A: Accelerators, Spectrometers, Detectors and Associated Equipment **826**, 39 (2016).

M. Najafi, I. Dillmann, F. Bosch, T. Faestermann, B. Gao, R. Gernhäuser, C. Kozhuharov, S. Litvinov, Y. Litvinov, L. Maier, F. Nolden, U. Popp, M. Sanjari, U. Spillmann, M. Steck, Th. Stöhlker, and H. Weick
CsI–Silicon Particle detector for Heavy ions Orbiting in Storage rings (CsISiPHOS)
Nuclear Instruments and Methods in Physics Research Section A: Accelerators, Spectrometers, Detectors and Associated Equipment **836**, 1 (2016).

J. Krey, A. Herrmann, J. Hein, J. Körner, M. C. Kaluza, and C. Rüssel
Effect of B2O3 and fluoride additions on the Yb3+ luminescence of an alumosilicate glass in the system Li2O/MgO/Al2O3/SiO2
Optical Materials Express **6**, 2662 (2016).

J. Rothhardt, S. Hädrich, Y. Shamir, M. Tschernajew, R. Klas, A. Hoffmann, G. K. Tadesse, A. Klenke, T. Gottschall, T. Eidam, J. Limpert, A. Tünnermann, R. Boll, C. Bomme, H. Dachraoui, B. Erk, M. D. Fraia, D. A. Horke, T. Kierspel, T. Mullins, A. Przystawik, E. Savelyev, J. Wiese, T. Laarmann, J. Küpper, and D. Rolles
High-repetition-rate and high-photon-flux 70 eV high-harmonic source for coincidence ion imaging of gas-phase molecules
Optics Express **24**, 18133 (2016).

M. Müller, M. Kienel, A. Klenke, T. Gottschall, E. Shestaev, M. Plötner, J. Limpert, and A. Tünnermann
1 kW 1 mJ eight-channel ultrafast fiber laser
Optics Letters **41**, 3439 (2016).

B. Landgraf, B. Aurand, G. Lehmann, T. Gangolf, M. Schnell, T. Kühl, and C. Spielmann
Broadband stimulated Raman backscattering
New Journal of Physics **18**, 073048 (2016).

M. Kienel, M. Müller, A. Klenke, J. Limpert, and A. Tünnermann
12 mJ kW-class ultrafast fiber laser system using multidimensional coherent pulse addition
Optics Letters **41**, 3343 (2016).

T. Scholtes, S. Pustelny, S. Fritzsche, V. Schultze, R. Stolz, and H.-G. Meyer
Suppression of spin-exchange relaxation in tilted magnetic fields within the geophysical range
Phyical Review A **94**, 013403 (2016).

S. Kuschel, D. Hollatz, T. Heinemann, O. Karger, M. B. Schwab, D. Ullmann, A. Knetsch, A. Seidel, C. Rödel, M. Yeung, M. Leier, A. Blinne, H. Ding, T. Kurz, D. J. Corvan, A. Sävert, S. Karsch, M. C. Kaluza, B. Hidding, and M. Zepf
Demonstration of passive plasma lensing of a laser wakefield accelerated electron bunch
Physical Review Accelerators and Beams **19**, 071301 (2016).

B. Bergmann, T. Michel, A. Surzhykov, and S. Fritzsche
Angular correlation function of the hypersatellite-satellite x-ray cascade following K-shell electron capture of ^{55}Fe
Physical Review C **94**, 014611 (2016).

F. Karbstein, and C. Sundqvist
Probing vacuum birefringence using x-ray free electron and optical high-intensity lasers
Physical Review D **94**, 013004 (2016).

A. S. Novo, M. C. Kaluza, R. A. Fonseca, and L. O. Silva
Optimizing laser-driven proton acceleration from overdense targets
Scientific Reports **6**, 29402 (2016).

A. N. Grum-Grzhimailo, E. V. Gryzlova, S. Fritzsche, and N. M. Kabachnik
Photoelectron angular distributions and correlations in sequential double and triple atomic ionization by free electron lasers
Journal of Modern Optics **63**, 334 (2016).

B. Faatz, E. Plönjes, S. Ackermann, A. Agababyan, V. Asgekar, V. Ayvazyan, S. Baark, N. Baboi, V. Balandin, N. v. Bargen, Y. Bican, O. Bilani, J. Bödewadt, M. Böhnert, R. Böspflug, S. Bonfigt, H. Bolz, F. Borges, O. Borkenhagen, M. Brachmanski, M. Braune, A. Brinkmann, O. Brovko, T. Bruns, P. Castro, J. Chen, M. K. Czwalinna, H. Damker, W. Decking, M. Degenhardt, A. Delfs, T. Delfs, H. Deng, M. Dressel, H.-T. Duhme, S. Düsterer, H. Eckoldt, A. Eislage, M. Felber, J. Feldhaus, P. Gessler, M. Gibau, N. Golubeva, T. Golz, J. Gonschior, A. Grebentsov, M. Grecki, C. Grün, S. Grunewald, K. Hacker, L. Hänisch, A. Hage, T. Hans, E. Hass, A. Hauberg, O. Hensler, M. Hesse, K. Heuck, A. Hidvegi, M. Holz, K. Honkavaara, H. Höppner, A. Ignatenko, J. Jäger, U. Jastrow, R. Kammering, S. Karstensen, A. Kaukher, H. Kay, B. Keil, K. Klose, V. Kocharyan, M. Köpke, M. Körfer, W. Kook, B. Krause, O. Krebs, S. Kreis, F. Krivan, J. Kuhlmann, M. Kuhlmann, G. Kube, T. Laarmann, C. Lechner, S. Lederer, A. Leuschner, D. Liebertz, J. Liebing, A. Liedtke, L. Lilje, T. Limberg, D. Lipka, B. Liu, B. Lorbeer, K. Ludwig, H. Mahn, G. Marinkovic, C. Martens, F. Marutzky, M. Maslocv, D. Meissner, N. Mildner, V. Miltchev, S. Molnar, D. Mross, F. Müller, R. Neumann, P. Neumann, D. Nölle, F. Obier, M. Pelzer, H.-B. Peters, K. Petersen, A. Petrosyan, G. Petrosyan, L. Petrosyan, V. Petrosyan, A. Petrov, S. Pfeiffer, A. Piotrowski, Z. Pisarov, T. Plath, P. Pototzki, M. J. Prandolini, J. Prenting, G. Priebe, B. Racky, T. Ramm, K. Rehlich, R. Riedel, M. Roggli, M. Röhling, J. Rönsch-Schulenburg, J. Rossbach, V. Rybnikov, J. Schäfer, J. Schaffran, H. Schlarb, G. Schlesselmann, M. Schlösser, P. Schmid, C. Schmidt, F. Schmidt-Föhre, M. Schmitz, E. Schneidmiller, A. Schöps, M. Scholz, S. Schreiber, K. Schütt, U. Schütz, H. Schulte-Schrepping, M. Schulz, A. Shabunov, P. Smirnov, E. Sombrowski, A. Sorokin, B. Sparr, J. Spengler, M. Staack, M. Stadler, C. Stechmann, B. Steffen, N. Stojanovic, V. Sychev, E. Syresin, T. Tanikawa, F. Tavella, N. Tesch, K. Tiedtke, M. Tischer, R. Treusch, S. Tripathi, P. Vagin, P. Vetrov, S. Vilcins, M. Vogt, A. d. Z. Wagner, T. Wamsat, H. Weddig, G. Weichert, H. Weigelt, N. Wentowski, C. Wiebers, T. Wilksen, A. Willner, K. Wittenburg, T. Wohlenberg, J. Wortmann, W. Wurth, M. Yurkov, I. Zagorodnov, and J. Zemella
Simultaneous operation of two soft x-ray free-electron lasers driven by one linear accelerator
New Journal of Physics **18**, 062002 (2016).

J. Körner, F. Yue, J. Hein, and M. C. Kaluza
Spatially and temporally resolved temperature measurement in laser media
Optics Letters **41**, 2525 (2016).

M. Schöffler, X. Xie, P. Wustelt, M. Möller, S. Roither, D. Kartashov, A. Sayler, A. Baltuska, G. G. Paulus, and M. Kitzler
Laser-subcycle control of sequential double-ionization dynamics of helium
Phyical Review A **93**, 063421 (2016).

Z. W. Wu, A. V. Volotka, A. Surzhykov, C. Z. Dong, and S. Fritzsche
Level sequence and splitting identification of closely spaced energy levels by angle-resolved analysis of fluorescence light
Phyical Review A **93**, 063413 (2016).

V. Yu. Kharin, D. Seipt, and S. G. Rykovanov
Temporal laser-pulse-shape effects in nonlinear Thomson scattering
Phyical Review A **93**, 063801 (2016).

M. L. Bissell, T. Carette, K. T. Flanagan, P. Vingerhoets, J. Billowes, K. Blaum, B. Cheal, S. Fritzsche, M. Godefroid, M. Kowalska, J. Krämer, R. Neugart, G. Neyens, W. Nörtershäuser, and D. T. Yordanov
Cu charge radii reveal a weak sub-shell effect at N=40
Physical Review C **93**, 064318 (2016).

C. Shah, P. Amaro, R. Steinbrügge, C. Beilmann, S. Bernitt, S. Fritzsche, A. Surzhykov, J. Crespo López-Urrutia, and S. Tashenov
Strong higher-order resonant contributions to x-ray line polarization in hot plasmas
Physical Review E **93**, 061201 (2016).

J. Haber, K. Schulze, K. Schlage, R. Loetzsch, L. Bocklage, T. Gurieva, H. Bernhardt, H.-C. Wille, R. Rüffer, I. Uschmann, G. G. Paulus, and R. Röhlsberger
Collective strong coupling of X-rays and nuclei in a nuclear optical lattice
Nature Photonics **10**, 445 (2016).

M. Kübel, C. Burger, N. Kling, T. Pischke, L. Beaufore, I. Ben-Itzhak, G. G. Paulus, J. Ullrich, T. Pfeifer, R. Moshammer, M. F. Kling, and B. Bergues
Complete characterization of single-cycle double ionization of argon from the nonsequential to the sequential ionization regime
Phyical Review A **93**, 053422 (2016).

N. A. Zubova, A. V. Malyshev, I. I. Tupitsyn, V. M. Shabaev, Y. S. Kozhedub, G. Plunien, C. Brandau, and Th. Stöhlker
Isotope shifts of the $2p^{3/2}$-$2p^{1/2}$ transition in B-like ions
Phyical Review A **93**, 052502 (2016).

R. H. Pratt, R. A. Müller, and A. Surzhykov
Sum rules for the polarization correlations in photoionization and bremsstrahlung
Phyical Review A **93**, 053421 (2016).

A. A. Peshkov, V. G. Serbo, S. Fritzsche, and A. Surzhykov
Absorption of twisted light by a mesoscopic atomic target
Physica Scripta **91**, 064001 (2016).

F. Wagner, O. Deppert, C. Brabetz, P. Fiala, A. Kleinschmidt, P. Poth, V. A. Schanz, A. Tebartz, B. Zielbauer, M. Roth, T. Stöhlker, and V. Bagnoud
Maximum Proton Energy above 85 MeV from the Relativistic Interaction of Laser Pulses with Micrometer Thick CH_2 Targets
Physical Review Letters **116**, 205002 (2016).

C. Kohlfürst, and R. Alkofer
On the effect of time-dependent inhomogeneous magnetic fields in electron–positron pair production
Physics Letters B **756**, 371 (2016).

E. Siminos, S. Skupin, A. Sävert, J. M. Cole, S. P. D. Mangles, and M. C. Kaluza
Modeling ultrafast shadowgraphy in laser-plasma interaction experiments
Plasma Physics and Controlled Fusion **58**, 065004 (2016).

P. Hansinger, G. Maleshkov, I. L. Garanovich, D. V. Skryabin, D. N. Neshev, A. Dreischuh, and G. G. Paulus
White light generated by femtosecond optical vortex beams
Journal of the Optical Society of America B **33**, 681 (2016).

H. Carstens, M. Högner, T. Saule, S. Holzberger, N. Lilienfein, A. Guggenmos, C. Jocher, T. Eidam, D. Esser, V. Tosa, V. Pervak, J. Limpert, A. Tünnermann, U. Kleineberg, F. Krausz, and I. Pupeza
High-harmonic generation at 250 Mhz with photon energies exeeding 100 eV
Optica **3**, 366 (2016).

C. Serrat, D. Roca, J. M. Budesca, J. Seres, E. Seres, B. Aurand, A. Hoffmann, S. Namba, T. Kuehl, and C. Spielmann
Avalanche of stimulated forward scattering in high harmonic generation
Optics Express **24**, 8028 (2016).

C. Jauregui, H.-J. Otto, S. Breitkopf, J. Limpert, and A. Tünnermann Optimizing high-power Yb-doped fiber amplifier systems in the presence of transverse mode instabilities Optics Express 24 7879 2016

M. Mueller, M. Kienel, A. Klenke, T. Eidam, J. Limpert, and A. Tünnermann
Phase stabilization of spatiotemporally multiplexed ultrafast amplifiers
Optics Express **24**, 7893 (2016).

J. Rothardt, C. Rothardt, M. Müller, A. Klenke, M. Kienle, S. Demmler, T. Elsmann, M. Rothardt, J. Limpert, and A. Tünnermann
100 W average power femtosecond laser at 343 nm
Optics Letters **41**, 1885 (2016).

P.-M. Hillenbrand, S. Hagmann, J. M. Monti, R. D. Rivarola, K.-H. Blumenhagen, C. Brandau, W. Chen, R. D. DuBois, A. Gumberidze, D. L. Guo, M. Lestinsky, Yu. A. Litvinov, A. Müller, S. Schippers, U. Spillmann, S. Trotsenko, G. Weber, and Th. Stöhlker
Strong asymmetry of the electron-loss-to-continuum cusp of multielectron U^{28+} projectiles in near-relativistic collisions with gaseous targets
Phyical Review A **93**, 042709 (2016).

H. Gies, F. Karbstein, and N. Seegert
Photon merging and splitting in electromagnetic field inhomogeneities
Physical Review D **93**, 085034 (2016).

C. Hahn, G. Weber, R. Märtin, S. Höfer, T. Kämpfer, and Th. Stöhlker
CdTe Timepix detectors for single-photon spectroscopy and linear polarimetry of high-flux hard x-ray radiation
Review of Scientific Instruments **87**, 043106 (2016).

S. Hädrich, J. Rothhardt, S. Demmler, M. Tschernajew, A. Hoffmann, M. Krebs, A. Liem, O. d. Vries, M. Plötner, S. Fabian, T. Schreiber, J. Limpert, and A. Tünnermann
Scalability of components for kW-level average power few-cycle lasers
Applied Optics **55**, 1636 (2016).

W. Cayzac, A. Frank, A. Ortner, V. Bagnoud, M. Basko, S. Bedacht, A. Blažević, O. Deppert, D. Gericke, L. Hallo, A. Knetsch, D. Kraus, G. Malka, K. Pépitone, G. Schaumann, T. Schlegel, D. Schumacher, An. Tauschwitz, J. Vorberger, F. Wagner, and M. Roth
Simulations of the energy loss of ions at the stopping-power maximum in a laser-induced plasma
Journal of Physics: Conference Series **688**, 012009 (2016).

D. Seipt, V. Kharin, S. Rykovanov, A. Surzhykov, and S. Fritzsche
Analytical results for nonlinear Compton scattering in short intense laser pulses
Journal of Plasma Physics **82**, 655820203 (2016).

S. Keppler, A. Sävert, J. Körner, M. Hornung, H. Liebetrau, J. Hein, and M. Kaluza
The generation of amplified spontaneous emission in high-power CPA laser systems
Laser & Photonics Reviews **10**, 264 (2016).

A. Gopal, A. H. Woldegeorgis, S. Herzer, G. G. Paulus, P. Singh, W. Ziegler, and T. May
Smith–Purcell radiation in the terahertz regime using charged particle beams from laser–matter interactions
Laser and Particle Beams **34**, 187 (2016).

A. V. Bogatskaya, E. A. Volkova, V. Y. Kharin, and A. M. Popov
Polarization response in extreme nonlinear optics: when can the semiclassical approach be used?
Laser Physics Letters **13**, 045301 (2016).

T. Kämpfer, I. Uschmann, Z. W. Wu, A. Surzhykov, S. Fritzsche, E. Förster, and G. G. Paulus
Linear polarization of the characteristic x-ray lines following inner-shell photoionization of tungsten
Phyical Review A **93**, 033409 (2016).

S. G. Rykovanov, C. G. R. Geddes, C. B. Schroeder, E. Esarey, and W. P. Leemans
Controlling the spectral shape of nonlinear Thomson scattering with proper laser chirping
Physical Review Accelerators and Beams **19**, 030701 (2016).

H. Gies, and G. Torgrimsson
Critical Schwinger Pair Production
Physical Review Letters **116**, 090406 (2016).

M. Schäfer, I. Huet, and H. Gies
Worldline numerics for energy-momentum tensors in Casimir geometries
Journal of Physics A: Mathematical and Theoretical **49**, 135402 (2016).

B. Dromey, M. Coughlan, L. Senje, M. Taylor, S. Kuschel, B. Villagomez-Bernabe, R. Stefanuik, G. Nersisyan, L. Stella, J. Kohanoff, M. Borghesi, F. Currell, D. Riley, D. Jung, C.-G. Wahlström, C. L. S. Lewis, and M. Zepf
Picosecond metrology of laser-driven proton bursts
Nature Communications **7**, 10642 (2016).

D. Seipt, A. Surzhykov, S. Fritzsche, and B. Kämpfer
Caustic structures in x-ray Compton scattering off electrons driven by a short intense laser pulse
New Journal of Physics **18**, 023044 (2016).

A. V. Volotka, V. A. Yerokhin, A. Surzhykov, Th. Stöhlker, and S. Fritzsche
Many-electron effects on x-ray Rayleigh scattering by highly charged He-like ions
Phyical Review A **93**, 023418 (2016).

J. W. Wang, W. Yu, M. Y. Yu, H. Xu, J. J. Ju, S. X. Luan, M. Murakami, M. Zepf, and S. Rykovanov
High-energy-density electron beam from interaction of two successive laser pulses with subcritical-density plasma
Physical Review Accelerators and Beams **19**, 021301 (2016).

A. Titov, B. Kämpfer, A. Hosaka, T. Nousch, and D. Seipt
Determination of the carrier envelope phase for short, circularly polarized laser pulses
Physical Review D **93**, 045010 (2016).

S. Fuchs, C. Rödel, A. Blinne, U. Zastrau, M. Wünsche, V. Hilbert, L. Glaser, J. Viefhaus, E. Frumker, P. Corkum, E. Förster, and G. G. Paulus
Nanometer resolution optical coherence tomography using broad bandwidth XUV and soft x-ray radiation
Scientific Reports **6**, 20658 (2016).

S. G. Podorov, and E. Förster
Direct inversion of digital 3D Fraunhofer holography maps
Applied Optics **55**, A150 (2016).

A. Blinne, and E. Strobel
Comparison of semiclassical and Wigner function methods in pair production in rotating fields
Physical Review D **93**, 025014 (2016).

J. Braun, F. Karbstein, S. Rechenberger, and D. Roscher
Crystalline ground states in Polyakov-loop extended Nambu-Jona-Lasinio models
Physical Review D **93**, 014032 (2016).